

ADHESION IMPROVEMENT OF CHEMICALLY VAPOR DEPOSITED DIAMOND
THIN FILMS ON CEMENTED CARBIDES VIA LASER SURFACE
MODIFICATION

By

DONG-GU LEE

A DISSERTATION PRESENTED TO THE GRADUATE SCHOOL
OF THE UNIVERSITY OF FLORIDA IN PARTIAL FULFILLMENT
OF THE REQUIREMENTS FOR THE DEGREE OF
DOCTOR OF PHILOSOPHY

UNIVERSITY OF FLORIDA

1998

ACKNOWLEDGMENTS

I would like to acknowledge many people that have made this work possible. I would like to express my heartfelt appreciation to my advisor, Dr. Rajiv K. Singh, for his guidance, support, and encouragement. A lot of suggestions that he has given have opened my mind more widely for various approaches of researches. Thanks are also due to my doctoral committee members, Dr. Paul Holloway, Dr. Stephen Pearton, Dr. Cammy Abernathy, Dr. David Tanner, and Dr. Fred Sharifi, for their interest and assistance in this work.

I would also like to thank Ming Huang and Dr. Tim Anderson in Chemical Engineering, and Dr. Vitor Baranauskas and Dr. Vladimir Jesus Trava Airoldi at the Universidade Estadual de Campinas, Brasil, for their help with Raman spectroscopy. Thanks are due to Wayne Acree for help with electron microprobe and Eric Lambers for help with Auger electron spectroscopy.

I would like to acknowledge Engineering Research Center for Particle Science and Technology for its support.

Special thanks go to Don Gilbert for thoughtful discussion and extensive support. I would like to acknowledge

all the friends and coworkers who made graduate school memorable time. Guangjin, Jongryul, Minhyeon, Jooho, Jongjin, Keunyong, Fan, John, Jim, Dr. Kumar, Ali, Uday, Kyugong, Seungmahn, and others provided constant support and a wonderful life in Gainesville.

Finally, I must express my deepest appreciation to my wife, Kyunghwa, and my son, Taeyoung, for unending love, support, and encouragement. I would also like to thank my parents and my brothers' families. Without their love and support, it would be impossible to go to the successes in my life.

TABLE OF CONTENTS

ACKNOWLEDGMENTS	ii
ABSTRACT	vi
CHAPTER 1 INTRODUCTION	1
Motivation and Objectives	1
Dissertation Outline	4
CHAPTER 2 LITERATURE REVIEW	6
Diamond Chemical Vapor Deposition	6
Diamond Coated Tools	11
Interface in Diamond-Cemented Carbide System	15
CHAPTER 3 EXPERIMENTAL APPROACH	22
Substrate Materials and Preparation	22
Laser Setup for Surface Modification	24
Etching Treatment	26
Diamond Seeding Treatment	27
Hot Filament Assisted Chemical Vapor Deposition	28
Characterization	30
Scanning Electron Microscopy (SEM)	31
Surface Profilometry	31
X-Ray Diffraction (XRD)	32
Electron Probe Microanalysis (EPMA)	33
Auger Electron Spectroscopy (AES)	33
Transmission Electron Microscopy (TEM)	34
Raman Spectroscopy	35
Indentation Adhesion Test	38
CHAPTER 4 RESULTS AND DISCUSSION	46
Growth of Diamond Thin Films	46
Gas Flow Rate and Chamber Pressure	46
Methane Concentration	51
Filament Temperature	53

Substrate Temperature	56
Summary	60
Laser-Cemented Carbide Interaction	61
Evolution of Surface Feature by Laser	62
Composition and Phase Change by Laser	72
Stress Analysis of Diamond Films	77
Etching and Heat Treatment	86
CHAPTER 5 CONCLUSIONS	179
APPENDIX PROPERTIES AND APPLICATIONS OF CVD DIAMOND . . .	182
LIST OF REFERENCES	184
BIOGRAPHICAL SKETCH	193

CHAPTER 1 INTRODUCTION

Motivation and Objectives

Diamond synthesis from the vapor phase by chemical vapor deposition has attracted much interest scientifically and technologically over the past decade because diamond has an unusual combination of extreme properties as shown in appendix. Due to these outstanding properties, diamond has emerged as an excellent candidate for cutting tool applications. It has a rare combination of the highest hardness (Knoop, 10,000 kg/mm²), which is twice that of cubic BN as well as about four times that of TiC, high compressive strength (> 110 GPa), and a good thermal shock resistance ($\Delta T > 1000$ K), together with a low coefficient of friction (0.03), which is the same as Teflon [Yod93]. In addition, diamond also exhibits the highest thermal conductivity (20 W/cm/K), which is about five times greater than that of copper, leading to efficient heat dissipation during cutting operations. Since the development of low pressure synthesis of diamond from a vapor of hydrocarbons diluted in an excess of hydrogen,

diamond coated cutting tools have been predicted to become one of the first large-scale commercial applications for CVD diamond [Bac89]. CVD diamond coating technology can be applied to the already available tool inserts such as cemented carbides and silicon nitride. Until recently the only diamond tools on the market were polycrystalline diamond (PCD) tools. The cutting edge of PCD tools is a sintered polycrystalline diamond tip bonded with cobalt made under high pressure-high temperature conditions and brazed onto the carbide insert. Because of the high cost involved in manufacturing, the PCD tools are very expensive. In addition, the tools are usually single tipped and limited to a relatively simple planar geometry.

CVD diamond cutting tools are divided into two categories: diamond sheet (thick film) tools and thin film coated inserts. The diamond sheet tools are fabricated from large, free-standing CVD diamond discs (~500 μm thick) and laser-cut into small blanks. Then these blanks are vacuum-brazed into a pocket which is ground into the corner of a cemented carbide tool. The development of successful brazing methods could avoid the adhesion problems associated with early thin film coated tools. The sheet tools were thus designed to compete with conventional single-point PCD tools [Hay93].

Thin film ($< 50 \mu\text{m}$) tools offer several advantages over single-point tools in that the entire functional surface of the tool is coated with diamond, offering multiple edges per tool insert and advanced chip breaker geometry [Cer93]. Compared to an uncoated cemented carbide tool, the CVD diamond coated tool shows much greater abrasive wear resistance which results in up to ten times longer tool life [Kik91], and less built-up edge and lower cutting forces which yield a better surface finish on the workpiece materials [Kar96].

However, one of the largest barriers to be overcome is the poor adhesion of diamond film to cemented carbides substrate (WC-Co). This is due to (i) the large thermal mismatch of the diamond film with the cemented carbide substrate tool and (ii) weak interface bonding resulting from graphite film formation during low pressure diamond deposition. There are many reports which claim to reduce the thermal mismatch and to limit the graphite formation by etching cobalt and/or depositing interlayers as diffusion barriers [Kik87, Nes93].

In this study, a unique method has been developed to improve the adhesion of diamond films to carbide tools [Sin96, Lee98]. By controlling the roughness of the interface between the diamond film and the cemented carbide substrate using a pulsed laser, it is expected that mechanical interlocking of diamond films to cemented carbides, release of interfacial

stress, increase of surface bonding, and complicated crack propagation paths can be achieved, thereby improving adhesion.

The first objective of this study is to investigate process parameters of diamond films in a hot filament assisted chemical vapor deposition (HFCVD) system. The second objective is to understand the mechanism of laser-cemented carbide interaction which is used for the formation of micro-rough substrate for diamond coatings. The third objective is to study stress distribution inside diamond films as a function of substrate roughness and correlate it with adhesion properties.

Dissertation Outline

Chapter 2 presents a general review on the subject of the diamond chemical vapor deposition process. This includes a brief of history of development of low pressure diamond synthesis, various processing methods, and the role of atomic hydrogen gas. Diamond coated tools are also discussed, including applications of diamond tools and previous works to improve adhesion of diamond films.

Chapter 3 discusses the experimental procedures and characterization methods that were used for investigating process parameters of diamond thin films in the HFCVD system and for understanding laser-solid interactions.

Chapter 4 presents and discusses the results of the experiments, followed by the conclusions of the study in chapter 5.

CHAPTER 2 LITERATURE REVIEW

Diamond Chemical Vapor Deposition

Diamond vapor deposition can be traced back to Eversole [Eve62], Angus et al. [Ang68], and Deryagin et al. [Der68] in the late 1950s through the mid 1970s. However, most of the scientific community viewed their results with great skepticism because of a low growth rate ($\text{\AA}/\text{hr}$) and codepositions of graphitic carbon. The major breakthrough was made by Deryagin's group in the late 1970s which indicated that gas activation techniques can greatly increase the growth rate ($\mu\text{m}/\text{hr}$) of diamond while suppressing the graphite deposition [Der89]. Starting in the early 1980s, Japanese researchers began to report dramatic successes in low pressure diamond growth using a variety of new gas activation techniques [Mat82, Kam83, Mat85].

Graphite is the most stable form of carbon under normal conditions, but at pressures of approximately 60,000 atmospheres and at temperatures exceeding 1500°C, diamond is the thermodynamically stable phase as shown in Fig. 2.1. The

possibility of diamond formation under normal CVD conditions can be attributed to a combination of kinetic, thermodynamic, and chemical factors: i) a significant activation energy barrier impeding spontaneous transformation of diamond to graphite [Gei92], ii) graphite being more stable than diamond only by a small free energy difference (0.5 kcal/mole at 298 K) [Wag82], and iii) the critical role of atomic hydrogen during growth in stabilizing diamond with respect to graphite [Spe89b]. Atomic hydrogen is believed to play a number of roles in the CVD process: i) it undergoes H abstraction with stable hydrocarbon molecules, producing highly reactive carbon-containing radical species [Spe89a], ii) it terminates the dangling carbon bonds on the growing diamond surface and prevents them from cross linking and reconstructing to a graphite surface [Pat86, Spe89b], and iii) it etches graphite several orders of magnitude faster than diamond, allowing diamond to grow without many impurities [May95, Set87, Sai88].

The common diamond deposition systems used currently are hot filament assisted chemical vapor deposition (CVD), plasma assisted CVD (DC, RF, microwave), plasma jet CVD, and combustion flame (oxyacetylene) CVD (Fig. 2.2). Hot filament assisted CVD involves the activation of feed gases using a hot filament [Mat82, Mou89]. Typical deposition gases are composed of methane and hydrogen with a ratio of 0.5-2:98-99.5. The filament temperature and substrate temperature are

controlled in the range of 1900 to 2200°C and 700 to 1000°C, respectively. Chamber pressures are controlled at ~10-50 torr with a flow rate of ~100-200 sccm. Plasma assisted CVD activates feed gases utilizing microwaves [Kam83, Sai86, Kob88, Eto92], inductively coupled rf [Mat85, Aka89, Rud92], and DC [Suz87, Sin88]. Among them, microwave excitation has been used much more extensively than any other method. The plasma systems yield a diamond growth rate of 1 to 20 $\mu\text{m}/\text{hr}$ and can operate in lower pressure than hot filament assisted CVD. Plasma jet CVD employs extremely high gas temperatures of >5000 K. The plasma is generally generated by a dc discharge at the nozzle [Kur88]. Chamber pressure is controlled in the range of 100-400 Torr. Combustion flame CVD simply involves a standard oxygen-acetylene brazing torch and a cooled substrate (600-1000°C) configuration [Hir89, Yar89, Sna91]. This method obtained a lot of attentions partly because of the simplicity and low cost of the experimental apparatus and partly because of the high growth rates obtained. Growth rates of greater than 100 $\mu\text{m}/\text{hr}$ have been reported.

While each method differs in detail, they all share some features in common. For example, growth of diamond normally requires that the substrate be maintained at a temperature in the range 500-1000°C, and that the hydrocarbon precursor gases be diluted in an excess of hydrogen (typically 1-3% CH_4).

Growth rates for the various deposition processes vary from submicron to hundreds of microns per hour. Bachmann et al. [Bac92] correlated the gas temperature in various CVD methods with the linear growth rate of diamond films as shown in Fig. 2.3. The lowest growth rates ($0.01 \mu\text{m/hr}$) are obtained with the simple thermal CVD method in which only the substrate is heated to about 1000°C . The low-pressure DC and RF discharges induce some additional plasma-heating of the gas, besides the heating from the substrate held at 1000°C . Their growth rates are typically $0.1 \mu\text{m/hr}$. The low-pressure microwave plasma and the hot filament CVD method have a gas temperature of between 2000 and 2500°C and their growth rate varies from 1 to $10 \mu\text{m/hr}$. The gas temperature in the oxyacetylene method is typically 3000 - 3500°C and the corresponding growth rates are typically $100 \mu\text{m/hr}$. Finally, the high-pressure plasmas whose gas temperature is between 5000 and 7000°C have growth rates in the range of 100 - $1000 \mu\text{m/hr}$. This correlation between gas temperature and growth rate of diamond films is attributed to the generation of atomic hydrogen and appropriate neutral carbon-containing radicals by collisions not only with electrons, but with gas molecules as well.

The simplified mechanism of diamond growth can be explained as follows [Ang91]. The first main chemical reaction in the diamond deposition is to dissociate the molecular hydrogen into atomic hydrogen through thermal,

microwave, rf, or dc activation.



The energy supplied to the system through reaction (2.1) drives several subsequent exothermic processes (2.2, 2.3, and 2.4). Atomic hydrogen can combine with vacant surface site, S^{..}.



Atomic hydrogen can also remove hydrogen from the hydrogenated surface by an abstraction reaction.



Atomic hydrogen can also abstract hydrogen from another hydrocarbon molecule, R-H such as CH₄.



Now, radicals, R^{..} produced by (2.4) or by other decomposition processes, combine with vacant surface sites to form the new diamond.



Reaction of H₂ with free radical surface sites is also possible by the reverse reaction of (2.3). Atomic hydrogen and free radicals can be destroyed by gas reaction (2.6 and 2.7) with a third body, M, such as a chamber wall.



In general, diamond films deposited by CVD techniques adhere well to carbides and carbide formers such as silicon,

silicon carbide, titanium, and tungsten carbide. However, it is very difficult to nucleate and grow diamond in the presence of cobalt, iron, and nickel. These materials promote the formation of graphitic carbon rather than diamond.

Diamond Coated Tools

Demand for aluminum alloys has been rapidly increasing in recent years because the automotive industry is turning to lightweight, high strength, and nonferrous materials, especially aluminum alloys in selecting materials for automobiles [Cer93]. Aluminum alloys are among materials for which it is known to be the most difficult to obtain a well-finished surface after machining since build-ups on a tool easily weld to surfaces of these works. Al-Si alloys, which are mostly used for engine and transmission parts, use a large amount of silicon (14-20%) to obtain high strength and good castability. These Al-Si alloys are very abrasive because of a high dispersion of primary silicon precipitates in an aluminum matrix, requiring many tool changes when cemented carbide tools are used. Diamond tools are being increasingly used in the automotive industry because of the abrasiveness of these materials [Cer93]. In addition to the machinability of nonferrous metals such as aluminum and copper, diamond tools

can machine metal-matrix composites (MMC) reinforced with Al_2O_3 , or SiC particulates or whiskers, fiber-reinforced plastics (FRPs) with glass or carbon fibers, carbon-carbon composites, woods, stones, and ceramics. One serious limitation on the application of diamond tools is the high chemical reactivity (solubility) of carbon to ferrous materials at elevated temperatures, making diamond unsuitable for machining steels and cast irons. With these materials, a very high temperature (up to 1000°C) is generated at the tool/chip interface, resulting in extremely rapid wear of the diamond tool by a chemical dissolution mechanism [Kar96].

Diamond coatings deposited by CVD on cemented carbides (WC-Co) generally have a low adhesive strength. The reasons for the poor adhesion are i) mismatch of the thermal expansion coefficient between diamond ($0.8 \times 10^{-6} \text{ K}^{-1}$ at room temp.) and the cemented carbide (WC-6Co: $5.0 \times 10^{-6} \text{ K}^{-1}$ at room temp.), leading to large thermal stress at the interface [Kuo90, Sod90], and ii) the interaction between carbon deposited from feed gases and cobalt binder on the surface of the tools [Mur88, Lux92, Rei90]. Without strong bonding to the substrate the coating will not endure the shearing force in the machining processes and will be easily delaminated.

The surface of a tungsten carbide based cemented carbide substrate is composed of WC grains bonded together by cobalt or a cobalt alloy. The cobalt is not only between WC grains

but it also thinly covers the grains at the surface. Although the cobalt is important for maintaining toughness of cemented carbide tools, the presence of cobalt is harmful to diamond deposition on the carbide surface. Cobalt, as well as nickel and iron, has considerable solubility (several atomic percent) for carbon at diamond deposition temperature ($\sim 1000^{\circ}\text{C}$) and rapid diffusivity of carbon (four orders of magnitude higher) relative to refractory metals [Jof88]. The dissolution and diffusion of carbon into the cobalt extends the incubation period for diamond nucleation and enhances the accumulation of graphite at the diamond-carbide interface by catalytic effect [Mur88, McC89, Oak91, Che93].

In order to overcome the adhesion problem, there have been attempts to use a variety of substrate materials such as silicon nitride [Sod91, Ito91], silicon carbide [Sen92], SiAlON (39Si-54N-3.5Al-3.5O) [McC92], and binderless tungsten carbide [Sai90] instead of cemented carbide (WC-Co). However, these substrate materials are limited in their usefulness because of low fracture toughness.

Other approaches in cemented carbide systems to limit the carbon-cobalt interaction have been also reported. Surface etching of cobalt is widely used to reduce the amount of cobalt at the diamond-cemented carbide interface before diamond deposition. Various etching agents such as HNO_3 [Nes95], HCl [Kik87], FeCl_3 [Gra93], H_2SO_4 [Ike96], $\text{H}_2\text{O}_2/\text{H}_2\text{SO}_4$

[Par93], etc. have been used for the removal of cobalt at the surface of cemented carbides. There is also a report about plasma etching of cobalt using a gas mixture of CO-H₂ or H₂O-H₂ because Co(CO)₄ and Co(OH)₂ are volatile compounds [Sai91]. Other researchers attempted a decarburation process or a heat treatment process for roughening a cemented carbide surface for adhesion improvement. A Japanese team at Toshiba Tungaloy [Sai90, Shi94] proposed the decarburation of hot pressed WC or WC-Co and then recrystallization by recarburation, resulting in grain refinement and surface roughening, thereby improving adhesion. Oles et al. [Ole96] reported a heat treatment method to eliminate cobalt by evaporation and to roughen an insert surface by the growth of tungsten carbide particles only at the surface. Another way for improving adhesion is the deposition of various interlayers such as a-C, Nb, W, Ti, Mo, TiC, TiN, Si₃N₄, and SiC prior to diamond coating [Nes93, Nes95, Deu96, Che93, Iso93, End96]. The function of interlayers is i) the formation of a diffusion barrier between the cobalt and the diamond coating, and ii) the relief of residual stresses at the diamond-carbide interface caused by thermal mismatch. Functionally gradient diamond films have been obtained by Kurihara et al. [Kur92] by plasma-spraying metal powders on the substrate during the diamond synthesis and controlling the composition gradient with a powder feed rate. These

approaches still do not provide strong enough adhesion to endure the shear force at high speed, leading to a possibility of flaking.

Interface in Diamond-Cemented Carbide System

The type of interface between a film and a substrate is determined by substrate morphology, chemical interactions, diffusion rates, and nucleation processes. As shown in Fig. 2.4, the interfaces can be distinguished into approximately four types [Ohr92]: (i) an abrupt interface which leads to sharp transitions in materials properties due to the absence of interaction between film and substrate atoms, and low interdiffusion rates, (ii) compound interfaces in which one or more layers of compounds of film-substrate and/or environmental gases are created by chemical interaction, (iii) a diffusion interface in which a gradual change in composition between film and substrate is created due to the mutual solubility of film and substrate, and (iv) a mechanical interface which results from interlocking of the depositing material with a rough substrate surface. When we consider a diamond film on a cemented carbide (WC-6%Co) substrate material from the interface point of view, the diamond coated cemented carbide may have a kind of compound interface due to

the formation of a graphite interlayer. This is detrimental to the adhesion of the diamond-cemented carbide due to poor mechanical properties. As mentioned before, some researchers have intentionally formed single or multiple interlayers to improve interface characteristics. When the cobalt at the surface of a cemented carbide is removed by etching agents prior to diamond coating, the diamond-carbide interface is mainly an abrupt interface along with small contribution of a mechanical interface due to microroughness caused by the removal of cobalt around tungsten carbide particles. There is no report that any kinds of chemical interactions take place between diamond and tungsten carbide. In this type of interface, stresses and defects are confined to a narrow planar region where stress gradients are high. Film adhesion in this case will be low because of easy interfacial fracture modes.

This thesis focused on the development of a mechanical interface between a diamond film and a cemented carbide substrate. The adhesion strength of a coated material having a mechanical interface will depend primarily on the mechanical properties of the film and substrate and on the interfacial geometry. Adhesion failure can also be reduced by the distribution of residual stress along the thickness of a gradient interface formed by surface roughness as compared to a high residual stress concentration at an abrupt interface

[Wil93a]. In addition, the increased surface roughness causes an increased surface area, leading to more interfacial bonding and better adhesion [Cha74]. A tortuous fracture path induced by rough surfaces and mechanical anchoring also leads to high adhesion. The decarburization-recrystallization process [Shi94] of a cemented carbide to increase surface area and the heat treatment process to increase surface roughness by growing larger tungsten carbide particles at the surface [Ole96] which have been mentioned previously, can be put in the group for obtaining mechanical interfaces.

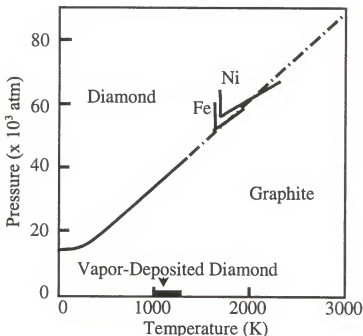


Figure 2.1 Pressure versus temperature phase diagram for carbon. (The lines labeled with metallic elements indicate the HPHT conditions utilized for diamond growth using metallic solvents. The use of a liquid metal catalyst enables one to use relatively low pressures that are close to the diamond-graphite phase boundary) [Bun61].

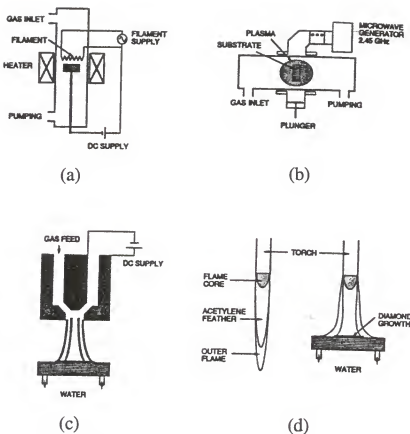


Figure 2.2 Schematics of four methods for obtaining diamond film growth: (a) filament assisted CVD, (b) plasma assisted CVD, (c) plasma jet, and (d) combustion flame assisted CVD [Mat89].

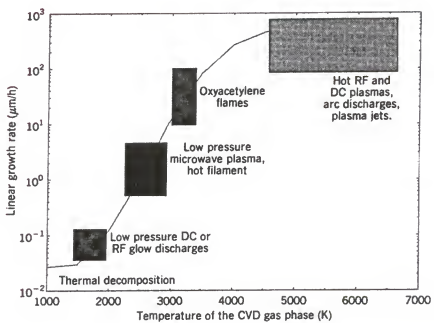


Figure 2.3 Growth rate for different diamond CVD methods versus the gas temperature in their activation zones [Bac92].

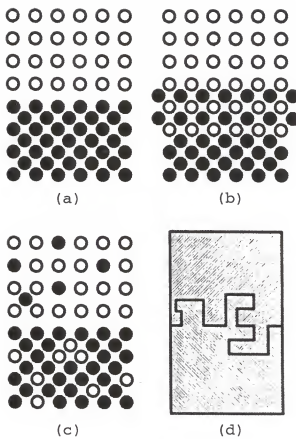


Figure 2.4 Different interfacial layers formed between film and substrate: (a) abrupt interface, (b) compound interface, (c) diffusion interface, and (d) mechanical interface [Ohr92].

CHAPTER 3 EXPERIMENTAL APPROACH

In this study, diamond films were deposited on silicon to observe the behavior of process parameters in HFCVD system. On the other hand, cemented carbides were modified using a KrF pulsed laser system, then coated with diamond films in HFCVD system. Other surface treatments such as etching and heat treatments also were attempted. Morphological, topological, compositional, residual stress, and adhesion changes of diamond films and laser modified substrates were characterized by various techniques including scanning electron microscopy (SEM), surface profilometry, X-ray diffraction (XRD), electron probe microanalysis (EPMA), Auger electron spectroscopy (AES), transmission electron microscopy (TEM), micro-Raman spectroscopy, and Rockwell indentation.

Substrate Materials and Preparation

Two kinds of substrates were used. The first substrate to be used for controlling diamond deposition parameters was (100) silicon with dimensions of 1 cm x 1cm x 400 μm thick. All samples were cleaned in acetone and then scrachted/seeded

with diamond powders using a diamond suspension in ultrasonic bath before loading into the HFCVD system. Different parameters of the HFCVD system affecting diamond growth were changed such as filament/substrate temperature, chamber pressure, gas flow rate, and gas composition.

The second substrate to be used for investigating laser interaction with solid and adhesion of diamond was commercially available cemented carbide tool inserts (Kennametal, K313 grade: WC-6%Co-0.5%Cr₃C₂). These tool inserts (M10-M20/K05-K15, C3-C4 class) are normally designed for machining nonmetals, nonferrous metals including aluminum, stainless steel, cast irons and most high-temperature alloys including titanium [Bro92, Kenna]. These samples were $\frac{1}{4}$ inch square and $\frac{1}{8}$ inch thick (Kennametal: SPG422, ISO: SPGN 120308). Most samples used in these experiments were made with dimensions of $\frac{1}{4}$ inch x $\frac{1}{4}$ inch x $\frac{1}{8}$ inch thick. Various laser pulses at a certain energy were employed to create surface modification. Then, etching/heat treatment and diamond seeding were applied to the surface modified samples. Diamond films were synthesized in HFCVD system and characterized.

Laser Setup for Surface Modification

Surface modification of the cemented carbides was performed with a Lambda Physik LPX 305 KrF excimer laser ($\lambda=248$ nm, pulse duration=25 ns). Figure 3.1 shows the schematic drawing of laser setup for surface modification. The beam was collimated using a long focal length (200 cm) lens. All lenses used in this study were made of UV-grade fused silica. The primary beam was reflected off the primary path using standard laser mirrors, with the laser beam incident at an angle of 45° with respect to the normal to the mirror. The beam was then focused using focusing lenses. The focusing lenses were either a cylindrical lens (focal length: 8 cm) for obtaining a line beam (~30 mm x 0.2 mm) or a spherical lens (focal length: 20 cm) for obtaining a rectangular beam (~3 mm x 1.7 mm). The samples were mounted on a X-Y translation stage driven by a motor with variable speed. Total energy was measured just after the focusing lens to incorporate energy loss through lenses. All energy measurements were done with a Gentec Sun Series EM-1 laser energy meter equipped with a Gentec ED-500 head. Laser Energy losses were ~10% for the collimating lens, 18.5% for the mirror, and 16.5% for the cylindrical lens.

Briefly discussing about fundamentals of general excimer laser systems, the usual range of laser wavelengths is from

200 nm to 400 nm (F_2 : 157 nm, ArF: 193 nm, KrF: 248 nm, XeCl: 308 nm, and XeF: 351 nm). Absorption coefficients of most materials used in laser work tend to increase as one moves to short wavelength end of this range and the penetration depths in the target materials are correspondingly reduced [Gre94]. The stronger absorption at the short wavelength results in a decrease in ablation fluence thresholds as well as thinner ablation layer of targets. Among various excimer laser systems, KrF is the highest gain system for electrically discharged pumped excimer lasers and is the popular choice in laser community. Excimer lasers are a family of gas lasers that emit powerful ultraviolet pulses lasting from a few nanoseconds to hundreds of nanoseconds. The usual active medium is a gas mixture containing a rare gas (Kr, Ar, or Xe) and a halogen (F_2 or HCl), which combine to form a short-lived rare-gas halide molecule through avalanche electric discharge excitation [Hec92]. Once the excimer is formed, it will decay via spontaneous emission and collisional deactivation. KrF laser system typically consists of ~3.5% Kr, ~0.1% F and the remainder neon as a buffer gas to mediate energy transfer with total gas pressure of ~3.5 atm. Some of the more important reactions for the case of KrF are listed below [Gre94].





The asterisk(*) denotes an electronically excited species and X denotes a third body (He, Ne).

Laser pulses with energy densities near the ablation threshold were employed to modify the surfaces of cemented carbide substrates. Number of laser pulses per unit area was controlled by repetition rate in the range of 1 to 50 Hz and scanning speed of samples in the range of 0.2 mm/min to 4.5 mm/min.

Etching Treatment

Once the micro-rough structures are formed on the surface of WC-6%Co by laser treatment, etching treatments were employed to reduce the amount of cobalt at the surface of inserts, preventing the formation of graphite interlayer. Although various etching agents have been reported before [Kik87, Gra93, Par93, Ike96], nitric acid (HNO_3) of 35% concentration was used in this study. Tungsten carbide also was etched using Murakami agent ($\text{K}_3\text{Fe}(\text{CN})_6$: NaOH : $\text{H}_2\text{O} = 1 : 1 : 10$ by weight) to increase the surface area and to obtain better contact with diamond as has been reported elsewhere [Gra93, Deu96]. Etching treatments were performed either by a stirring method or by an ultrasonic method. The stirring

method involved a magnetic stir plate on which a beaker of 600 ml capacity filled with an etching solution of 300 ml was put. Two centimeter length magnetic bar was used to stir etching solutions at around 900 rpm for 0-120 minutes for nitric acid etching and for 0-5 minutes for Murakami agent etching. The ultrasonic method involved the use of ultrasonic bath. A beaker filled with an etching solution was immersed into ultrasonic bath for 0-45 minutes for nitric acid etching and for 0-2 minutes for Murakami agent etching. After etching treatments, samples were rinsed with water and acetone.

Diamond Seeding Treatment

(100) silicon wafers and cemented carbides underwent an ultrasonic microscratch treatment for 1 hour in diamond suspension ($25 \mu\text{m}$ dia. : $0.25 \mu\text{m}$ dia. = 7 : 3 by weight) in acetone, in which diamond powders having large size were used to generate physical damage on the surface of the substrates and submicron diamond powders were used for getting embedded into the damaged surface as seeds. Diamond suspension was found to be well-dispersed in acetone as compared to other organic solvents [Lee96]. Fine scratches and fine diamond seeds on the substrate surfaces have been recognized to be favorable for nucleation of diamond by Shibuki et al. [Shi88] because they provide a better contact between coating and

substrate via enhanced nucleation density and reduced grain size of the deposited diamond particles. After ultrasonic microscratch treatments, samples were ultrasonically cleaned in acetone for one minute.

Hot Filament Assisted Chemical Vapor Deposition

The experiments were carried out in a HFCVD apparatus as shown schematically in Fig. 3.2. The HFCVD chamber was constructed from a six-way stainless steel cross. The reaction chamber sat on one arm and covered the filament and substrate heater; the other five arms were used as feedthroughs for the mechanical pump, power supplies for the filament and substrate heaters, and for the thermocouple. The reaction chamber consisted of a quartz glass tube with a 7 inch diameter and a 11 inch height, sealed by steel flanges on both ends. The substrate was placed on a tungsten-3%rhenium resistive heater (Omega, SUB1000) of 1 inch diameter and 1 inch height which was encapsulated by a molybdenum can. The substrate-heater assembly was supported above the six-way cross on two stainless steel rods supported from the base of the cross. The substrate temperature was monitored by a K-type thermocouple which contacts the back side of the substrate through a center hole made in the stainless heater cap. The tungsten filament (of 0.02 inch diameter, 2 inch

length coiled region, and 5 inch overall length, stranded with 3 wires, wound to a coil of 0.25 inch inner diameter 15 times) was fixed between two copper electrodes and supported by three tungsten hooks for horizontal positioning. The filament was positioned 1 cm above the substrate. The filament temperature was measured optically with a two-color Mikron M90R-2 pyrometer with an accuracy of $\pm 0.7\%$. The mixture of hydrogen and methane gases was controlled by two mass flow controllers and introduced through the top of the reactor. The pressure was measured by a thermocouple gauge and by a pressure diaphragm. The pressure was adjusted to the required value by a roughing valve. The different experimental conditions are summarized in Table 3.1. The deposition rate of diamond was around 0.5 $\mu\text{m}/\text{hr}$.

Briefly explaining about the operating procedure of HFCVD, the substrate was put on the substrate heater first. The chamber was pumped down to below 10 mTorr by mechanical pump and then backfilled with hydrogen gas to the required pressure at certain flow rate in order to prevent any undesired deposition on the substrate surface during temperature increase. Filament temperature was increased to the required value with control of substrate temperature. Once the filament and substrate temperature was stabilized, methane gas was introduced and growth time was counted.

Table 3.1 Diamond deposition conditions

Conditions	Diamond Deposition Experiment	Surface Modification Experiment
Substrate material	(100) Si	WC-6%Co
Methane concentration (vol%)	0-5	1
Total gas flow rate (sccm)	100-500	200
Chamber pressure (Torr)	20-80	20
Filament temperature (°C)	1700-2350	2100
Substrate temperature (°C)	700-1030	960
Filament to substrate distance (cm)	1.0-1.5	1.0
Deposition time (hr)	10	20

Characterization

Various characterization techniques were employed to investigate changes in phase, roughness, internal stress, surface composition, and adhesion characteristics of diamond films and substrates.

Scanning electron microscopy (SEM) was used to observe morphological changes. Transmission electron microscopy (TEM) was used to characterize high-resolution morphologies and structures. X-ray diffraction (XRD) was adopted for crystal structure analysis. Electron probe microanalysis (EPMA) and Auger electron spectroscopy (AES) were employed for composition analysis.

Scanning Electron Microscopy (SEM)

Scanning electron microscopy (SEM) was used to examine the surface structure of the diamond films and substrates with different laser, etching, heat treatment, and deposition conditions. A JEOL JSM-6400 was operated at 15 kV with working distance of 15-20 mm. A focused electron beam is scanned over the specimen. Secondary and backscattered electrons are produced. Detectors measure intensity versus position and display this on a CRT. The backscattered contrast is the result of the dependence of the electron yield on the atomic number changes within the specimen. The secondary contrast is caused by the dependence of the electron yield on the topography.

Surface Profilometry

Surface roughness of diamond films and substrates was measured by TENCOR Alpha-step 500 surface profilometer having a mechanical stylus. The system measures the mechanical movement of a diamond needle stylus as it is made to trace the topography of the surface of the material. Each scan length was maintained at 2000 μm with a scan rate of 200 $\mu\text{m/sec}$. Average peak-to-valley height surface roughness (R_z) values were obtained from averaging three measurements of scanning. R_z is the average height difference between the five highest peaks and five lowest valleys contained within a chosen

evaluation length (ISO 4287) as shown in Fig. 3.3. A peak (valley) is defined as the highest (lowest) point between two crossings of mean line of the profile. R_z is determined by the following formula:

$$R_z = \frac{1}{5} \left(\sum_{i=1}^5 P_i + \sum_{i=1}^5 V_i \right) \quad (3.2)$$

X-Ray Diffraction (XRD)

A Philips APD 3720 X-ray diffractometer was used to analyze phase and structural changes of substrates. A collimated beam of X rays is incident on a specimen and is diffracted by the crystalline phases in the specimen according to Bragg's law ($\lambda=2d \cdot \sin\theta$, where d is the spacing between atomic planes in the crystalline phase). The intensity of the diffracted X rays is measured as a function of the diffraction angle 2θ and the specimen's orientation. The tube generator was operated at 40kV and 20 mA and Cu K α radiation at a wavelength (λ) of 1.540562 Å. X-ray step scan was performed in the range of 20° to 140° with a step size of 0.05° and 1 second integration time per step. Receiving slit of 0.2 was used.

Electron Probe Microanalysis (EPMA)

A JEOL superprobe 733 electron probe microanalyzer was used for qualitative and quantitative elemental analysis on the surface of the samples. The EPMA is based upon bombarding a specimen with a focused beam of energetic electrons to induce emission of characteristic X rays. The high energy electron beam is used to eject core level electrons from the constituent atoms of the material. The ejected core electron leaves a vacancy which can be filled by the de-excitation of a higher level electron. As a consequence of the de-excitation process, X-rays are emitted. The emitted X-rays have an energy which is characteristic of the parent atom. The X rays are measured by an energy dispersive (EDS) or four wavelength dispersive (WDS) X-ray spectrometers.

Auger Electron Spectroscopy (AES)

A Perkin-Elmer PHI 660 Auger electron spectroscope was used to obtain elemental compositional details from the top three or four atomic layers of the samples. With use of an Ar ion sputtering device, the composition distributions as a function of depth were investigated. Briefly discussing about fundamentals of AES, an energetic electron beam is used to eject core level (K) electrons from the material's constituent atoms. The ejected core electron leaves a vacancy which can be filled by the de-excitation of a higher level electron (L).

As a consequence of the de-excitation process, a characteristic quantity of energy can be transferred to another higher level electron (L). This electron can then escape from the atom, and if it is within the top 20 Å of the material, can escape from the surface without undergoing inelastic electron scattering. The emitted electron has an energy which is characteristic of the parent atom.

Transmission Electron Microscopy (TEM)

A JEOL 200CX transmission electron microscope was used to observe micro-morphologies and to do structural analysis of laser modified cemented carbide substrates. The system was operated at 200kV with a resolution of 2.3 Å. The theory of operation is that a thin solid specimen is bombarded in vacuum with a highly focused, monoenergetic beam of electrons. The beam is of sufficient energy to propagate through the specimen. A series of electromagnetic lenses then magnifies this transmitted electron signal. Diffracted electrons are observed in the form of a diffraction pattern beneath the specimen.

TEM samples were prepared for a cross-sectional view to investigate the melt zone of substrate surface induced by laser energy. The film-substrate interface was made parallel to the direction of the electron beam so that the sample was viewed edge-on. Two samples were prepared first. The

materials surfaces of interest were glued together using M-bond and cured for 20 minutes at 100°C. The glued samples were diced into 3 mm thick (on cross-section side) and 1 mm wide strips using a diamond-blade dicing saw. The samples were then mounted to the micropolisher using crystal glue and mechanically polished to a thickness of less than 50 μm thick. The final thinning process was done using the Gatan 600 DuoMill ion milling machine until a hole was made around interface of two surfaces. The ion mill used two 4. kV Ar⁺ ion beam with a total current of 1 mA at milling angle of 12-15°.

Raman Spectroscopy

Two kinds of micro-Raman spectrometers were used to characterize the crystal quality, purity, and residual stress of diamond films. A Renishaw 2000 micro-Raman spectrometer was used to measure the quality of diamond films on silicon substrates at different growth conditions in HFCVD system. The slit width was set at 30 μm and Ar ion laser ($\lambda=514.5$ nm) was operated at 25 mW. Another micro-Raman spectrometer to be used for internal stress analysis of diamond films deposited on laser modified cemented carbide substrates was a Jobin Yvon U1000 double spectrometer. Samples were excited by a coherent Ar ion laser ($\lambda=514.5$ nm) operated at 200 mW. Both spectroscopies had a spectral resolution of 1 cm^{-1} and collected data through a CCD (charge coupled device) detector.

For the measurement of stress distribution around the interface between diamond films and cemented carbide substrates, the laser spot size was set at ~4 μm using a 100X objective lens.

Looking at the fundamentals of Raman scattering [Ber97], the Raman effect in solids is an inelastic scattering of the incident photons by the crystal electrons distributed around the lattice nuclei. In the photon-electron interaction, the incoming photons exchange a quantum of energy with the electrons via the creation or annihilation of lattice vibrations (phonons). As a result, the scattered photons lose or gain an energy quantum depending on whether a phonon was created (Stokes process) or annihilated (anti-Stokes process). In Raman spectroscopy, the energy of the scattered photons is measured; thus, a characteristic value of the vibration energy of a specific material may be obtained. As shown in Fig. 3.4, the sample is irradiated by a monochromatic laser beam of frequency v_i . The incident photons create or annihilate crystal vibrations of frequency v_p , and the observed scattered beam consists of light of frequency $v_i - v_p$ and $v_i + v_p$, respectively. The scattered beam has an additional light component of the same frequency as the incident light (v_i) that arises from the elastic Rayleigh scattering. Raman shift ($\pm v_p$) is measured from the incident beam frequency v_i . Typically, only Stokes Raman shifts are studied because of

their higher intensities.

Raman spectroscopy has been very useful for studying the chemistry and physics of carbon, particularly of CVD diamond films. It is very sensitive to the nature of the carbon bonding such as diamond, graphite, amorphous carbon, etc. Since the Raman scattering efficiency for graphite is typically 50-75 times greater than for diamond, it is easy to qualitatively evaluate the purity of diamond [Wad80, Ber97]. Table 3.2 shows some characteristic Raman peaks of carbon materials.

Table 3.2 Characteristic Raman peaks of carbon materials

Materials	Raman Peak Position (cm ⁻¹)
Diamond (cubic)	1332 (first order) 2458 (second order)
Microcrystalline diamond	~1140
Diamond (hexagonal, Lonsdaleite)	1315-1326
Diamond-like or amorphous carbon	~1345-1360 (D band) ~1520-1555 (G band)
Graphite	1580 (first order) 3240 (second order)
Microcrystalline graphite	1355, 2710 (second order)

Diamond has sp³ (covalent) bonding while graphite has sp² bonding (intraplanar, covalent) with π bonding (interplanar, van der Waals). Although the interplanar bonding (π) in

graphite is very weak, the intraplanar c-c bonding (sp^2) in graphite is considerably stronger than the c-c bonding (sp^3) in diamond. That is the reason why the Raman peaks due to sp^2 or graphite bonding occur at higher frequencies than 1332 cm^{-1} . When small graphite microcrystallites form or when bond-angle disorder is introduced, the graphite or G line shifts down to lower frequencies and broadens. Diamond-like carbon (DLC) is a mixture of sp^2 bonding and sp^3 bonding with some amount of hydrogen. The G peak arises from changes in connectivity and from a decrease in average bond angle. The D peak is caused by the lack of long-range order [Bee84]. It is not easy to differentiate between DLC and microcrystalline graphite because both Raman peaks are overlapping and very broad, and because DLC also contains some amounts of graphite.

Indentation Adhesion Test

The adhesion strength was evaluated from Rockwell-C point indentation with a Brale diamond indenter [Kuo90, Sai90, Nes95, Chi81, Jin87]. The Rockwell C diamond indenter has a spherocoinal shape with 120° tip angle. Indentation loads of 60, 100, and 150 kg were applied and delamination diameters were measured for each load.

The indentation adhesion test involves introducing a mechanically stable crack into the coating-substrate interface

by the use of conventional indentation procedures. Therefore, this method is fairly common and convenient for estimating qualitatively the relative adhesion of films before conducting an expensive machining test these days. According to Chiang et al. [Chi81], the semianalytical relationship between the measured crack length (c) and the applied load (P) is given by

$$c = \alpha [1 - (P_{cr} / P)]^{1/2} P^{1/4} \quad (3.3)$$

where

$$\alpha^2 = \frac{\alpha_1 t^{3/2} H^{1/2}}{K_{ic}} \quad (3.4)$$

α_1 is a numerical constant, P_{cr} is the critical stress for crack initiation, t is the coating thickness, H is the mean hardness, and K_{ic} is the fracture toughness of the coating/substrate interface. Figure 3.5 shows the schematic representation of the indentation adhesion test. At low loads the coating deforms with the substrate. However, if the load is sufficiently high, a lateral crack is initiated and propagates along the film-substrate interface, leading to debonding of the coating. The lateral crack length increases with an increase of the indentation load. The minimum load at which coating fracture is observed is called the critical load, P_{cr} . The slope of the linear part of the lateral crack

length versus indentation load curve is related to the indentation fracture toughness parameter K_{Ic} , which has correlation with the crack propagation.

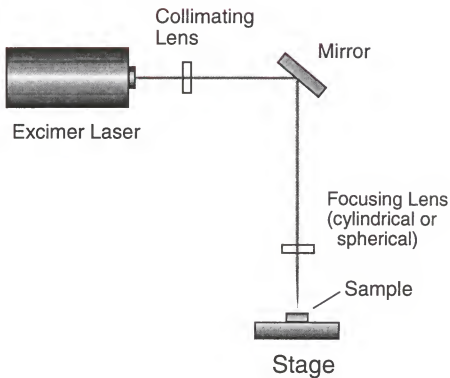


Figure 3.1 Schematic drawing of laser setup for surface modification.

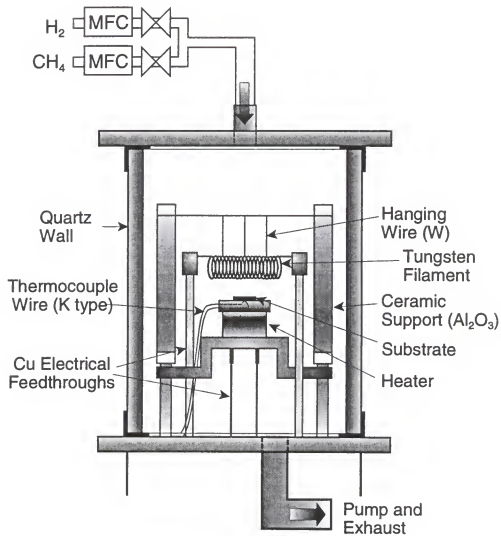


Figure 3.2 Schematic drawing of Hot filament assisted chemical vapor deposition system for diamond synthesis.

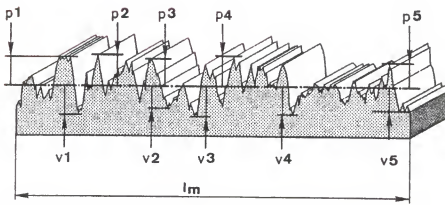


Figure 3.3 Derivation of average peak-to-valley height roughness (R_z).

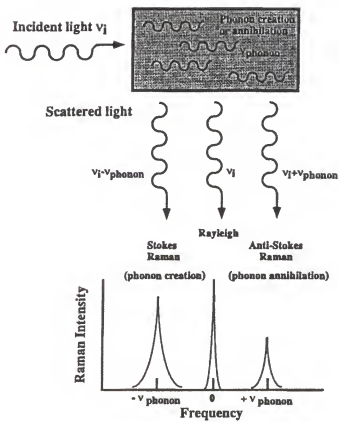


Figure 3.4 Schematic Raman scattering spectrum showing Raleigh line, Stokes Raman scattering and anti-Stoke Raman scattering [Ber97].

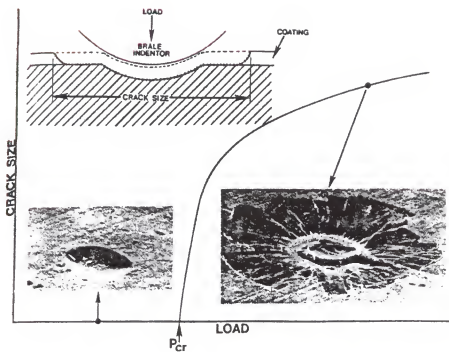


Figure 3.5 Schematic representation of the indentation adhesion test [Jin87].

CHAPTER 4 RESULTS AND DISCUSSION

Growth of Diamond Thin Films

The depositions of diamond films on (100) silicon substrates were carried out to observe the effect of process parameters on the quality of diamond films in HFCVD system and then to optimize the deposition conditions.

Gas Flow Rate and Chamber Pressure

Figure 4.1 shows the surface morphology changes of diamond films with variations of gas flow rate and chamber pressure. Substrate and filament temperature were maintained at 925°C and 2035°C, respectively. The error range of the filament temperature was $\pm 0.7\%$. The methane concentration in hydrogen gas was kept at 1.0% and the distance between filament and substrate was 1 cm. As shown in Fig. 4.1, all the diamond films grown in these ranges had typically cubo-octahedral shapes with {100} facets and {111} facets. As the gas flow rate and chamber pressure were increased, the grain size of diamond films decreased and microcrystalline forms of diamonds with graphite impurities increased.

Growth parameter (α) was measured from the SEM images of diamond films by roughly comparing the edge dimension of {111} crystal faces with that of {100} crystal faces. Wild et al. [Wil93b] defined growth parameter (α) as

$$\alpha = \frac{V_{100}}{V_{111}} \cdot \sqrt{3} \quad (4.1)$$

where V_{100} and V_{111} are the growth rates on the {100} and {111} faces. The dependence of the crystal shape on α is shown in Fig. 4.2. The facets that appear on a crystal are those for which the normal growth velocity is the slowest. When α is varied from 1 via 1.5 to 3, the largest diameter and therefore the direction of fastest growth varies from <111> via <110> to <100>. When $\alpha \leq 1$, diamond crystals grow in the form of cubes. When $1 < \alpha < 3$, they grow in the form of cubo-octahedra. When $\alpha \geq 3$, they grow in the form of octahedra [Wil93b].

From observing the changes in surface morphologies with chamber pressure and gas flow rate, only diamond films grown at 20 Torr with 100-200 sccm had a growth parameter of ~0.7. The rest of diamond films within these ranges had a growth parameter of ~0.5. This pressure range and gas flow rate did not have much effect on the fastest growth direction of diamond crystals. If any, with an increase in gas flow rate and chamber pressure, the {100} crystal faces increased.

Figure 4.3 shows the three-dimensional contour plot of ratio of the integrated intensity (I_d) of Raman diamond peak

(1332 cm⁻¹) to the integrated intensity (I_g) of Raman graphite peak (broad band at around 1580 cm⁻¹). With an increase in gas flow rate and chamber pressure, I_d/I_g values decreased, i.e. impurities such as graphite increased.

Critical parameters to control diamond crystal quality and impurities in HFCVD systems are the concentrations of atomic hydrogen as well as various hydrocarbon species. Dissociation rate of molecular hydrogen and recombination rate of atomic hydrogen play an important role. The dissociation rate of hydrogen gas increases markedly with increasing the filament temperature above 2200 K and decreases with increasing the chamber pressure [Set89] as shown in Fig. 4.4. The recombination rate of atomic hydrogen increases with increasing chamber pressure [Bru93] because of higher collision rate. The gas velocities inside chamber as a function of pressure and gas flow rate were approximately calculated in order to understand the reaction mechanism. By Boyle's and Charles' law,

$$\frac{P_1 V_1}{T_1} = \frac{P_2 V_2}{T_2} \quad (4.2)$$

Feed gases are introduced into hot chamber (T_2) with some volume (V_1) per minute (i.e. V_1 sccm). Here, standard cubic centimeter per minute (sccm) indicates the gas flow rate at standard temperature and pressure (STP; 0°C, 1 atm). The

introduced gases are expanded to V_2 per minute because high temperature is induced from hot filament and substrate, and pressure (P_2) is below 1 atm. V_2 can be easily calculated from the known values P_1 (=760 Torr), T_1 (=273 K), V_1 , P_2 , and T_2 . From (4.2),

$$V_2 = V_1 \left(\frac{P_1}{T_1} \right) \left(\frac{T_2}{P_2} \right) \quad (4.3)$$

Gas velocity, v , is obtained by dividing V_2 by cross-sectional area A of chamber. The diameter of HFCVD chamber was 17 cm.

$$\begin{aligned} v(\text{cm/sec}) &= \frac{\left(\frac{V_2}{60} \right)}{A} = \frac{\left(\frac{V_2}{60} \right)}{\left(\pi d^2 / 4 \right)} \\ &= V_1 \left(\frac{1}{15\pi d^2} \right) \left(\frac{P_1}{T_1} \right) \left(\frac{T_2}{P_2} \right) \\ &= V_1 \left(\frac{1}{15\pi 17^2} \right) \left(\frac{760}{273} \right) \left(\frac{T_2}{P_2} \right) \\ &= 2.044 \times 10^{-4} V_1 \left(\frac{T_2}{P_2} \right) \end{aligned} \quad (4.4)$$

where units of V_1 , T_2 , P_2 are sccm, K, and Torr, respectively.

Figure 4.5 shows the calculated gas velocity as a function of pressure and gas flow rate. Average chamber temperature was assumed to be 800°C. Gas velocity decreased with increasing the chamber pressure as shown in equation (4.4) and increased with higher gas flow rate. For the growth of high-quality diamond films, optimum gas velocity is

required in order to obtain enough time for dissociation of molecular hydrogen into atomic hydrogen on hot surface of filament. The triangular region in the range of 20-50 Torr and 100-200 sccm is the condition for growing high quality diamond film with $I_d/I_g > 0.5$. The best-quality diamond was obtained at 20 Torr with 200 sccm and at 40 Torr with 100 sccm. The other hatched region showed the low-quality diamond with $0.25 < I_d/I_g < 0.5$. From calculations, the gas velocity in the range of 1-3 cm/sec at around 20-40 Torr was optimum. As the chamber pressure is lowered toward 20 Torr, the amount of atomic hydrogen increases as shown in Fig. 4.4. In low pressure regime (around 20-30 Torr), the larger amount of atomic hydrogen helps more in high-quality diamond. However, with higher flow rate in this pressure regime, gas velocity increases to around 6 cm/sec and contact time of molecular hydrogen with filament for dissociation reaction is shorter. That means a decrease in the dissociated atomic hydrogen at higher flow rate, resulting in increasing the amount of graphitic carbon. In higher pressure regime (around 60-80 Torr), although the contact time of gas with filament is high enough due to slowly moving gas, the recombination rate between the activated gases and the unactivated gases is increasing, finally reducing the amount of the dissociated atomic hydrogen.

The diamond films were grown at different substrate temperatures with various chamber pressures as shown Fig. 4.6. The 1% methane in hydrogen was used with a gas flow rate of 200 sccm and the distance of filament to substrate was kept at 1 cm. The diamond grain size was relatively larger at higher substrate temperature (1000°C). Like the phenomena with pressure shown in Fig. 4.1, the diamond grain size also decreased with increasing pressure. At a chamber pressure of 20 Torr, the growth parameter of diamond was changed from 1.7 at a substrate temperature of 925°C to 1.5 at a substrate temperature of 1000°C. At chamber pressures over 20 Torr, the growth parameters of diamond were all 1.5 irrespective of substrate temperature. Shown in Fig. 4.7 is the dependence of diamond quality (I_d/I_g) on chamber pressure at different substrate temperatures. As described in Fig. 4.3, the quality of diamond films grown at a substrate temperature of 925°C decreased with increasing chamber pressure. However, the quality of diamond films grown at higher substrate temperature of 1000°C was very low compared to diamond films grown at 925°C and did not change much with pressure. The effect of substrate temperature will be explained later.

Methane Concentration

Methane concentration in hydrogen was changed from 0.5% to 5%. The filament and substrate temperature were maintained

at 2035°C and 960°C, respectively. The chamber pressure was kept at 20 Torr with a gas flow rate of 100 sccm and a filament-substrate distance of 1 cm. Figure 4.8 shows the SEM images of diamond films grown using different methane concentration. At a methane concentration of 0.5%, the diamond grain size was smaller compared to the one grown using 1% methane. The reason for the grain size difference is not clear. The growth parameter of diamond films was changed from 1.25 to 1.5 when the methane concentration increased from 0.5 to 1. Lower methane concentration favored {100} faces. This observation was not consistent with the other reports [Bad88, Spi81]. With further increase in methane concentration from 2% to 5%, the facets of diamond crystal began to disappear, forming smaller ball type features. Above 2% methane concentration, significant deposition of graphite was found on the surface of hot filament. This observation is in accordance with other reports [Cel92, Som90]. Celii et al.[Cel89] reported that a sharp drop in atomic hydrogen production with greater than 3% methane fraction, below 2200°C was due to carbon condensation on the filament, which caused a poisoning of the catalytic dissociation by the filament as shown in Fig. 4. 9. The role of the hot tungsten filament is to dissociate molecular hydrogen into atomic hydrogen [Lan12]. It was reported that the dissociation process involves the adsorption of molecular hydrogen on the tungsten surface

followed by evaporation of atomic hydrogen back into the gas phase [Hic60]. Figure 4.10 shows the Raman spectra of diamond films for different methane concentrations. At 0.5% methane concentration, the Raman peak of diamond at 1332 cm^{-1} was sharp and strong. Above 2% methane concentration, the diamond peak disappeared and the amorphous carbon peak at 1344 cm^{-1} and graphite peak at 1587cm^{-1} significantly increased. According to Frenklach et al [Fre91], the increase in the methane concentration causes an increase in the formation of aromatics and a decrease in the atomic hydrogen concentration.

Filament Temperature

The filament temperature is one of the critical factors controlling the quality of diamond films because gas activation is strongly affected by filament temperature. Figure 4.11 shows the SEM images of diamond films as a function of filament temperature at two different substrate temperatures. The chamber pressure was maintained at 20 Torr with a gas flow rate of 100 sccm using 1% methane in hydrogen. Filament to substrate distance was varied because of limitation in control of filament and substrate temperature. Figure 4.11 (a), (c), and (e) shows the diamond films grown at substrate temperature of 925°C with filament-substrate distance of 1.5 cm and Fig. 4.11 (b), (d), and (f) shows the diamond films at substrate temperature of 1030°C with

filament-substrate distance of 1.0 cm. The grain size of diamond was smaller at a filament temperature of 1820°C (Fig. 4.11(a)). As the filament temperature increased to 2270°C, the diamond facets became more perfect (Fig. 4.11(e)). The growth parameter changed from 1.25 at 1820°C to 1.75 at 2270°C. That means that {111} plane is more stable with increasing filament temperature. In case of diamond films grown at a substrate temperature of 1030°C, the facets of diamond crystal were good in the range of 2050-2170°C. At a filament temperature (T_f) of 2300°C (Fig. 4.11(f)), the diamond films grown at a substrate temperature (T_s) of 1030°C were different compared to the diamond films grown at $T_s=925^\circ\text{C}$. The facets of diamond became smooth with smaller grain size. The growth parameter of diamond films grown at $T_f=2050-2170^\circ\text{C}$ (Fig. 4.11(b),(d)) was approximately 1.6-1.7. The quality of different diamond films is shown in Fig. 4.12. At $T_f=1820^\circ\text{C}$, the diamond quality grown at $T_s=925^\circ\text{C}$ is low due to low dissociation of molecular hydrogen as shown in Fig. 4.9. The diamond quality was improved as the filament temperature increased up to 2100°C and became constant until 2300°C. This behavior can be explained with some results reported by Celii et al [Cel89, Cel91] The concentration of atomic hydrogen increases with increasing filament temperature (Fig. 4.9). The concentration of methyl radicals also increases due to more dissociation of methane gas induced by larger amount of

active atomic hydrogen with increasing filament temperature up to 2100°C and then reaches a plateau [Cel91]. This phenomenon of gas concentration change exactly explains the diamond quality change shown in Fig. 4.12. The diamond films grown at $T_s=1030^\circ\text{C}$ have large amount of graphite impurities. The reason for this behavior is that the substrate temperature is too high for growing high-quality diamond films. The higher substrate temperature reduces the density of active sites for depositing diamond due to their thermal decomposition and subsequent graphitization at around this temperature (Fig. 4.13). Figure 4.14 shows the Raman spectra of diamond films grown at $T_s=925^\circ\text{C}$ for different filament temperatures. At $T_f=1820^\circ\text{C}$, the Raman peak of diamond was weak with some amount of graphite. The background luminescence (noise) in Raman spectra was also large, which may be caused by defects or impurities such as sp^2 disordered phase [Ber94] or incorporated hydrogen [Bou91]. The background noise decreased and the diamond peak increased as the filament temperature was raised. The Raman spectra for the diamond films grown at $T_s=1030^\circ\text{C}$ is shown in Fig. 4.15. As the filament temperature increased, the diamond peak also became small and the amorphous and graphitic carbon increased.

Substrate Temperature

The effect of substrate temperature on diamond growth was observed. Figure 4.16 shows the SEM images of diamond films for different substrate temperatures at two different pressures and flow rates. One series of diamond films was grown at 20 Torr with 100 sccm (Fig. 4.16 (a)(c)(e)(g)). Another series of diamond films was grown at 30 Torr with 200 sccm (Fig. 4.16 (b)(d)(f)(h)). The filament-to-substrate distance was maintained at 1 cm. The changes in Raman peak intensity ratio (I_d/I_g) for these diamond films are shown in Fig. 4.17. The difference in diamond grain size grown at different pressure and flow rate was larger at 900°C (Fig. 4.16 (a) and (b)) and smaller with increasing substrate temperature to 1000°C (Fig. 4.16 (g) and (h)). The diamond grains grew bigger with increasing substrate temperature due to larger growth rate at higher temperature. Looking at diamond quality from Fig. 4.19, the diamond quality grown at $T_s=925^\circ\text{C}$ was best in both conditions and decreased from $T_s=925^\circ\text{C}$ to 1030°C . The reason for the decrease in diamond quality with higher temperature can be explained by Frenklach et al. [Fre91] who developed a kinetic model for various reactions in HFCVD reactor as shown in Fig. 4.13. At low substrate temperatures, condensation of benzene from the gas phase onto the growing surface competes with the diamond

growth process by covering the available sp^3 diamond sites. The condensing aromatic molecules are then converted into an amorphous sp^2/sp^3 carbonaceous network by the addition reactions of hydrogen atoms [Fre91]. Because of low substrate temperature, hydrogen abstraction rate from substrate surface is slow , i.e. the formation of active sites is slow. At temperature above 1050°C, sp^2 carbon formation is enhanced due to the thermal decomposition and subsequent graphitization of substrate surface radicals. The quality of diamond films grown at 20 Torr with 100 sccm was better than those grown at 30 Torr with 200 sccm. The reason is, as discussed earlier, the difference in the concentration in atomic hydrogen as well as gas contact time with hot filament. The changes in growth parameters within this substrate temperature range were little. The growth parameters of diamond films grown at 20 Torr with 100 sccm was 1.7, and the growth parameter of diamond films grown at 30 Torr with 200 sccm was 1.5.

The other series of diamond growth was performed as shown in Fig. 4.17. The filament to substrate distance was changed to 1.5 cm in order to obtain more temperature flexibility. The filament temperature was kept at 1950°C. A low filament temperature of 1800°C was used to grow diamond films at $T_s=700^\circ\text{C}$ (Fig. 4.17(a)) because the substrate temperature was also affected by the filament and could not be lowered with a filament temperature of 1950°C. In the substrate temperature

range of 700 to 1000°C, the change in growth parameter was distinctive from 2 at 700°C to 1.25 at 1000°C. That means that the {100} crystal faces favored high substrate temperature while the {111} crystal faces favored low substrate temperature. The results were consistent with other reports [Mat82, Bad88, Spi81]. However, the reasons for the different preferable growth faces for different conditions are not cleared. The grain sizes deposited at $T_f=1950^\circ\text{C}$ with filament-substrate distance of 1.5 cm were generally smaller than the ones deposited at $T_f=2035^\circ\text{C}$ with filament-substrate distance of 1.0 cm. This difference in grain size may be related to the low concentration of activated species due to the more recombination of atomic hydrogens resulting from the longer distance of filament-substrate and lower filament temperature. From Fig. 4.19, the diamond quality for $T_f=1950^\circ\text{C}$ with longer separation distance was better than that at $T_f=2035^\circ\text{C}$ with shorter separation distance. The filament-substrate distance did appear to be affecting the quality of diamond films in this low pressure regime with low flow rate. It is speculated that the relative concentration of the atomic hydrogen and methyl radicals may be different for different filament-substrate distance. The relative amount of methyl radicals to H atoms arriving on the substrate with a separation distance of 1.5 cm may be smaller compared to the ones at shorter separation distance. This is probably due to higher

recombination rate of methyl radicals with respect to the one of H atoms by molecular weight difference. Owing to the difference in relative concentrations of methyl radicals to H atoms, the diamond quality may be higher. And the growth rate of diamond films at longer separation distances is expected to be small, making grain size also smaller. Figure 4.18 shows the SEM images of diamond films when the filament temperature was changed without controlling substrate temperatures independently. The substrate temperature measured here was controlled solely by the energy of hot filament. The filament-substrate distance was kept at 1 cm. The feed gases of 1% methane in hydrogen were introduced at a flow rate of 100 sccm with pressure of 20 Torr. At $T_s=700^\circ\text{C}$ (Fig. 4.18(a)), the filament temperature was 1700°C . The diamond films became structureless and had a lot of impurities and graphitic carbon as shown in Fig. 4.19 because of low activation of hydrogen molecules at low filament temperature, less amount of active substrate sites for depositing diamond, and the condensation of polycyclic aromatic hydrocarbons. At $T_s=800^\circ\text{C}$, for which filament temperature was 1900°C (Fig. 4.18(b)), the facets of diamond crystallites began to appear and the diamond quality increased a little. At $T_s=900^\circ\text{C}$, for which filament temperature was 2010°C , the quality of diamond films began to significantly improve because of higher dissociation rate of molecular hydrogen and substrate surface activation. The diamond

quality peaked at $T_s=900\text{-}960^\circ\text{C}$ with $T_f=2010\text{-}2080^\circ\text{C}$. With further increase in substrate temperature to 1030°C and filament temperature to 2350°C , the diamond quality decreased due to contributions of both temperatures as shown in Fig. 4.19. As mentioned before, the sp^2 formation is enhanced at high substrate temperature. At filament temperatures above 2100°C , the formation of acetylene(C_2H_2) gas starts to increase, which may be the precursor of graphitic and amorphous carbon [Kaw87].

Summary

All the process parameters for growing diamond films in HFCVD system were investigated.

The conditions for growing good-quality diamond films in HFCVD system are following:

Chamber pressure: 20-30 Torr

Gas flow rate: 100-200 sccm

Methane concentration in hydrogen: $\leq 1\%$

Filament temperature: $1800\text{-}2280^\circ\text{C}$

Substrate temperature: $900\text{-}980^\circ\text{C}$.

The shapes of diamond crystals grown using these growth conditions were all cubo-octahedra. At high substrate temperature and chamber pressure, and at low filament temperature and methane concentration, {100} crystal faces were favored (in other words, growth parameter decreased).

{111} crystal faces were favored at reverse conditions. The effect of chamber pressure and methane concentration on growth parameter was weak while the filament and substrate temperature affected the growth parameter to some extent. Table 4.1 shows the growth parameters for different substrate and filament temperatures.

Table 4.1 Changes in growth parameters with substrate and filament temperature (gas concentration 1% CH₄ in H₂; chamber pressure 20 Torr; gas flow rate 100 sccm; filament-substrate distance: 1 cm)

Fila. Sub. temp. (°C)	1800	1900	2000	2100	2200	2300
	2*					
700	2*					
800			1.5			
900		1.25*	1.5	1.7	1.7*	1.75*
1000			1.25	1.7	1.65	1.65

* filament-substrate distance=1.5 cm.

Laser-Cemented Carbide Interaction

The interaction between cemented carbide tool substrate and laser beam was investigated to understand the mechanism of surface modification. Cemented carbide (WC-6%Co) tool

materials were used as substrates as shown in Fig. 4.20. As-received cemented carbides had grinding streaks on surfaces and had an approximate average peak-to-valley height roughness (R_z) of 1 μm (Fig. 4.20(a)). Cemented carbides consisted of 1 μm size of irregular tungsten carbide particles and cobalt binder around them (Fig. 4.20(b)).

Evolution of Surface Feature by Laser

Pulsed nanosecond lasers are a unique and useful tool for processing the shallow surfaces of bulk materials. They can generate high temperatures in the surface regions for very short time without affecting the bulk properties. Ultrarapid heating and solidification induced by high-intensity laser pulses can lead to the formation of novel compounds and metastable alloys. The photon energy from laser is transferred to heat very quickly (< 1 ps), giving rise to intense thermal effects on the surface of the irradiated material. The processing times are generally extremely short (~100 ns). The heat generated by the laser is determined mainly by the optical properties (reflectivity and absorption coefficient) and thermal properties (thermal conductivity, density, melting/evaporation temperature, and specific heat capacity) of the substrate materials, and the laser properties (wavelength and energy density). This heat causes melting, evaporation, and solidification of materials which is shown

schematically in Fig. 4.21. The laser energy is absorbed over a finite depth called the absorption depth which is the inverse of the absorption coefficient, and melting and vaporization begin (Fig. 4.21(a)). The melt front propagates into the solid, accompanied by vaporization (Fig. 4.21(b)) during pulsed irradiation. After termination of the laser pulse, solidification begins and the melt front recedes to the surface (Fig. 4.21(c)). Then solidification completes (Fig. 4.21(d)) [Fol94].

In order to estimate the surface temperature of cemented carbide, SLIM (Simulation of Laser Interactions with Materials) program developed by Singh et al. [Sin92] was used. Table 4.2 shows the input parameters for running SLIM program. The oversimplified simulation assumes not only a single laser pulse irradiation on tungsten carbide and cobalt, respectively but also assumes no interactions between tungsten carbide and cobalt. The simulated surface temperatures of tungsten carbide and cobalt, respectively as a function of laser fluence are shown in Fig. 4.22. At a laser fluence of 2 J/cm^2 , the estimated temperatures of tungsten carbide and cobalt reach approximately the melting temperature (2993 K) of tungsten carbide and the boiling temperature (3143 K) of cobalt, respectively.

Table 4.2 Input parameters for SLIM.

	WC	Co
.Density (g/cm ³)	15.7	8.8
.Melting	2993	1768
Temperature (K)		
.Heat of Melting (J/cm ³)	3020	2295
.Reflectivity	0.51	0.41
.Absorption Coefficient (cm ⁻¹)	1.4×10^6	9.3×10^5
.Thermal Conductivity (W/cm·K)	0.121 (room-1100K) 0.31 + $1.15 \times 10^{-4} T$ (1100-2993K) 0.7 (liquid)	$1.11 - 9.91 \times 10^{-5} T$ $-1.57 \times 10^{-6} T^2$ (room-430K) 0.793 (430-1768K) 0.7 (liquid)
.Heat Capacity (J/cm ³ ·K)	$-2.08 + 2.38 \times 10^{-2} T$ $-2.84 \times 10^{-5} T^2$ $+1.14 \times 10^{-8} T^3$ (solid) 121 (liquid)	$2.19 + 6.54 \times 10^{-3} T$ $-6.15 \times 10^{-6} T^2$ $+3.08 \times 10^{-9} T^3$ (solid) 11.5 (liquid)

In this study, a laser fluence of 2 J/cm² with various number of pulses was used to obtain micro-rough structure of substrates. The development of surface features with increasing laser pulses was observed in static mode (no movement of the sample position) and dynamic mode (movement of sample position) during laser irradiation. Figure 4.23 shows the changes in surface morphologies of cemented carbides as a function of laser pulses having a rectangular shape (~3 mm x 1.7 mm) in static mode. After 2 pulses (Fig. 4.23(a)), the grinding streaks on the as-received substrate which is shown in Fig. 4.20(a) started disappearing with the uniform shallow

melting of surface. Small pits (or craters) normally formed along the grinding streaks on the surface. On increasing the number of pulses to 20 (Fig. 4.23(c)), the number of small pits significantly increased to combine together and to form a net, and the grinding streaks almost disappeared. Small pits might be caused by the evaporation of cobalt and consequent expansion of vapor, making craters, as expected from the computer simulation (Fig. 4.22). This net consisting of small pits appears to be the main source for periodic micro-roughness on cemented carbide surface. Once the pits formed a net, further laser pulses would interact more with these pits, etch away more, and make valley regions as shown in Fig. 4.23(d). In Fig. 4.23(d), the surface feature began to develop the peak and valley regions with less number of pits. The surface cracks also developed in between peaks and valley regions due to the repeated cycle of ultrafast heat/cooling ($\sim 10^{11}$ K/sec) and surface tension. The developed peak/valley regions enhanced the roughness with increasing the number of pulses to 300 (Fig. 4.23(e)-(f)). When a laser light impinges on the rough surface, it is scattered at peak regions while it is collected at valley regions due to geometrical effects. Therefore, more intense laser light irradiates the valley regions as compared to the peak regions, causing more melting/evaporation at the valley regions. The roughness changes as a function of the number of laser pulses

are shown in Fig. 4.27. The development of surface roughness was slow until around 120 pulses. Above 120 laser pulses up to around 900 pulses, the surface roughness developed fast due to the predeveloped periodic structure. At 450 laser pulses (Fig. 4.23(g)), the periodicity of micro-roughness was destroyed because the melted surface started to peel off. Because laser irradiation in static mode processed modification over large area, larger melt would be likely to produce more stress to the boundary of melted-unmelted regions when it is solidified. The repeated shockwave of laser pulses would probably break down the weak interface. Then the peeled portion of modified regions rebonded together (Fig. 4.23(h)). The peeling and bonding repeated up to around 900 pulses. Above 900 pulses, peeling did not occur because of the thick melted modified area and the surface roughness became almost constant.

In contrast to the static mode, surface features were observed during laser irradiation using a line beam (30 mm x 0.2mm) in dynamic mode (Fig. 4.24). As in the static mode, a lot of small pits were formed and developed periodic rough structure having around ten micron periodicity at initial stage up to 40 pulses (Fig. 4.24 (a)-(c)). The periodicity of surface features also changed from 10 μm (40-80 pulses) to 30 μm (>304 pulses) with larger areas of peak regions. The periodicity of surface features was not destroyed even at high

number of pulses probably because the laser beam was so narrow that it only modified a local area at one time with lower thermal stress compared to large area laser irradiation. However, some peeling of modified layer was still observed at 675 pulses (Fig. 4.24(h)). Owing to the predeveloped surface features, the roughness of the modified surface increased at faster rate from 1 μm to 12 μm in the range of 40 to 800 pulses (Fig. 4.27). At the conditions above 675 pulses, the peak regions of the periodic structures started to significantly melt and evaporate. The reason is that the area of peak regions became wider while valley regions were deep and narrow not enough to modify. The peak regions became sharper because the top of peak area is hard to modify due to higher scattering of laser light (Fig. 4.24(i)-(j)). After the sharp edge in peak regions is thin enough to interact with laser, then it melted and formed spherical shapes (Fig. 4.24(k)-(l)). As seen from Fig. 4.27, the surface roughness of modified structures was maximum at 1350 pulses, at which sharp edges of the peak regions existed. The surface roughness decreased with further increasing laser pulses to 3040 because of melting of sharp edges too. The surface roughnesses of modified structures in dynamic mode were a little bit higher than the ones at static mode probably due to moving force of shockwave in dynamic mode. The moving speed of samples during laser irradiation was changed to observe any

effects on the surface roughness. The surface roughness slightly increased with increasing the moving speed of samples. This evolution of surface features as a function of laser pulses is schematically drawn in Fig. 4.25.

The evolution of surface features of etched cemented carbides with no cobalt binder on the surface when irradiated with laser pulses at static mode was also observed as shown in Fig. 4.26. The evolution behavior of etched cemented carbides was fairly different from that of unetched cemented carbides. The etched surface of cemented carbides consisted of mostly loosely-bound tungsten carbide (WC) particles. Owing to loosely-bound tungsten carbide particles with a lot of pores, the laser photon can easily penetrate through pores and interact with more WC particles, inducing more melting. Even two laser pulses lead to a considerable melting on substrate surface, shaping spheres due to surface tension of melt (Fig. 4.26(a)). The spherical melts grew larger due to more interaction of laser with substrate and merging of small melts at 5 pulses (Fig. 4.26(b)). At 10 laser pulses, the melts of carbide substrate induced by laser began to interconnect to form a two-dimensional network of melts (Fig. 4.26(c)). Then this 2-D network developed into periodic rough structures with increase in the laser pulses (Fig. 4.26(d)-(f)). The peeling-rebonding process was also observed locally (Fig. 4.26(f)). It was observed that a lot of particles were splashed out from

the substrate surface during the laser processing due to loose bonding of particles with no cobalt. The surface roughness significantly increased with increasing the number of laser pulses (Fig. 4.27).

Around the surface modification, there were some deposits which was brought from the evaporation of substrate materials (Fig. 4.28). Composition analysis through depth was performed on the deposits using Auger spectroscopy as shown in Fig. 4.29. From the depth profile curves, these deposits were considered to be within 12 min sputter time range in this figure. They mostly consisted of cobalt and carbon elements. It means that both cobalt element having low melting/evaporation temperature and carbon element dissociated from tungsten carbide melt were easily evaporated during the laser irradiation. This was fairly consistent with the computer simulation result.

Cross-sections of the laser modified cemented carbides with various laser pulses were observed in Fig. 4.30. Cross-section samples were prepared by cutting, grinding with diamond disk grinder, and polishing with diamond paste. Secondary electron images (Fig. 4.30 (a), (c), (e), and (g)) and backscattered electron images(BEI) (Fig. 4.30 (b), (d), (f), and (h)) were used. With 40 laser pulses at 2 J/cm^2 , the modified surface formed a shallow wave (Fig. 4.30(a)). From BEI of Fig. 4.30(b), tungsten carbide particles of $1 \mu\text{m}$ size

were clearly observed inside the material. However, the top of the modified surface had a uniformly shallow phase-transformed area of $0.3 \mu\text{m}$ depth which is expected to be melt-depth (Fig. 4.30(b)). With 80 laser pulse (Fig. 4.30(d)), the valley regions of the modified surface still had same transformed area as the one modified with 40 pulses (Fig. 4.30(b)) and became deeper. The peak regions had a thick phase-transformed area around $1.3 \mu\text{m}$ deep. With further increase in the number of pulses from 120 to 160, the depth of phase-transformed area at peak regions increased from $2.3 \mu\text{m}$ to $2.8 \mu\text{m}$ while the valley became deeper. Irrespective of the number of laser pulses, the depth of phase-transformed area at valley regions was all same and constant ($\sim 0.3 \mu\text{m}$). The reason is that the valley regions were constantly melted and evaporated.

From this observation, speculation of the formation mechanism of rough surface was possible. Figure 4.31 schematically shows the formation of rough surface. As explained before in Fig. 4.24, with n_1 laser pulses, a wavy feature of cemented carbide develops probably due to the formation of some pits on cemented carbide grain boundary and on grinding streaks. At this stage, the evolution rate of surface feature is slow due to small difference in local laser energy density between peak and valley regions. As the surface roughness of modified structure increases with n_2

laser pulses, difference in local laser energy density between peak and valley regions becomes larger. As seen in the case of n_3 pulses, the laser energy density is larger at valley regions of surface features than the average energy density due to the collection of the diffracted laser beam, resulting from geometrical effects. However, at peak regions, laser light is fairly scattered, making the laser energy density lower. The material removal rate by laser is much faster in valley regions than in peak regions. Thus, it is expected that the removal of substrate materials occurs mainly at valley regions. Although the melting and evaporation of substrate materials occurs all over the surface area, the peak regions acquires redeposition of the evaporated materials coming from the valley regions because evaporation rate is low. As the number of laser pulses increases to n_4 , higher energy at valley regions removes the substrate material at faster rate. Correspondingly, the evolution rate of surface features increases with increasing the number of laser pulses. The valley regions of modified structures will be deeper and the slope of peak-to-valley regions will be also steeper with increase in the number of laser pulses. It is expected that the peak regions consist of layers of deposits. Figure 4.32 shows the low magnification cross-sectional view of modified regions. From Fig. 4.32(b), the melted and redeposited areas can be clearly seen. The boundary between the

melted/redeposited area and unmodified substrate was straight.

Composition and Phase Change by Laser

Composition analysis for laser modified cemented carbides was performed to understand chemical reactions and phase changes during laser irradiation. Shown in Fig. 4.33 are the depth profiles of as-received and laser modified cemented carbides using Auger electron spectroscopy. In case of an as-received cemented carbide (Fig. 4.33(a)), there were high contents of carbon/oxygen and low contents of cobalt/tungsten on the surface. Carbon and oxygen elements on the surface were considered to come from air and cleaning organic solvents such as acetone or alcohols. All the amounts of each element were quite constant. Some minor fluctuations of each element (W, C, and Co) were due to tungsten carbide particles of one micron size and cobalt segregation to the boundary of tungsten carbide particles. Figure 4.33(b), (c) presents the depth profiles from peak and valley regions of cemented carbide substrates modified at 2 J/cm^2 with 120 pulses, respectively. The surface of laser modified structure contained high cobalt/oxygen contents and low tungsten/carbon contents irrespective of the number of laser pulses at 2 J/cm^2 (Fig. 4.33(b), (c), and (e)). In Fig. 4.33(b), the melted/redeposited area at peak regions might be within a sputtering time of 70 minutes from the observation of

composition changes. The ion gun sputter rate in Auger spectroscopy for cemented carbide was considered to be around 300 Å/min. Within the melted/redeposited area at peak regions, higher contents of tungsten were found. Tungsten contents gradually decreased to the composition of tungsten carbide matrix as it went deeper. It presented the formation of other forms of tungsten carbide phase having less carbon content. In Fig. 4.33(c), the compositional conditions at valley surface were the same as the one obtained from peak regions (Fig. 4.33(b)). The gradual change in tungsten content was not observed in this valley regions. The composition profiles of each element were quite similar to the as-received cemented carbide in Fig. 4.33(a). Sudden jumps in tungsten and carbon elements were due to noise of signals. Figure 4.33(d) shows the detailed depth profiles of modified structure at the surface of peak regions. On the surface, (tungsten-cobalt) oxide layer existed within a sputtering time of 6 minutes ($\sim 0.2 \mu\text{m}$) below the oxide layer. The cobalt-rich phase existed in the range of 6 to 16 minutes of sputter time ($\sim 0.3 \mu\text{m}$). The cobalt-rich phase indicated segregation during the melting and resolidification process in the energy-absorbed, melted region. As solidification begins from the melt induced by laser, higher melting point component of the cemented carbide/cobalt liquid such as tungsten carbide freeze first, driving cobalt rich liquid toward the surface. This

type of behavior has also been observed in other reports such as the segregation of Cu or Ba from YBCO superconductor [Ase88] and the segregation of Au from TeO₂ [Mar85]. In case of peak regions of cemented carbide modified at 2 J/cm² with 40 pulses (Fig. 4.33(e)), the formation of tungsten-cobalt oxide and the segregation of cobalt at the modified surface was also observed. Each elemental profile was almost the same as the as-received samples because the modified regions were small as shown in Fig. 4.30(a)-(b). Sudden jump of W and Co at 10 minutes sputter time also appeared to be a signal noise.

X-ray diffraction studies of surface modified cemented carbides were undertaken to identify phases in the melted/redeposited area at peak regions. As-received samples showed typical peaks of tungsten carbide (WC) and cobalt (Fig. 4.34(a)). When a cemented carbide was modified at 2 J/cm² with 40 pulses (Fig. 4.34(b)), another form of tungsten carbide phase (WC_{1-x}, X=0-0.3) formed, which had less carbon content. With further increase in laser pulses to 80, another form of tungsten carbide phase (W₂C) formed, which had much less carbon content. As the number of laser pulses increased, the peak intensity of W₂C phase also increased. From this XRD observation, it is found that carbon element was dissociated in tungsten carbide/cobalt melt during laser irradiation and was evaporated as forms of volatile CO_x gases.

Figure 4.35 shows the SEM images of the

melted/redeposited region at peak regions. A laser modified cemented carbide was cross-cut, polished, and etched with Murakami's agent ($K_3Fe(CN)_6$: NaOH : $H_2O = 1 : 1 : 10$ by weight). As shown in Fig. 4.35(a), the melted/redeposited area at peak regions consisted of microcrystalline grains of 70-100 nm size. From the XRD results in Fig. 4.34, these nanocrystalline grains were considered to be a mixture of WC_{1-x} and W_2C particles. It was found that this melted/redeposited area consisted of multiple layers of nanocrystals (Fig. 4.35(a), (b)). Figure 4.35(c) also presented the surface of the melted/redeposited area which had a lot of nanocrystals compared to one micron size of tungsten carbide matrix particles (Fig. 4.35(d)).

Transmission electron micrographs of melted area of laser modified regions are shown in Fig. 4.36. Like the one obtained from Fig. 4.35, TEM images also showed the same size of nanocrystals. Selected area diffraction (SAD) patterns for the melted area of laser modified regions indicated polycrystals (Fig. 4.35(b)). But it was difficult to analyze the structure because crystal size was too small. It is speculated that these were tungsten carbides with less carbon content. Figure 4.37 shows TEM images of an unmodified tungsten carbide substrate which has a grain size of 0.5-1 μm with hexagonal structure.

In order to observe any compositional changes on the

modified surface, backscattered electron images were used in Fig. 4.38. Backscattered electrons are more sensitive to difference in atomic numbers compared to secondary electrons. Higher atomic numbers give more brightness in images [Gol92]. In Fig. 4.38(b), there were distinctive difference in contrast between peak and valley regions. From magnified view of boundary of modified structure between valley and peak regions in SEI mode (Fig. 4.38(c)), there existed a fuzzy oxide layer mostly deposited on peak regions (on the right side in this figure). Backscattered electron image of Fig. 4.38(c) showed compositional contrast (Fig. 4.39(d)). From cross-sectional view of modified regions (Fig. 4.38(e)), tungsten-cobalt oxide layer of 0.1-0.2 μm thickness was observed. From the observation of BEIs above, it was found that the oxide layer normally formed on peak regions which is the melted/redeposited area, and did not form on valley regions which is normally melted and evaporated. Figure 4.39 shows a schematic drawing of the formation of peak regions of surface modified cemented carbide during laser irradiation. Whole structure of laser modified cemented carbide was illustrated in Fig. 4.40.

Stress Analysis of Diamond Films

After the whole structure of laser modified cemented carbide surface was understood clearly, it was easy to control the surface conditions of cemented carbide substrates before diamond coating.

Residual stress is critically important in thin films because it can overcome the adhesion of a film and caused delamination from a substrate. The total residual stresses in a diamond film deposited on a substrate arise from two types of stress, an intrinsic stress and a thermal stress. The intrinsic stress in diamond films is normally tensile mainly due to attractive atomic forces acting across grain boundaries [Win91]. Impurities and structural defects such as dislocations inside diamond films also affect the intrinsic stress. Graphite inclusions produce compressive stress due to their large specific volume and high internal surface area [Bag92, Zhu89, Win91]. Thermal stress is caused by differences in thermal expansion of diamond film and substrate when the film is coated at high deposition temperature and cooled down to room temperature. Since most materials have a larger thermal expansion coefficient than diamond, the thermal stress of diamond film is mostly compressive, except for fused silica and silicon nitride. The thermal stress can be calculated from the following Hooke's law:

$$\begin{aligned}
 \sigma_{\text{th}} &= E_f' \cdot \epsilon \\
 &= \frac{E_f}{(1-\nu_f)} \int_{293K}^{T_d} (\alpha_f - \alpha_s) dT \\
 &= \frac{E_f}{(1-\nu_f)} (\epsilon_f - \epsilon_s)
 \end{aligned} \tag{4.5}$$

where E_f' ($= E_f / (1 - \nu_f)$) is the biaxial Young's modulus of the film, and α_f , α_s , and T_d are the thermal expansion coefficients of the film and substrate, and deposition temperature, respectively. ν_f is the Poisson coefficient (0.07) of the diamond film, and ϵ_f and ϵ_s are the linear thermal expansions ($\Delta l/l_0$) of the film and substrate, respectively. Young's modulus (E_f) of polycrystalline diamond film is 1143 GPa. Figure 4.41 shows the thermal expansion (ϵ) as a function of temperature for diamond and some other substrates. At a deposition temperature of 960°C, the calculated thermal stress of diamond film is 1.3 GPa of compression.

Raman spectroscopy has been frequently used till now to estimate the residual stresses for other materials. For a strained lattice, the interatomic potential changes, and the lattice vibration may deviate from that of the unstrained lattice, which has an effect on the Raman active mode of diamond. Residual stress can be evaluated from the shift of the Raman diamond peak with respect to natural diamond value at 1332 cm⁻¹. Raman peak shifts to lower frequencies due to

the presence of tensile stress in diamond films, or to higher ones due to the presence of compressive stress in the films. Ager et al. [Ager93] derived the direct relationship of peak shift of Raman peak with the amount of residual stress. They showed the shift and splitting of the Raman phonon caused by biaxial stress into a singlet and a doublet as a function of crystallographic direction as shown in Table 4.3

Table 4.3 Shift and splitting of the Raman phonon of diamond with biaxial orientation.

Biaxial stress orientation	Singlet shift ($\text{cm}^{-1}/\text{GPa}$)	Doublet shift ($\text{cm}^{-1}/\text{GPa}$)
(100)	-1.64	-2.37
(111)	-0.67	-2.86
(110)	-0.90	-2.25
(112)	-0.90	-2.80
average	-0.93	-2.60

Rats et al. [Rat95] also showed that the use of the average stress gage factor ($-2.60 \text{ cm}^{-1}/\text{GPa}$) for the principal peak (doublet phonon) matched quite well with the experimental results in order to calculate the residual stress as a function of diamond peak shift.

In this study, the same residual stress gas factor ($-0.384 \text{ GPa}/\text{cm}^{-1}$) for the doublet phonon as the one used by Rats was used to calculate the total residual stress as a function of diamond peak shift.

$$\sigma[\text{GPa}] = -0.384\Delta\nu = -0.384(\nu - \nu_0)[\text{cm}^{-1}] \quad (4.6)$$

where ν_0 and ν are the Raman peak position of an unstressed and stressed diamond, respectively.

In order to investigate residual stress of diamond films deposited on laser modified cemented carbide substrates as a function of surface roughness, cemented carbides were modified at 2 J/cm² with different pulses (40, 80, and 120), etched with nitric acid for 30 minutes for removing cobalt on the surface, heat-treated for 5 hrs, then sonicated in diamond colloid, and coated with diamond for 20 hrs as shown in Fig. 4.42. The thickness of diamond films was 15 μm . As the roughness of laser modified cemented carbide substrates was increased, the roughness of diamond film also increased. Figure 4.42(b), (d), (f), and (h) shows the cross-sections of diamond-substrate interfaces.

Figure 4.43 shows the stress changes on the surface of diamond films deposited on laser modified substrate with various roughness using micro-Raman spectroscopy. The stresses were converted from the Raman peak shift of diamond by using equation (4.6). The Raman peak position of unstressed free-standing natural diamond was measure at 1333.67 cm⁻¹ with a full width at half maximum of 3.9 cm⁻¹ in this micron-Raman spectroscopy. The measurement of Raman spectroscopy was performed on peak and valley regions of

diamond films. As shown in Fig. 4.42, as the surface roughness increased, the protrusions of diamond films were larger along with the substrate roughness. Because of the large protrusions of diamond films to the free surface, residual stresses at peak regions (protrusions) on diamond surface were strongly relaxed compared to the ones at valley regions. Ralchenko et al. also observed the same relaxation of stress [Ral95]. Although changes in residual stresses at valley regions on diamond surface were not large, residual surface stress at valley regions decreased slightly with increasing roughness. In Fig. 4.44, full width at half maximum (FWHM) of diamond Raman peak at peak regions of diamond films was large compared to the one (3.9 cm^{-1}) of an unstressed natural diamond and increased with increasing surface roughness due to the superposition of different stress states in the films. On the other hand, changes in FWHM at valley regions of diamond films were small.

Figure 4.45 shows the stress distribution from the diamond-substrate interface to the diamond free surface inside diamond films. Argon ion laser beam having around $4 \mu\text{m}$ spot size was used for the measurement of Raman shift of diamond peaks. The sets of measurements were performed on regions of peak and valley interfaces which were next each other. As shown in Fig. 4.45(a), the interface of diamond film and cemented carbide which was unmodified with laser was almost

flat. The residual stress at diamond-substrate interface expectedly was highest due to large thermal expansion mismatch. As the measurement went up toward the free surface, compressive residual stress gradually decreased. In case of diamond films deposited on laser modified samples having 2.5 μm roughness (Fig. 4.45(b)), difference in residual stress between peak and valley regions at the diamond-cemented carbide interface was surprisingly large. Residual stress at peak region of the interface was even larger than the one in Fig. 4.45(a). It was found that residual stress in the films was normally concentrated on peak interface. As the measurement went up toward the free surface of diamond films, residual stress measured from peak region significantly decreased while residual stress measured from valley region increased, and two stresses became almost the same at the free surface. With an increase in interface roughness to 4.5 μm as shown in Fig. 4.45(c), the residual stress at valley interface was very small, almost near zero value. Compressive residual stress could not affect the valley regions due to geometrical blocking by peak features at diamond-substrate interface. Difference in residual stress between peak and valley regions at a distance of 2 μm from the interface was small compared to the one in Fig. 4.45(b). As the measurements were performed closer to the free surface, compressive residual stresses were more relaxed. In case of a sample having an interface

roughness of 6.3 μm , an interesting behavior was observed. Compressive residual stress measured from the valley regions increased with an increase in distance from interface and became larger than the ones measured from the peak regions to the free surface. The reason is that, as shown in Fig. 4.42, an increase in surface roughness caused the difference in residual stress between peak and valley regions on diamond surface. These surface stresses affected stress distribution inside diamond film just below diamond surface. Higher surface stress in valley region compared to much lower surface stress in peak region caused residual stress measured from valley interface to cross-over the stress measured from peak interface. The residual stress measured at valley interface was almost zero. From the observation of whole stress distribution, the average residual stress decreased with increasing the interface roughness of diamond-substrate.

From the measurement of residual stress of cross-section along with surface residual stress measurement at different interface roughness, the whole stress distributions inside diamond films with different interface roughness are schematically drawn in Fig. 4.46.

Figure 4.47 shows the changes in full width at half maximum (FWHM) of diamond Raman peak for diamond films for different interface roughnesses. Although it was not easy to find any trends in this figure, FWHM at valley interfaces

having lower residual stresses was normally small. However, FWHM measured from the peak interfaces were generally larger due to the broadening of diamond Raman peak caused by complicated stress states. The average FWHM of diamond films decreased with increasing interface roughness.

In order to observe the effect of the surface roughness induced by laser on the adhesion of diamond film, the samples with different roughness were prepared. Samples included cemented carbides nonmodified and modified with laser at 2 J/cm² with 40, 80, and 120 pulses. Samples were etched with Murakami's agent for two minutes and nitric acid for one hour by stirring method, then coated with diamond at a substrate temperature of 960°C with 1% methane in hydrogen. Figure 4.48 shows the surface morphologies of samples for adhesion test. As shown in Fig. 4.48(f), some of the melted/redeposited area at peak regions of cemented carbides which were modified at 2 J/cm² with 120 pulses still remained unetched by etching treatment of two minutes with Murakami's agent. However, except the melted/redeposited area, cemented carbide substrate surfaces were etched and were microscopically roughened (Fig. 4.48(d)-(f)). Figure 4.48(j)-(l) shows the delaminated diamond films indented with a Rockwell C scale brale (spheroconical) diamond indenter at 100 kg using a conventional Rockwell hardness testing system. This method of adhesion testing has been suggested for comparing only films

grown on the same substrate material [Dav89]. The spalled regions after indentation generally have ring shapes. The indentation process induces plasticity of the substrate to lead to the energy transfer to the film, causing delamination. This plasticity can be either radial displacement or a pile up of substrate material around the indenter during indentation. Piling up the substrate effectively causes beam bending of the film as the plastic zone increases [Bah95]. Fig. 4.48(j) shows the pile up of substrate around indentation. When diamond films were indented, delamination diameter decreased with increasing interface roughness as shown in Fig. 4.48(j)-(l). In case of diamond film having a roughness of 3.5 μm , little delamination of diamond films was observed at an indenter load of 100 kg. As previously observed from Fig. 4.45, the reason is that the residual stresses at diamond-substrate interface became smaller with increasing interface roughness and crack propagation paths during indentation may be complicated due to the geometry of diamond film. Figure 4.49 shows the curves of delamination diameter of diamond films as a function of indentation load by indentation adhesion test. The diamond film deposited on cemented carbide unmodified with laser having a low interface roughness showed a considerable delamination even at low indentation load of 60 kg. However, the laser modified cemented carbides still were not delaminated at 60 kg load. Again, it was proved that

increasing interface roughness caused better adhesion of diamond films on cemented carbide.

Etching and Heat Treatment

The control over cobalt binder on the cemented carbide substrate surface is very critical for obtaining adherent diamond films because cobalt is a catalyst for graphitizing diamond, causing weak bonding between diamond film and tungsten carbide. However, depletion of cobalt over a certain range of depth from surface could cause detrimental effects due to loose bonding of tungsten carbide particles.

In this study, the effects of etching agent such as nitric acid for controlling cobalt and Murakami's agent for controlling tungsten carbide, as well as heat treatment on the surface structure and adhesion of diamond films were investigated.

Figure 4.50 shows the surface morphology of cemented carbides when etched with 35% nitric acid by stirring at around 900 rpm. When the substrate was etched for 30 minutes (Fig. 4.50(c)), the grain boundaries of tungsten carbide began to appear due to the removal of cobalt, but the surface of cemented carbide appeared to still contain cobalt. From the cross-sectional view (Fig. 4.50(d)), the depletion of cobalt was observed down to around 20 μm thick from the surface. The

curve of depletion of cobalt as a function of etching time is shown in Fig. 4.52. It is speculated that nitric acid attacked the etched boundaries of tungsten carbide particles more easily and penetrated through locally-etched tungsten carbide boundaries. Figure 4.53 presents the composition changes on the surface of cemented carbides as a function of etching time with nitric acid and heat treatment time using an electron probe microanalyzer (EPMA). After etching for 30 minutes, the cobalt content on the cemented carbide surface significantly decreased. The values of cobalt content in this figure are not absolute values, but relative ones due to the use of different sources such as tungsten and graphite instead of using tungsten carbide in the process of composition calculation in EPMA system. The measured values of cobalt content were larger by a factor of 2.25 than the real composition. After etching for 120 minutes (Fig. 4.50(g)), most of the grain boundaries of tungsten carbide particles on the cemented carbide surface were clearly shown. Although composition change of cobalt over etching time of 30 minutes was small, cobalt content decreased with increase in etching time. The depletion depth of cobalt was around 50 μm (Fig. 4.52). The depletion curve of cobalt as a function of etching time showed a sigmoidal behavior. These kinds of large depletion depth of cobalt may not be desirable for obtaining strong adhesion of diamond films because breaking of cemented

carbide could happen at the boundary of cobalt depletion as shown in Fig. 4.54.

An effective removal method of cobalt only on the shallow surfaces of cemented carbides without hurting bonding among tungsten carbide particles is necessary. Ultrasonic etching method using nitric acid was examined as shown in Fig. 4.51. The removal of cobalt on the cemented carbide surface was more effective than the stirring method. The cross-sectional view (Fig. 4.51 (b), (d), and (f)) showed more homogeneous and effective removal of cobalt within depletion depth than the one used by stirring method. As shown in Fig. 4.52, while the depletion depth of cobalt using ultrasonic method was higher than the one using stirring method up to 15 minutes of etching time, it was lower than the one using stirring method over 15 minutes of etching time. Etching of cobalt within one minute range using ultrasonic method will be useful for removing cobalt without causing much debonding of tungsten carbide particles on the surface.

The effect of heat treatment in pure hydrogen environment on the surface morphology of cemented carbides was also observed (Fig. 4.55). Heat treatments of cemented carbide were performed in hot-filament chemical vapor deposition system at a substrate temperature of 960°C with a filament temperature of 2000°C, a chamber pressure of 20 Torr, and a flow rate 200 sccm of pure hydrogen. After one hour heat

treatment (Fig. 4.55(b)), grain boundaries began to emerge due to the etching of cobalt. Interestingly, some big clusters of cobalt having 1-3 μm size diffused out to the surface of cemented carbide. After 3 hours of heat treatment (Fig. 4.55), the substrate surface showed a lot of small tungsten carbide particles which were suspected to be ground down to around 0.1 μm size during final surface finishing of tool materials. After 5 hours of heat treatment (Fig. 4.55(d)), the number of these small particles significantly decreased. It is not clear why the small particles were disappearing. Tungsten carbides may also be etched away by active atomic hydrogen gases. After 20 hours of heat treatment (Fig. 4.55(f)), the small tungsten carbide particles almost disappeared. The substrate surfaces were cleaned away and had more distinctive tungsten carbide particles compared to other methods such as stirring and ultrasonic methods. Figure 4.56 shows the cobalt distribution on the surface of cemented carbide with different heat treatment time at low magnification. With heat treatment of cemented carbide for one hour (Fig. 4.56(a)), a lot of cobalt clusters ($\sim 8 \times 10^5 / \text{cm}^2$) were observed. Backscattered electron image of Fig. 4.56(a) shows dispersion of cobalt more clearly (black spot in Fig. 4.56(b)). With heat treatment for three hours (Fig. 4.56(c)), the number of cobalt clusters decreased down to around $1 \times 10^5 / \text{cm}^2$. After 5 hours of heat treatment (Fig.

4.56(d)), cobalt clusters completely disappeared. Figure 4.57 shows the depletion depth of cobalt as a function of heat treatment time. Depletion depth of cobalt was quite small as compared to other methods such as stirring and ultrasonication. Although long heat treatment was required to etch away cobalt, it was very effective for perfectly removing cobalt on the surface without damaging the substrate to large depth. Heat treatment might also cause tungsten carbide particles to bond together on the surface as shown in Fig. 4.55(f). From cross-sectional view of etched cemented carbide in Fig. 4.58, there were not many changes in depletion depth between 5 hrs and 20 hrs heat treatment. As shown in Fig. 4.53, heat treatment of as-received cemented carbides over 5 hrs caused significant amount of decrease in cobalt. Heat treatment for cemented carbides etched with nitric acid for 120 minutes without heat treatment for 120 minutes was performed and result obtained is shown in Fig. 4.59. The surface of cemented carbide etched with nitric acid is shown in Fig. 4.50(g). After heat treatment of 5 hrs (Fig. 4.59(a)), small tungsten carbide particles were observed on the surface, similar to the ones in the unetched cemented carbide(Fig. 4.51(d)). With an increase in heat treatment time, the small tungsten carbide particles appeared to be bonded to the larger tungsten carbides. Fig. 4.53 shows that there was little change in cobalt composition with different

heat treatment times for cemented carbides etched with nitric acid for 120 minutes because the cobalt on the substrate was almost removed by nitric acid.

In order to observe the effect of the etching treatment and heat treatment on the adhesion of diamond films, diamond films were grown on as-received cemented carbides. Before diamond coating, the cemented carbides were etched with nitric acid for 0, 15, and 60 minutes, then ultrasonically scratched and seeded in diamond colloids, and heat-treated for 10-30 hrs. Other samples with high density of diamond seeds before diamond deposition were prepared for comparison of adhesion. Indentation adhesion test was performed on those diamond films. The main reason for seeding before heat treatment is to make diamond seeds stick more to cemented carbide substrates by partial dissolution of diamond seeds to the substrate during heat treatment. Diamond films were found to be easily detached if diamond particles were seeded after heat treatment.

Figure 4.60 shows the surface morphology and indentation of diamond films deposited for 10 hrs on cemented carbides which were etched with nitric acid for 15 minutes, then seeded and heat-treated for 10-30 hrs. Just after normal ultrasonic scratch and seeding in diamond colloids, the density of diamond seeds of around $0.1 \mu\text{m}$ size was approximately $5 \times 10^8 / \text{cm}^2$. High density seeding of diamond was controlled by

ultrasonication time and a density of around $8 \times 10^8 /cm^2$ was obtained. It was difficult to measure diamond seed density on the heat treated surface because a lot of etched small tungsten carbide particles as shown in Fig. 4.55(e) were also mixed together. With increasing heat treatment time from 10 to 30 hrs (Fig. 4.60(a), (c) and (e)), the diamond grains grew bigger with some more voids around diamond grain boundaries. This may be due to more etching of diamond seeds during heat treatment, causing less nucleation density for diamond growth. Indentation adhesion test showed better adhesion characteristics with longer heat treatment. There might be several reasons for better adhesion with longer heat treatment: (i) more perfect removal of cobalt on the cemented carbide surface, resulting in stronger bonding, (ii) stronger adhesion of diamond nuclei (seeds) before diamond deposition due to dissolution of diamond seeds to tungsten carbide matrix, and (iii) stress relaxation of diamond films due to more voids around grain boundaries, resulting from less nucleation density. The surface roughness values of diamond films on cemented carbide etched for 15 minutes prior to diamond coating were not changed much with increasing heat treatment time as shown in Fig. 4.63. However, the surface roughness values of diamond films were significantly larger than the ones grown with high density seeds. The grain size of diamond films with high density seeds was approximately 5

μm, resulting in smaller roughness.

Figure 4.61 shows the surface morphology and indentation of diamond films on cemented carbides which were etched with nitric acid for various time, then heat-treated for 30 hrs. As the etching time with nitric acid before diamond deposition was increased, the surface roughness of diamond films also increased with more voids around grain boundary of diamond films. It is not clear why the longer etching time with a heat treatment of 30 hrs caused less nucleation density while growing diamond films. The adhesion of diamond films decreased with increasing etching time. The reason for poor adhesion with increasing etching time is that cracking occurred at the interface between the etched and unetched regions of cobalt in the substrate instead of breaking at diamond-substrate interface as shown Fig. 4.61(f) and 4.54. Shown in Fig. 4.62 are the results of Rockwell indentation adhesion test for the substrates with etching and heat treatments. Comparing the slopes of delamination diameter-load curve together, diamond films on cemented carbide without nitric acid etching and with longer heat treatment had stronger adhesion. Perfect removal of cobalt only within shallow depth, strong bonding of diamond nuclei to the substrate, and stress relaxation through some voids may affect the adhesion of diamond films. Overetching of substrate with nitric acid was not found to be desirable for adhesion due to

formation of weak substrate surface. Diamond films deposited on the substrates having diamond seeds of high density were mostly delaminated even at a load of 60 kg. A diamond film on cemented carbide which was heat-treated for 10 hours was also delaminated at a load of 60 kg. Heat treatment below 10 hours for cemented carbides having an interface roughness of one micron may not be enough for removing cobalt to certain depth and for preventing diffusion of cobalt out to the surface during diamond deposition. Longer heat treatment irrespective of pre-etching time of cemented carbides provides good adhesion of diamond films. Increasing etching time caused steeper slopes of delamination diameter-load curve because of weaker adhesion. Figure 4.63 showed the surface roughness of diamond films with etching and heat treatment. Again, longer etching time with nitric acid resulted in higher surface roughness of diamond films.

Murakami's agent ($K_3Fe(CN)_6$: NaOH : $H_2O = 1 : 1 : 10$ by weight) for controlling tungsten carbide matrix was used to observe the effect on the adhesion of diamond films. Figure 4.64 shows the surface morphology of cemented carbides modified at 2 J/cm^2 with 120 pulses as a function of etching time with Murakami's agent by stirring method. Figure 4.65 presents the XRD of laser modified cemented carbides as a function of etching time with Murakami's agent. Until two minutes of etching, low carbon tungsten carbides such as WC_{1-x}

and W_2C phases remained on the modified cemented carbide surface. After etching for five minutes, low carbon tungsten carbide phases almost disappeared and only WC phase remained.

Indentation adhesion test was performed on diamond films on cemented carbides having various treatments. Surface treatment procedures of cemented carbides are listed in Table 4.4. Seeding of diamond was performed by ultrasonication just before heat treatment. After various surface treatments of cemented carbides, diamond films were deposited for 20 hours. Surface morphology changes for each step of surface treatments and adhesion indentation are shown in Fig. 4.66, 4.70, and 4.71.

Table 4.4 Surface treatment conditions of cemented carbides.

Surface Treatment	M: Surface modification at 2 J/cm ² with 120 pulses N: Nitric acid etching for 60 sec by ultrasonication. Mu(x): Murakami etching for x sec by ultrasonication. N2: Nitric acid etching for 15 sec by ultrasonication. H: Heat treatment for 10 hrs.
Cemented Carbide Samples for Diamond Deposition	<ol style="list-style-type: none"> 1. MNMu(15)N2H : Fig. 4.66(a), (d), (g), and (j) 2. MNMu(30)N2H : Fig. 4.66(b), (e), (h), and (k) 3. MNMu(90)N2H : Fig. 4.66(c), (f), (i), and (l) 4. NH : Fig. 4.70(a), (d), (g), and (j) 5. NMu(30)N2H : Fig. 4.70(b), (e), (h), and (k) 6. NMu(90)N2H : Fig. 4.70(c), (f), (i), and (l) 7. NMu(90)N2 : Fig. 4.71(a), (b), and (c)

In Fig. 4.66(a), Murakami etching for 15 seconds by ultrasonication did not show a significant effect on the surface morphology of a modified cemented carbide. As shown in Fig. 4.66(b), etching for 30 seconds caused the removal of 60% of the melted surface of a modified cemented carbide except the melt/redeposited peak regions. The etched areas showed tungsten carbide particles. The etching of a cemented carbide for 90 second showed removal of the entire melted surface of laser modified substrate (Fig. 4.66(c)). Figure 4.66(d)-(f) shows the heat treated surface of the substrate. If we closely look at the heat treated surface (Fig. 4.67), a needle-like tungsten carbide (WC) phase was grown from nano-size low-carbon tungsten carbide phases (WC_{1-x} and W_2C). Backscattered electron image of cross-section of diamond-cemented carbide interface (Fig. 4.67(c)) also showed needle-like phases at the interface. XRD results shown in Fig. 4.68 proved that low carbon tungsten carbide phases transformed to WC phase after a heat treatment of 5 hrs. After a heat treatment of 10 hrs, diamond films were grown as seen from Fig. 4.66(g)-(i). As the etching time with Murakami's agent increased, the surface roughness of diamond films also increased to around 4 micron (Fig 4.73). Although the reason is not clear, it is speculated that microscopic irregularities of cemented carbides induced by etching probably led to outgrowth of diamond grains. Indentation

adhesion tests (Fig. 4.72) showed no delamination of diamond films deposited on cemented carbide etched for 90 seconds, with Murakami's agent, as shown in Fig. 4.66(1). With an increase in Murakami etching time to 90 seconds, adhesion of diamond films increased. The cross-section of this diamond film on the substrate which was etched for 90 seconds with Murakami agent (Fig. 4.66(1)) is shown in Fig. 4.69. Periodic wavy interface of diamond-cemented carbide was observed with a good bonding to each other. The effects of Murakami's agent on the diamond films grown on cemented carbides which were not modified with laser are shown in Fig. 4.70 and 4.71. As shown in Fig. 4.70(a)-(c), the surface morphology of cemented carbides etched with Murakami's agent showed higher roughness as seen in Fig. 4.73. Grain size of diamond films deposited on cemented carbides which were etched with Murakami's agent was a little bit larger than the one without Murakami etching (Fig. 4.70(g)-(i)). There were no voids around grain boundary in diamond films because of heat treatment for a short time (10 hrs) as compared to the ones with heat treatment for 20-30 hrs (Fig. 4.60). However, the grain size of diamond films without heat treatment was around 10 μm with a roughness of 1.6 μm as compared the ones with heat treatment (15-20 μm grains and 4 μm roughness) (Fig. 4.71 and 4.73). From Fig. 4.73, the grain size of all diamond films having undergone heat treatment increased to around 4 μm . A diamond film with

no heat treatment did not show much changes in grain size (Fig. 4.73). From observation of indentation adhesion test in Fig 4.70(j)-(l) and Fig. 4.72, it can be seen that diamond films with increasing etching time from 0 sec. to 90 sec. with Murakami's agent gave higher adhesion and heat treatment also provided better adhesion from a comparison of Fig. 4.70(l) and 4.71(c).

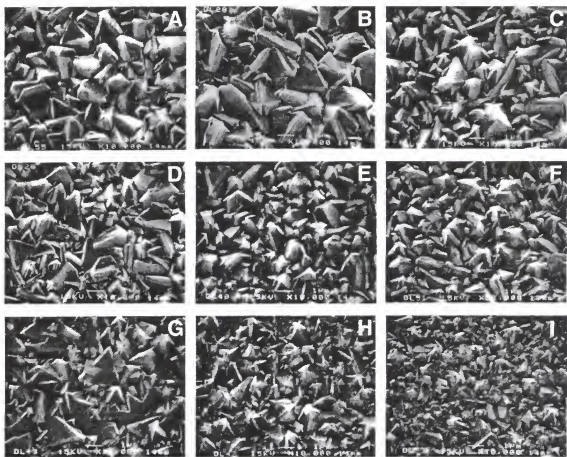


Figure 4.1 Surface morphology changes of diamond films as a function of chamber pressure(P : (a-c) 20 Torr; (d-f) 40 Torr; (g-i) 80 Torr) and gas flow rate (R_g : (a)(d)(g) 100 sccm; (b)(e)(h) 300 sccm; (c)(f)(i) 500 sccm). Other conditions: methane concentration(C)=1%, filament temperature(T_f)=2035°C, substrate temperature(T_s)=925°C, filament-substrate (F-S) distance=1 cm.

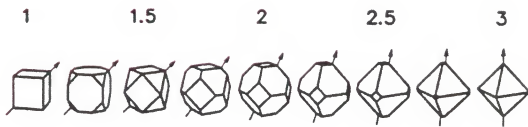


Figure 4.2 Diamond crystal shapes for different values of the growth parameter (α). The arrows denote the largest diameter, i.e. the direction of fastest growth [Wil93].

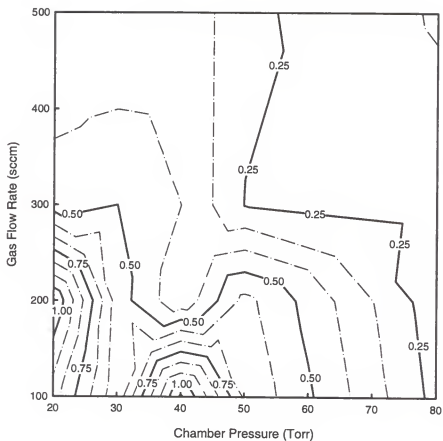


Figure 4.3 Contour plot of Raman peak intensity ratio of diamond to graphite (I_d/I_g) as a function of with gas flow rate and chamber pressure.

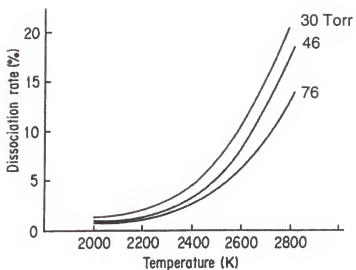


Figure 4.4 Calculated thermal dissociation rate of molecular hydrogen as a function of temperature and pressure [Set89].

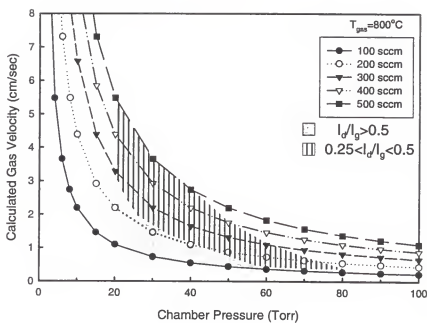


Figure 4.5 Calculated gas velocity with chamber pressure and gas flow rate (chamber diameter: 17cm).

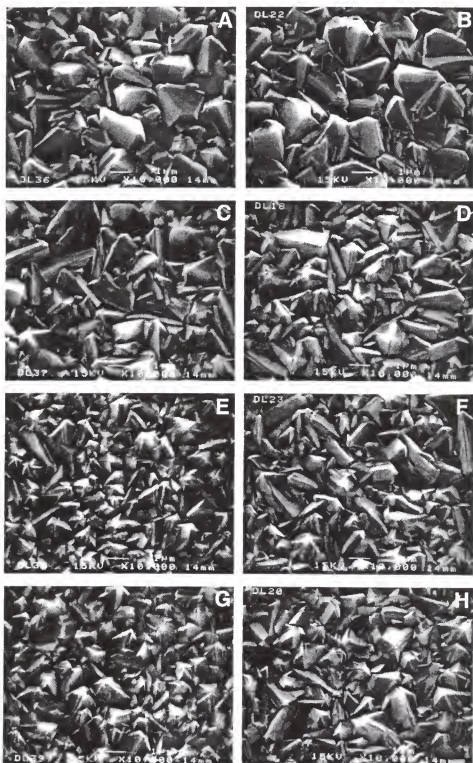


Figure 4.6 SEM images of diamond films as a function of chamber pressure (P : (a-b) 20 Torr; (c-d) 30 Torr; (e-f) 40 Torr; (g-h) 50 Torr) and substrate temperature (T_s ; (a) (c) (e) (g) 925°C; (b) (d) (f) (h) 1000°C) ($R_g=200$ sccm and F-S distance=1 cm, methane concentration (C)=1%).

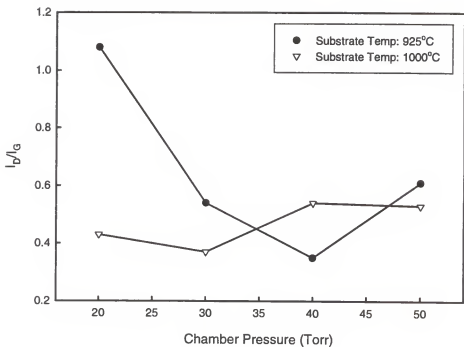


Figure 4.7 Dependence of Raman peak intensity ratio of diamond to graphite(I_d/I_g) on chamber pressure and substrate temperature.

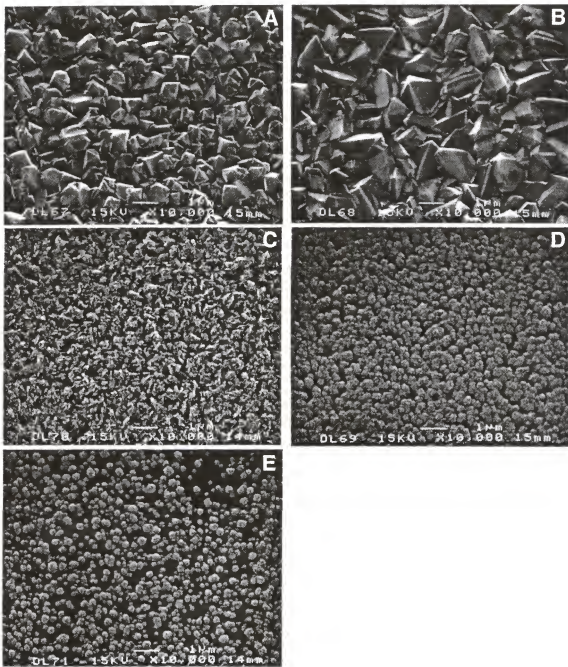


Figure 4.8 SEM images of diamond films with methane concentration of (a) 0.5%, (b) 1%, (c) 2%, (d) 3%, and (e) 5% ($P=20$ Torr, $R_g=100$ sccm, $T_s=960^\circ\text{C}$, $T_f=2035^\circ\text{C}$, and F-S distance=1 cm).

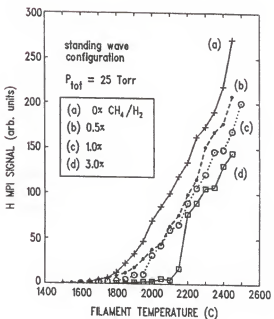


Figure 4.9 Dependence of the hydrogen atom REMPI (resonance-enhanced multiphoton ionization) intensity on filament temperature in HFCVD chamber operated at 25 Torr [Cel89].

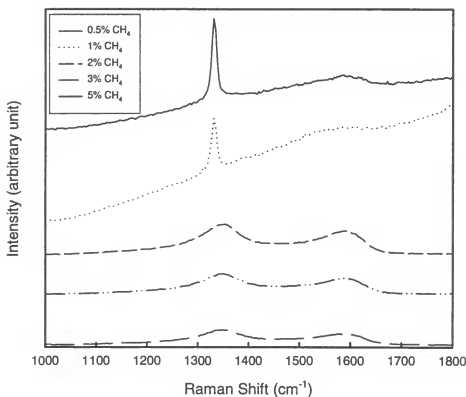


Figure 4.10 Raman spectra of diamond films with methane concentration.

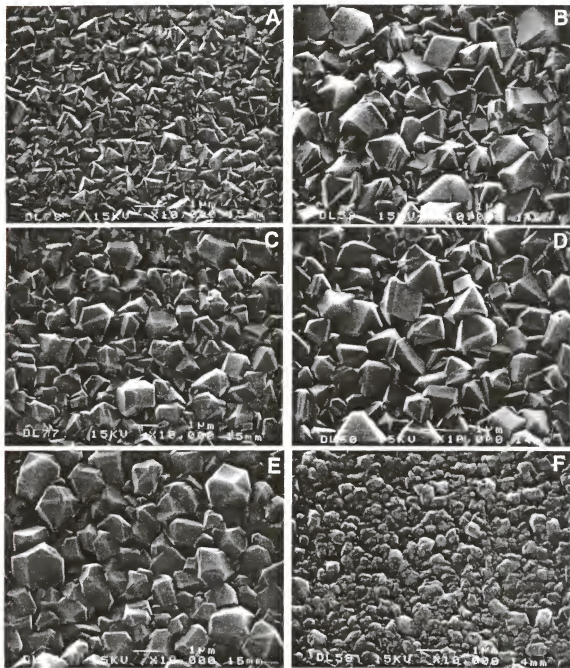


Figure 4.11 SEM images of diamond films with filament temperature: (a) 1820°C, (c) 2100°C, and (e) 2270°C, $T_s=925^\circ\text{C}$, F-S distance=1.5 cm; (b) 2050°C, (d) 2170°C, and (f) 2300°C, $T_s=1030^\circ\text{C}$, F-S distance=1.0 cm. ($P=20$ Torr, $R_g=100$ sccm, and $C=1\%$)

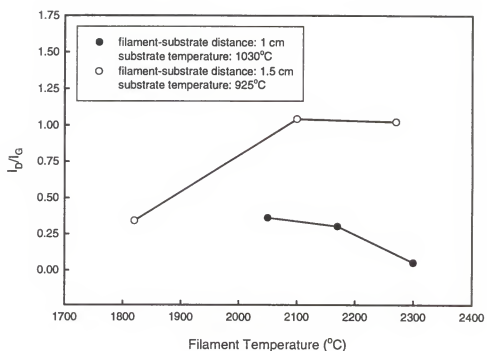


Figure 4.12 Dependence of Raman peak intensity ratio of diamond to graphite (I_d/I_g) on filament temperature.

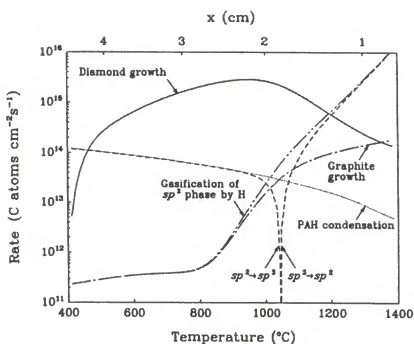


Figure 4.13 Calculated comparison of the rates of carbon depositing and removing reactions for HFCVD chamber operated at 20 Torr, 0.3% CH_4 [Fre91].

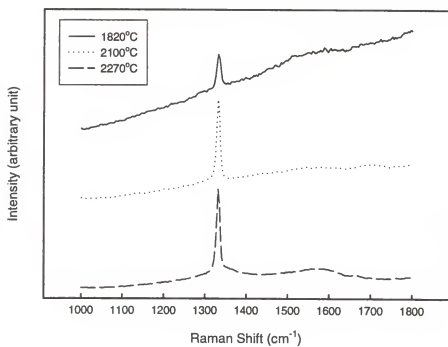


Figure 4.14 Raman spectra of diamond films for different filament temperatures ($T_s = 925^\circ\text{C}$, F-S distance=1.5 cm).

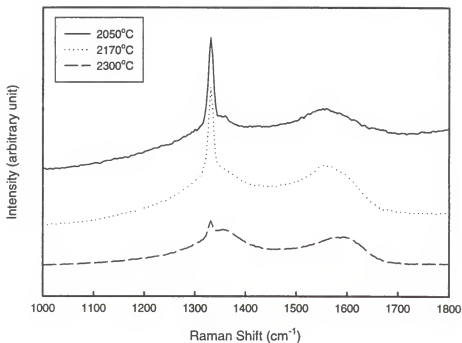


Figure 4.15 Raman spectra of diamond films for different filament temperatures ($T_s=1030^\circ\text{C}$, F-S distance=1 cm).

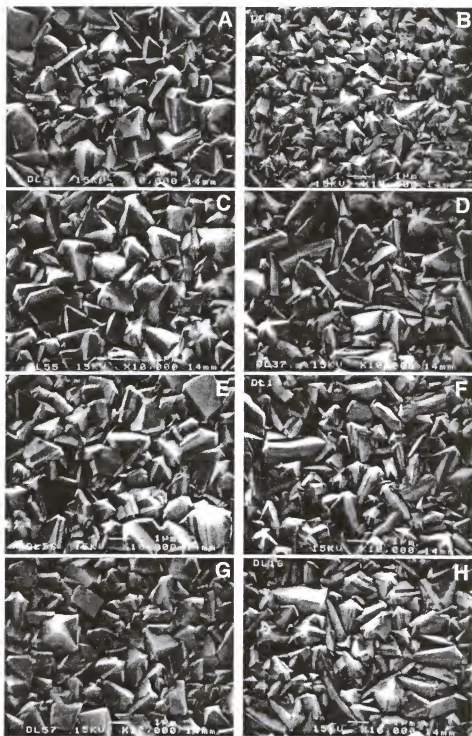


Figure 4.16 SEM images of diamond films with substrate temperature; $P=20$ Torr, $R_g=100$ sccm, F-S distance=1 cm, (a) 900°C, (c) 925°C, (e) 960°C, and (g) 1000°C; $P=30$ Torr, $R_g=200$ sccm, F-S distance=1 cm, (b) 900°C, (d) 925°C, (f) 960°C, and (h) 1000°C. ($T_f = 2035^\circ\text{C}$ and $C=1\%$)

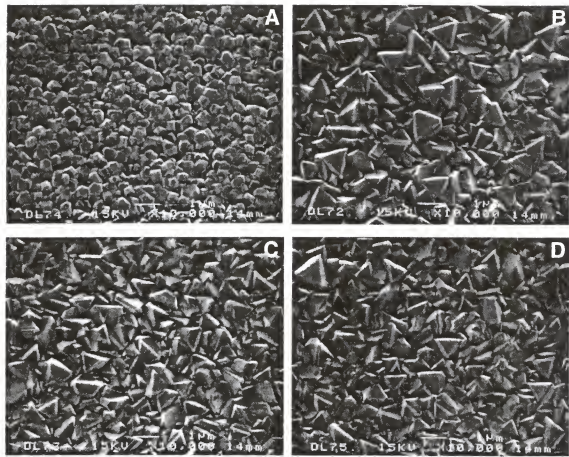


Figure 4.17 SEM images of diamond films for different substrate temperatures (a) 700°C ($T_f=1800^\circ\text{C}$), (b) 800°C, (c) 900°C, and (d) 1000°C ($P=20$ Torr, $R_g=100$ sccm, $T_f=1950^\circ\text{C}$, F-S distance=1.5 cm, and $C=1\%$)

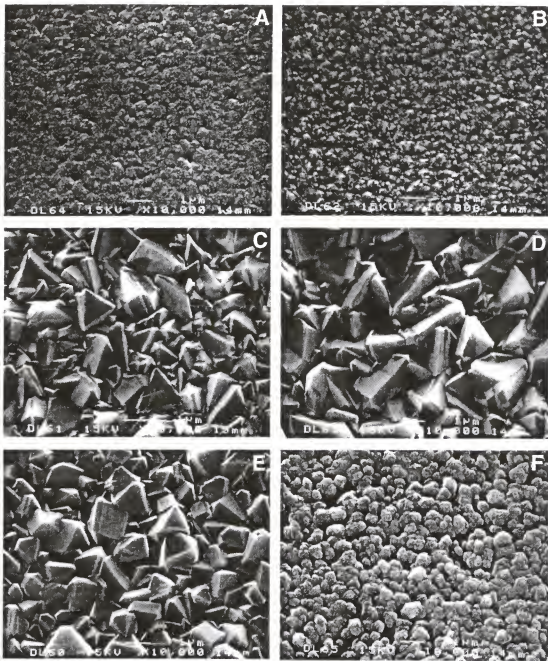


Figure 4.18 SEM images of diamond films for different filament and substrate temperatures (a) $T_s=700^\circ\text{C}$ ($T_f=1700^\circ\text{C}$), (b) $T_s=800^\circ\text{C}$ ($T_f=1900^\circ\text{C}$), (c) $T_s=900^\circ\text{C}$ ($T_f=2010^\circ\text{C}$), (d) $T_s=960^\circ\text{C}$ ($T_f=2080^\circ\text{C}$), (e) $T_s=1000^\circ\text{C}$ ($T_f=2170^\circ\text{C}$) and (f) $T_s=1030^\circ\text{C}$ ($T_f=2350^\circ\text{C}$). ($P=20$ Torr, $R_g=100$ sccm, $T_f=1950^\circ\text{C}$, F-S distance=1.5 cm, and C=1%)

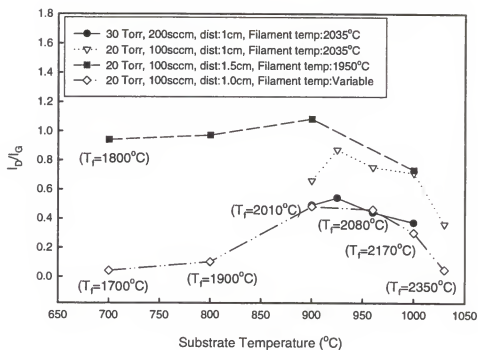


Figure 4.19 Dependence of Raman peak intensity ratio of diamond to graphite(I_d/I_g) on substrate temperature.

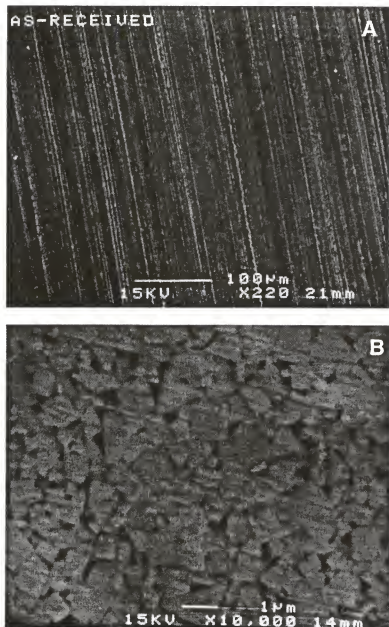


Figure 4.20 SEM images of cemented carbide (WC-6%Co).
(a) as-received and (b) polished and etched surface.

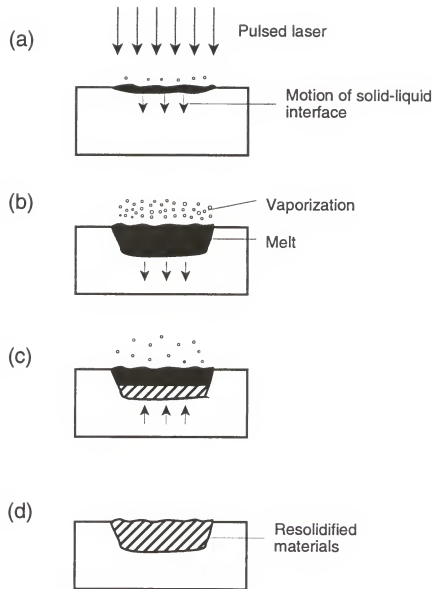


Figure 4.21 Schematic diagram of the basic thermal cycle induced by a laser pulse. (a) Absorption of laser and melting, (b) Propagation of melt front, (c) Recession of melt front and start of solidification, and (d) Completion of solidification. The next laser pulse will interact with some or all of the resolidified material [Fol94].

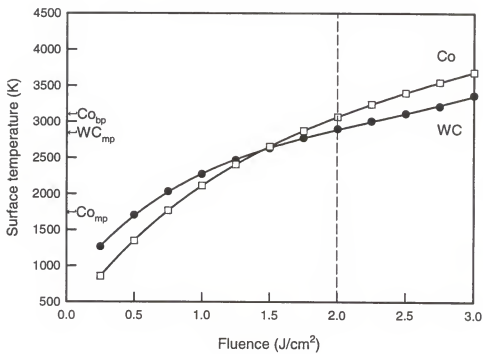


Figure 4.22 Calculated surface temperature as a function of laser fluence using SLIM (Simulation of Laser Interactions with Materials) program.

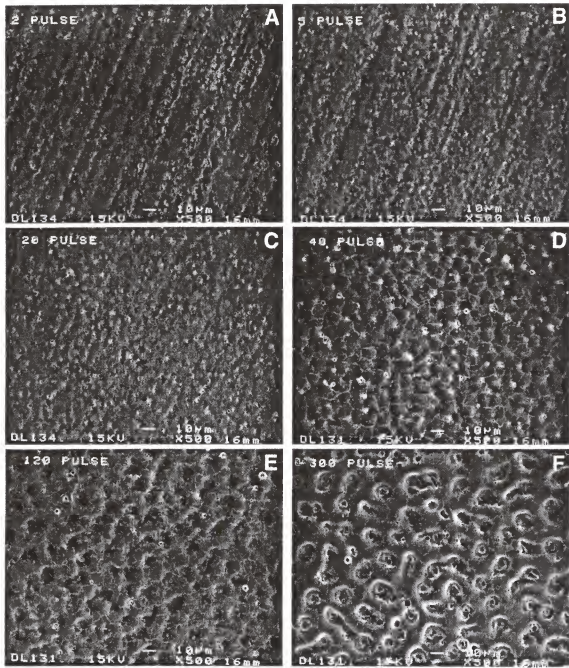


Figure 4.23 Surface morphology changes of cemented carbide surfaces with (a) 2, (b) 5, (c) 20, (d) 40, (e) 120, (f) 300, (g) 450, (h) 600, (i) 900, (j) 1200, (k) 1500, and (l) 2700 pulses at 2 J/cm^2 in static mode (no moving samples).

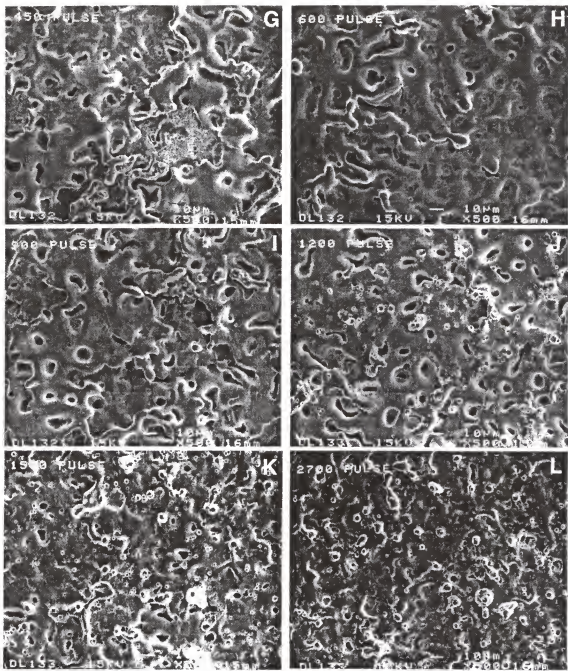


Figure 4.23 --continued.

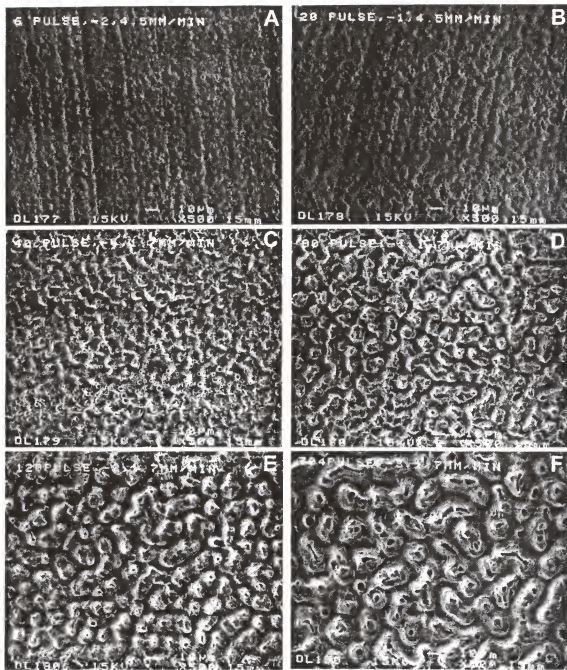


Figure 4.24 Surface morphology changes of cemented carbide surfaces with (a) 6, (b) 20, (c) 40, (d) 80, (e) 120, (f) 300, (g) 400, (h) 675, (i) 1015, (j) 1350, (k) 2050, and (l) 3040 pulses at 2 J/cm^2 in dynamic mode (moving of samples during scanning).

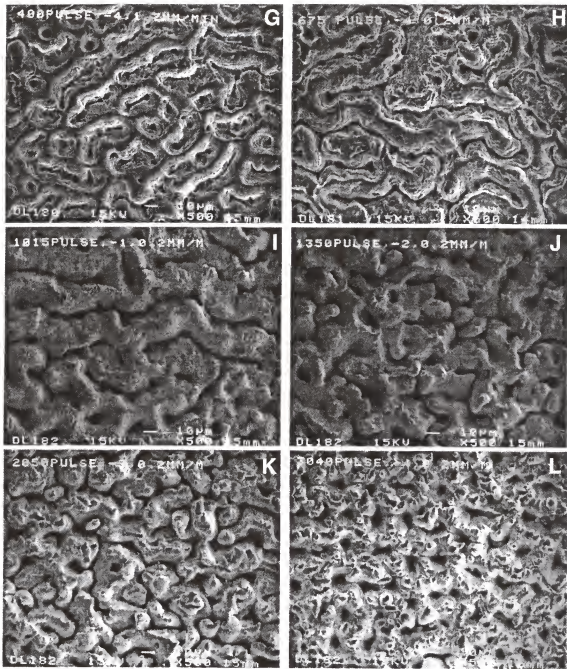


Figure 4.24 --continued

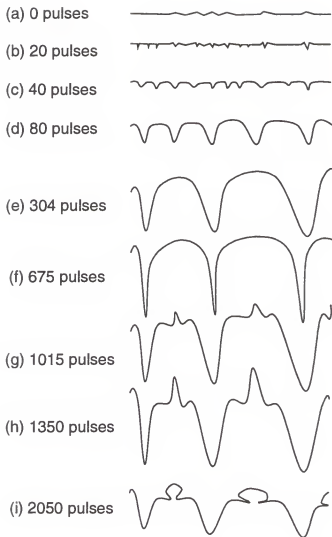


Figure 4.25 Schematic drawing of the evolution of surface features with increasing the number of pulses at dynamic mode, (a) as-received, (b) some pits formed, (c) development to peaks and valleys having 10 μm periodicity, (d) growth of peaks and valleys having 20 μm periodicity, (e) increase in periodicity to 30 μm , (f) valley became deeper and narrower, (g) evaporation on peak regions, (h) sharper peaks, and (i) melting of sharp peaks.

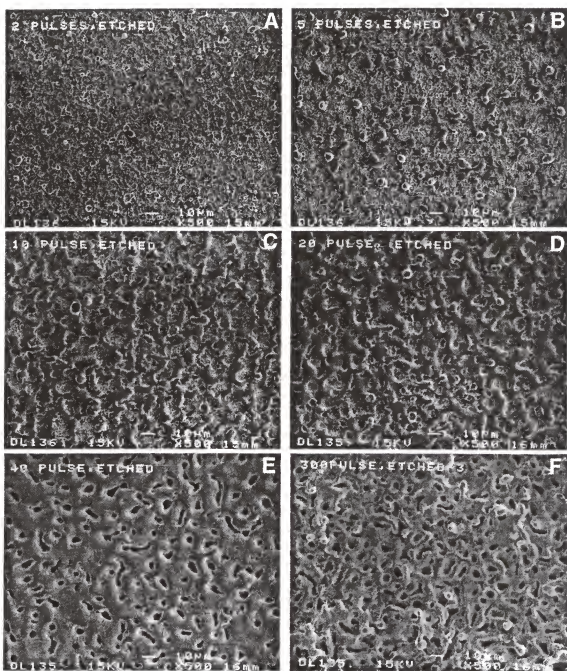


Figure 4.26 Surface morphology changes of etched cemented carbide surfaces with (a) 2, (b) 5, (c) 10, (d) 20, (e) 40, and (f) 300 pulses at 2 J/cm^2 in static mode (no moving samples).

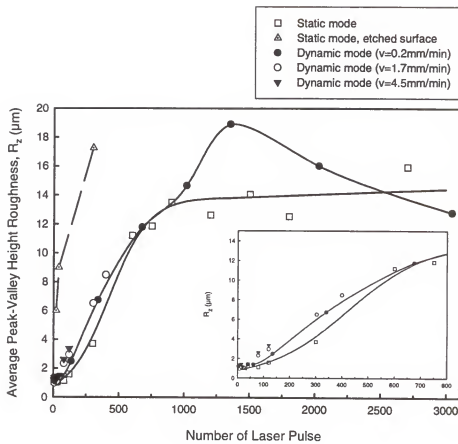


Figure 4.27 Roughness (R_z) changes of cemented carbides as a function of the number of pulses at 2 J/cm^2 .

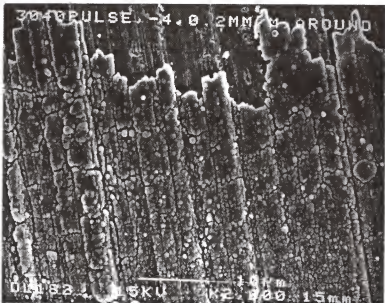


Figure 4.28 Deposits around laser-modified areas of cemented carbides irradiated with laser at 2 J/cm^2 with 3040 pulses (dynamic mode).

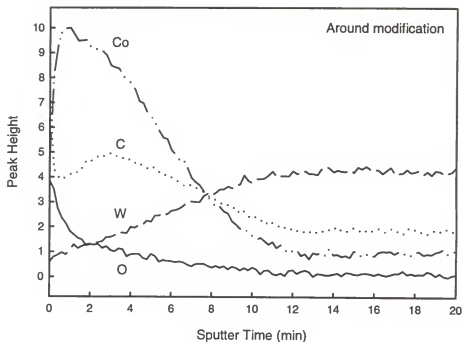


Figure 4.29 Depth profiles of deposits around laser-modified cemented carbides using Auger electron spectroscopy.

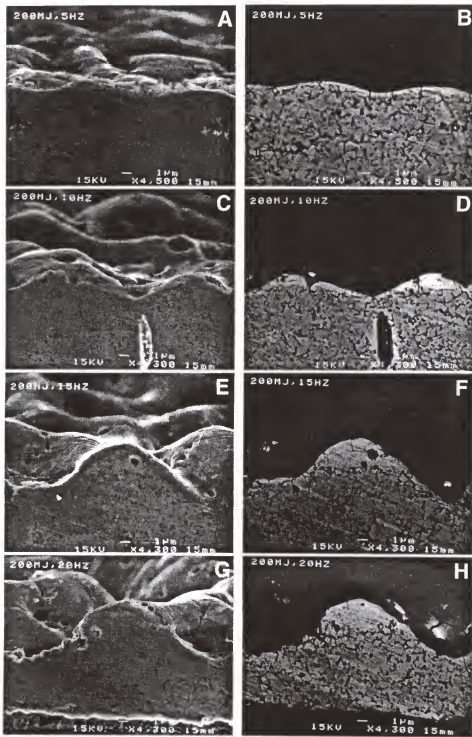


Figure 4.30 Cross-section of LIMS (laser-induced micro-rough structure) with (a) 40, (c) 80, (e) 120, and (g) 160 pulses at 2 J/cm^2 . (b), (d), (f), and (h) are back scattered electron images of (a), (c), (e), and (g), respectively.

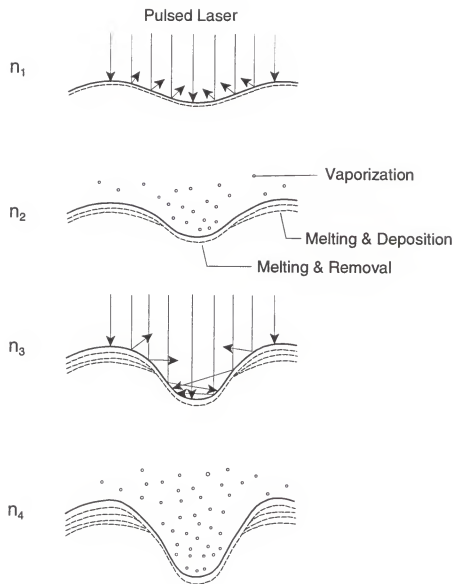


Figure 4.31 Schematic drawing of evolution of periodic micro-rough structure with increasing the number of laser pulses ($n_1 < n_2 < n_3 < n_4$) (The dotted line indicates the phase-transformed areas).

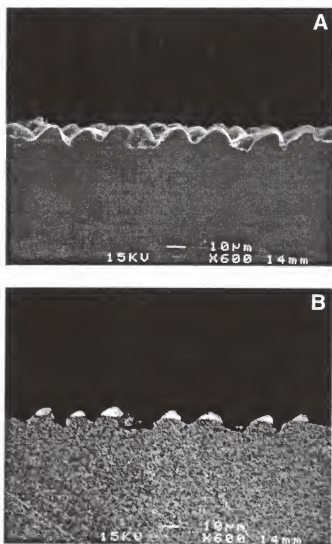


Figure 4.32 Cross-section of LIMS: (a) secondary electron image(SEI) and (b) backscattered electron image(BEI).

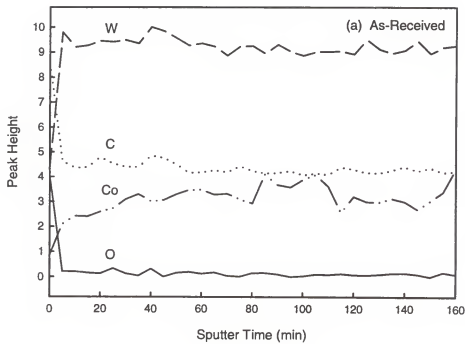


Figure 4.33 Depth profile of cemented carbides with and without laser modification using Auger electron spectroscopy: (a) as-received, (b) from peak region modified at 2 J/cm^2 with 120 pulses, (c) from valley region modified at 2 J/cm^2 with 120 pulses, (d) more details about peak region modified at 2 J/cm^2 with 120 pulses, and (e) from peak region modified 2 J/cm^2 with 40 pulses.

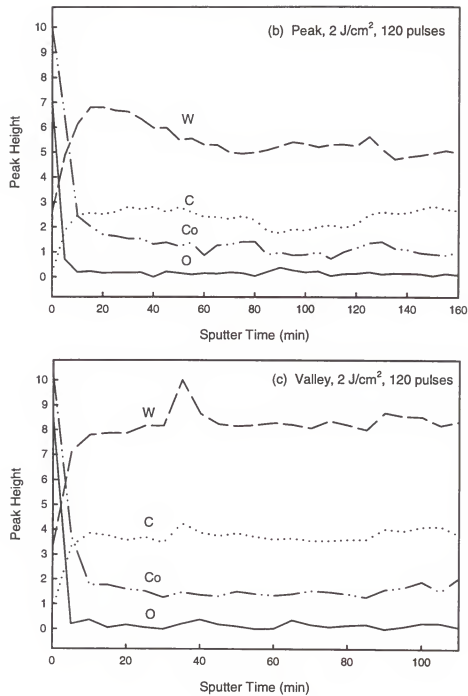


Figure 4.33 --continued

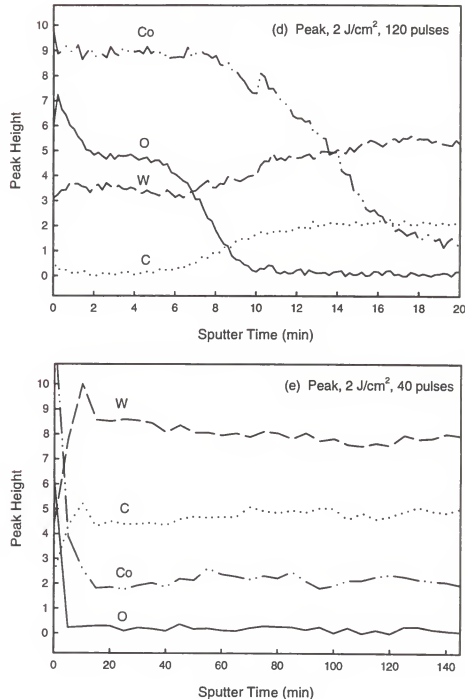


Figure 4.33 --continued

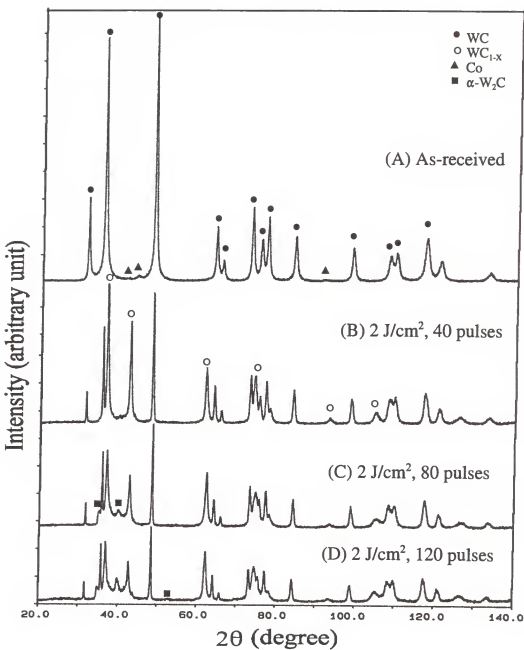


Figure 4.34 X-ray diffraction of laser modified cemented carbide (WC-6Co) as a function of laser pulse.

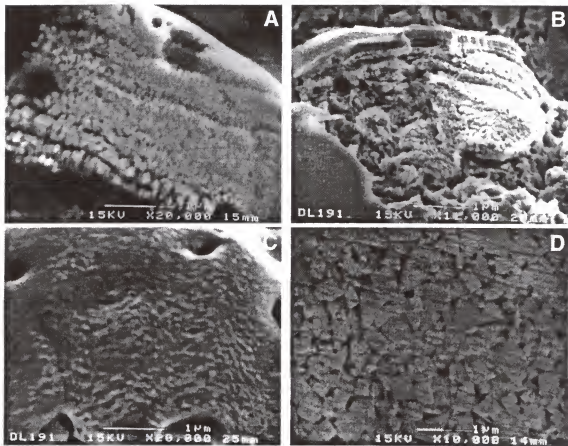


Figure 4.35 SEM images of surface modified region: (a), (b), and (c) melt-zone of LIMS; (d) unmodified cemented carbide matrix.

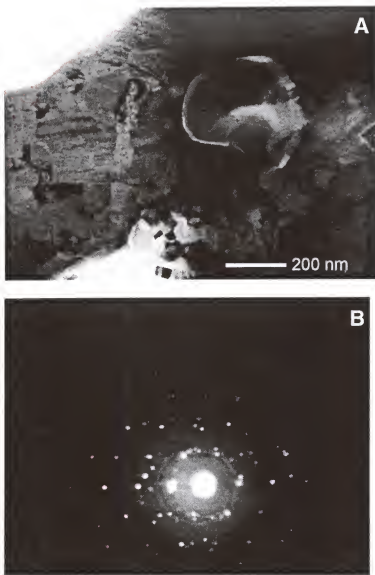


Figure 4.36 Transmission electron micrograph of melt-zone of LIMS:(a) bright field image and (b) diffraction pattern.

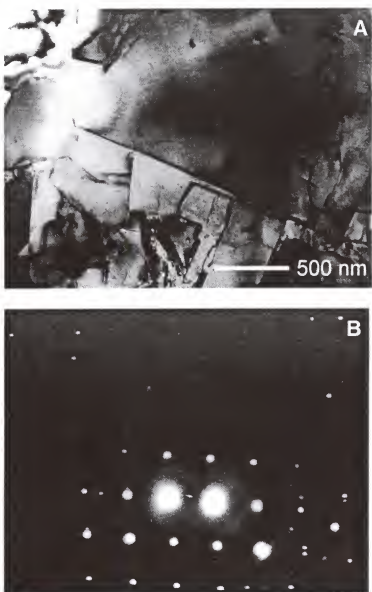


Figure 4.37 Transmission electron micrograph of as-received cemented carbide substrate: (a) bright field image and (b) diffraction pattern.

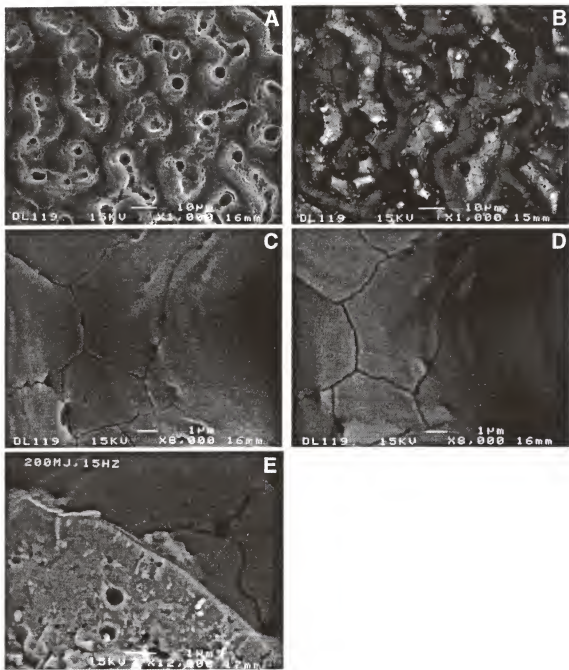


Figure 4.38 Surface morphology of LIMS: (a)SEI, (b) BEI of (a), (c) magnified view, (d) BEI of (c), and (e)cross-section.

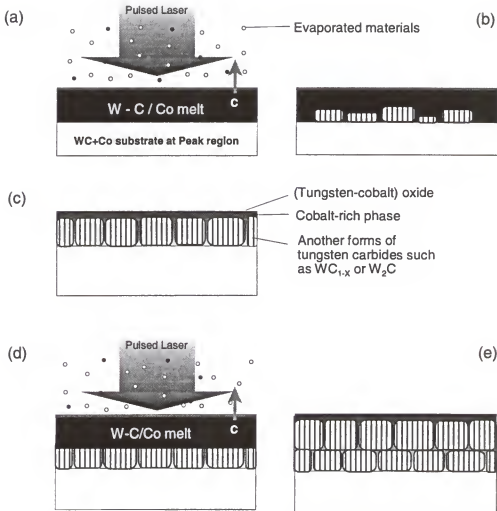


Figure 4.39 Schematic drawing of the formation of peak regions of surface modified cemented carbides during laser irradiation. (a) A pulsed laser melts substrate, evaporated materials coming from valley regions are dissolved, and carbon is more evaporated (b) Another forms of tungsten carbides (WC_{1-x} or W_2C) having less carbon content nucleate and grow in the melt, (c) Cobalt is segregated to surface when solidified, (d) Another pulsed laser melts substrate again within melt-depth region and evaporated materials are dissolved again, and (e) Multiple layers of tungsten carbide phases having less carbon content.

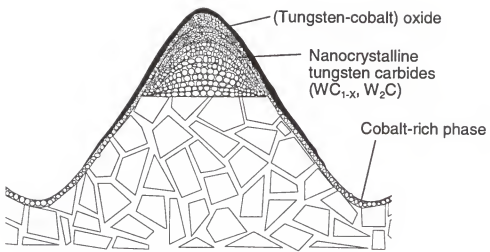


Figure 4.40 Schematic drawing of laser-induced micro-rough structure of cemented carbides.

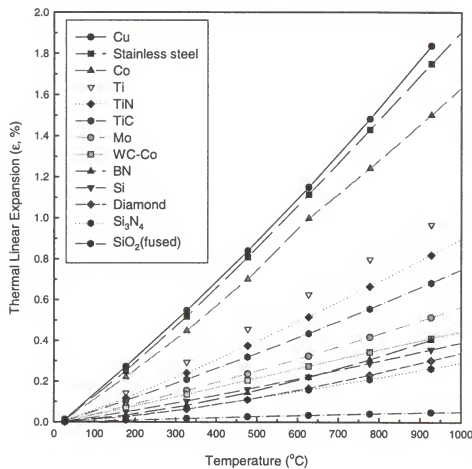


Figure 4.41 Thermal expansion (ϵ) as a function of temperature for diamond and other substrate materials. zero expansion correspond to $T=20^{\circ}\text{C}$.

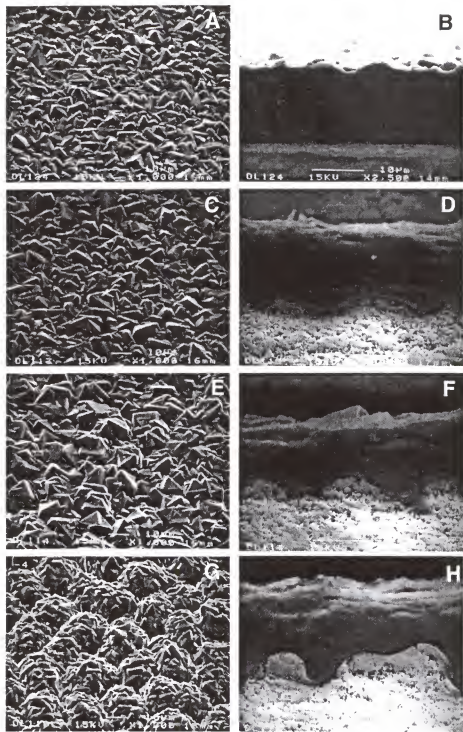


Figure 4.42 SEM images of diamond films deposited on cemented carbide (a) with no modification, (c) modified at 2 J/cm^2 with 40 pulses, (e) modified at 2 J/cm^2 with 80 pulses, (g) modified at 2 J/cm^2 with 120 pulses. (b), (d), (f), and (h) are the cross-sections of (a), (c), (e), and (g) respectively.

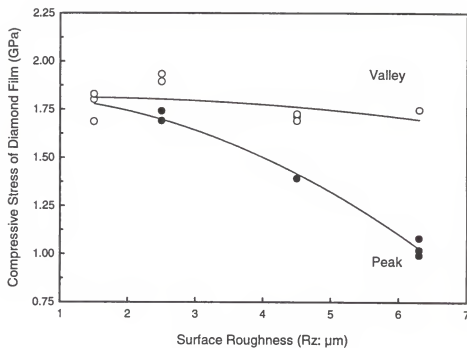


Figure 4.43 Stress changes on the top surface of diamond film deposited on laser modified substrates as a function of roughness using micro-Raman spectroscopy.

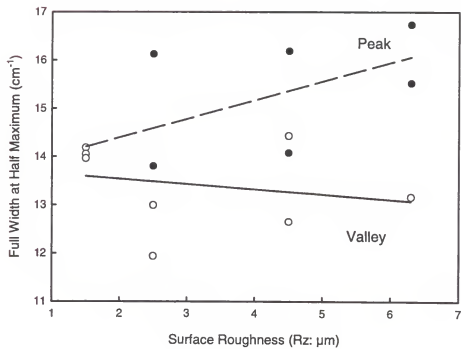


Figure 4.44 Full width at half maximum (FWHM) of diamond Raman peak measured on the diamond film surface as a function of roughness.

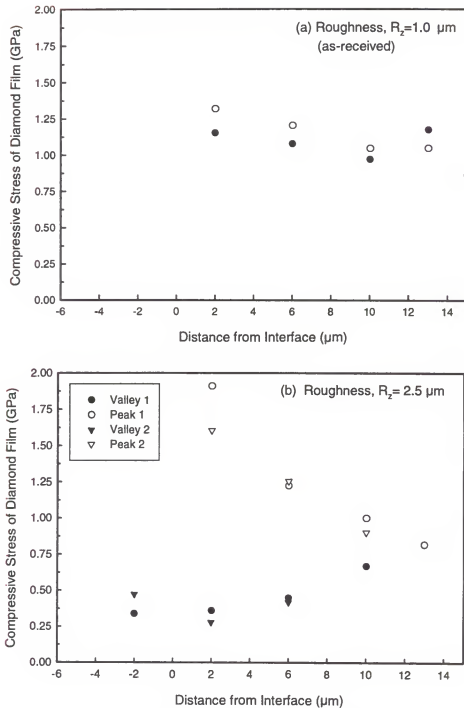


Figure 4.45 Stress changes from the diamond-cemented carbide interface to the diamond film surface using micro-Raman spectroscopy: (a) interface roughness, $R_z=1.0 \mu\text{m}$ (as-received), (b) interface roughness, $R_z=2.5 \mu\text{m}$, (c) interface roughness, $R_z=4.5 \mu\text{m}$, and (d) interface roughness, $R_z=6.3 \mu\text{m}$.

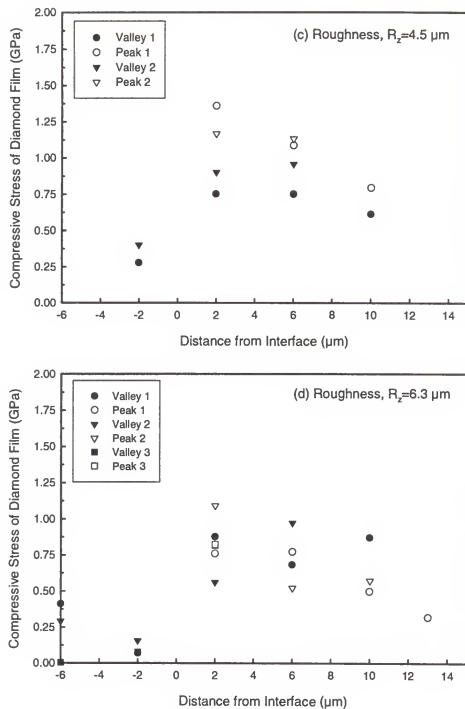


Figure 4.45 --continued

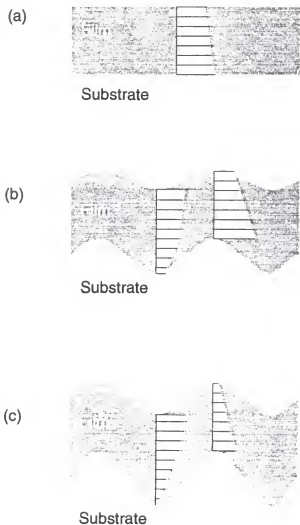


Figure 4.46 Schematic diagram of compressive residual stress distribution inside diamond films from (a) planar interface and laser modified interface having roughness (b) R_1 and (c) R_2 ($R_1 < R_2$).

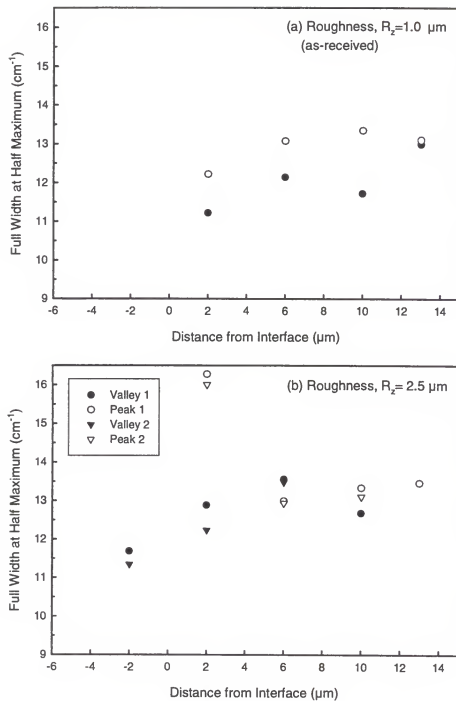


Figure 4.47 Full width at half maximum of diamond Raman peak from the interface to the diamond film surface measured by micro-Raman spectroscopy: (a) interface roughness, $R_z=1.0 \mu\text{m}$, (b) interface roughness, $R_z=2.5 \mu\text{m}$, (c) interface roughness, $R_z=4.5 \mu\text{m}$, and (d) interface roughness, $R_z=6.3 \mu\text{m}$.

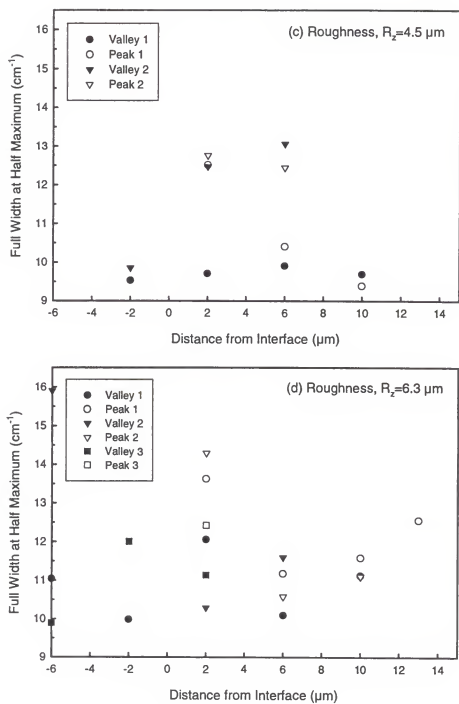


Figure 4.47 --continued

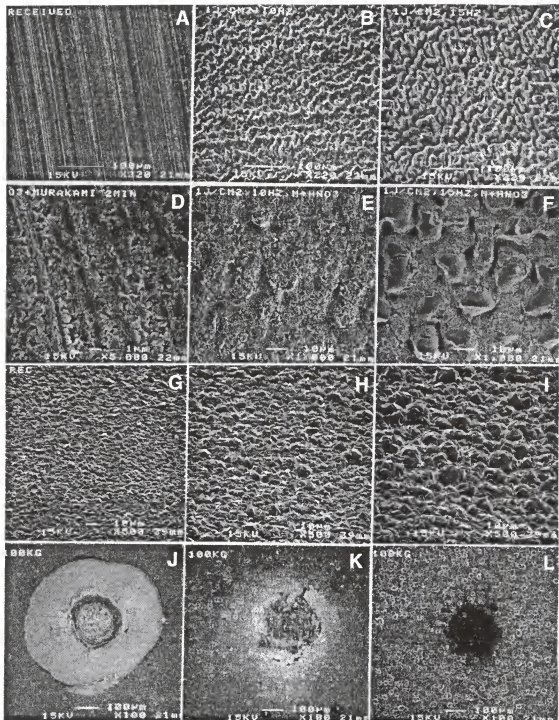


Figure 4.48 Surface morphology of laser modified ((a)-(c)) and etched ((d)-(f)) cemented carbide as well as as-grown ((g)-(i)) and indented ((j)-(l)) diamond films with Rockwell C indenter at 100 kg for for different roughness ($Rz=0.5 \mu\text{m}$ (as-received): (a), (d), (g), and (j), $Rz=2.5 \mu\text{m}$ ($2 \text{ J}/\text{cm}^2$, 80 pulses): (b), (e), (h), and (k), $Rz=3.5 \mu\text{m}$ ($2 \text{ J}/\text{cm}^2$, 120 pulses): (c), (f), (i), and (l)).

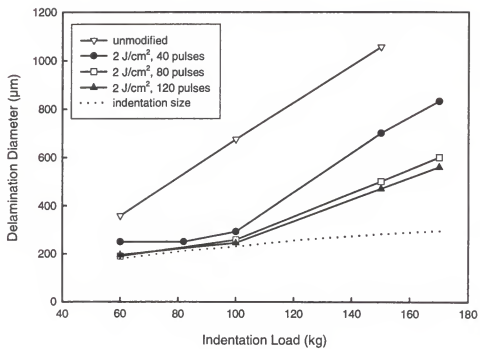


Figure 4.49 Rockwell indentation adhesion test for diamond coated cemented carbides having different roughness.

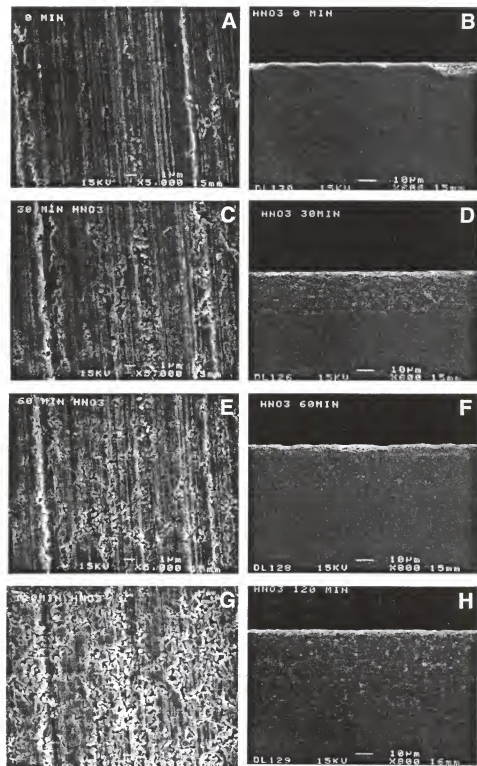


Figure 4.50 Surface morphology changes of cemented carbides etched with nitric acid for (a) 0 min, (c) 30 mins, (e) 60 mins, and (g) 120 mins by stirring. (b), (d), (f), and (h) are the cross-sectional views of (a), (c), (e), and (g), respectively.

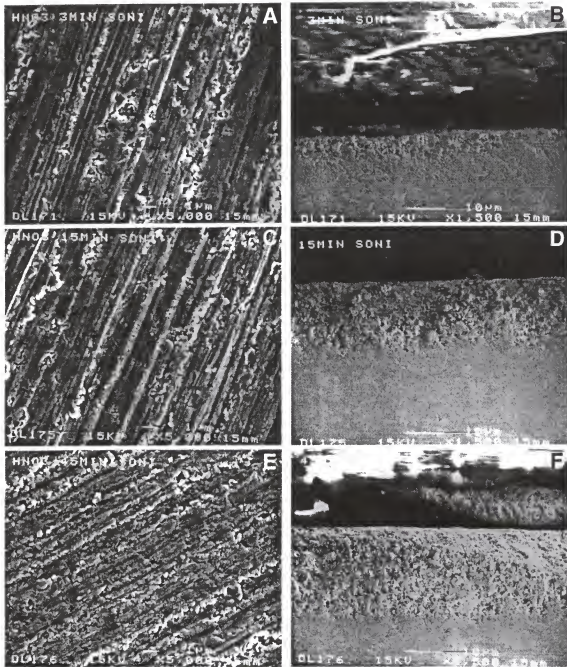


Figure 4.51 Surface morphology changes of cemented carbides etched with nitric acid for (a) 3 mins, (c) 15 mins, and (e) 45 mins by ultra-sonication. (b), (d), and (f) are the cross-sectional views of (a), (c), and (e), respectively.

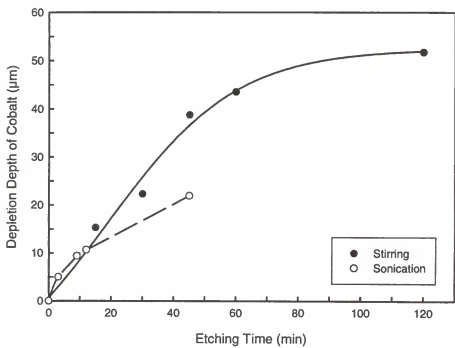


Figure 4.52 Depletion depth of cobalt as a function of etching time by nitric acid.

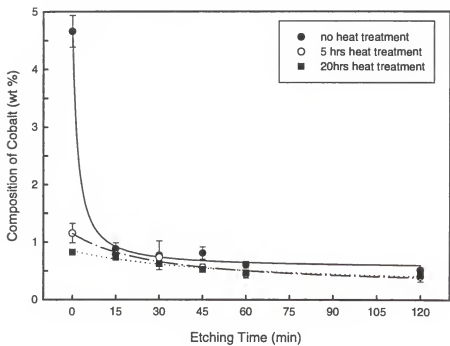


Figure 4.53 Cobalt composition in cemented carbides as a function of etching time and heat treatment.

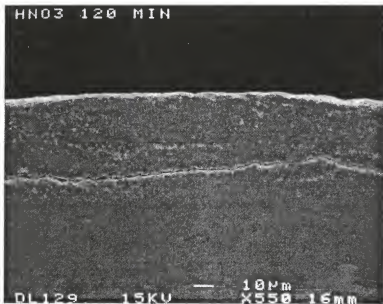


Figure 4.54 Cross-sectional view of cemented carbides etched for 120 minutes.

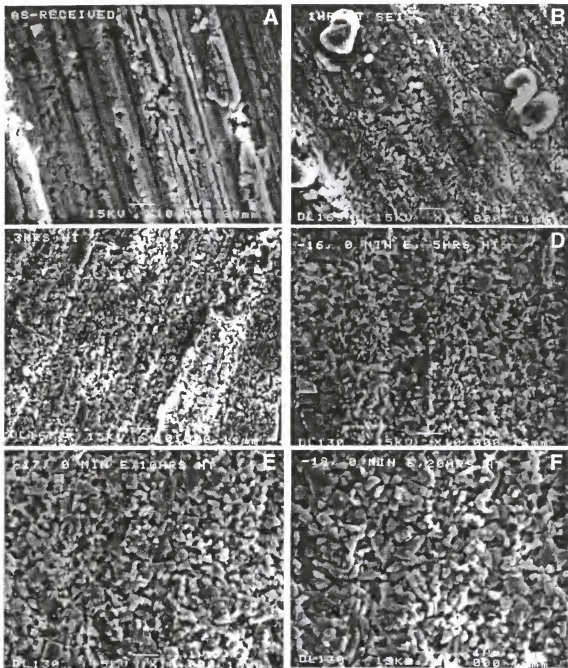


Figure 4.55 Surface morphology changes of cemented carbides with heat treatment time (a) 0 hr, (b) 1 hr, (c) 3 hrs, (d) 5 hrs, (e) 10 hrs, and (f) 20 hrs ($P=20$ Torr, $R_g=200$ sccm, $T_s=920^\circ\text{C}$, $T_f=2000^\circ\text{C}$, F-S distance=1 cm, and pure H_2)

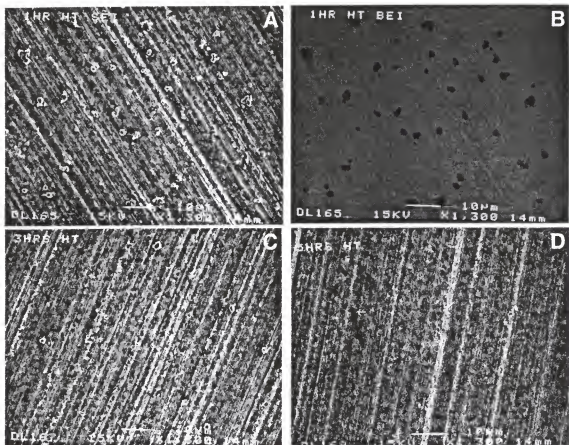


Figure 4.56 Surface morphology changes of cemented carbides as a function of heat treatment time (a) 1 hr, (b) backscattered electron image of (a), (c) 3 hrs, and (d) 5 hrs.

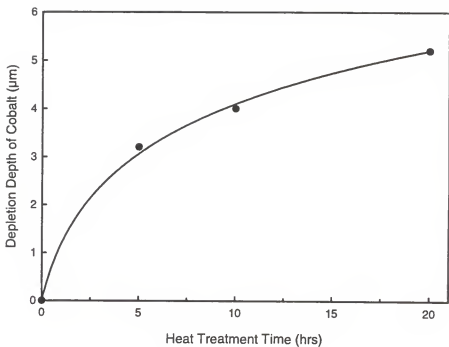


Figure 4.57 Depletion depth of cobalt in cemented carbides as a function of heat treatment time.

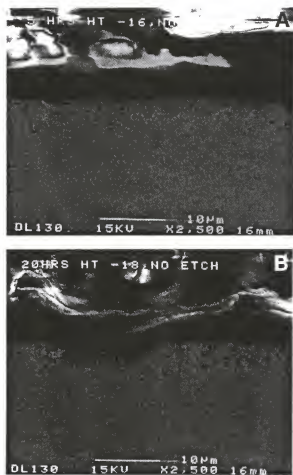


Figure 4.58 Cross-sectional view of cemented carbides with heat treatment time (a) 5 hrs and (b) 20 hrs.

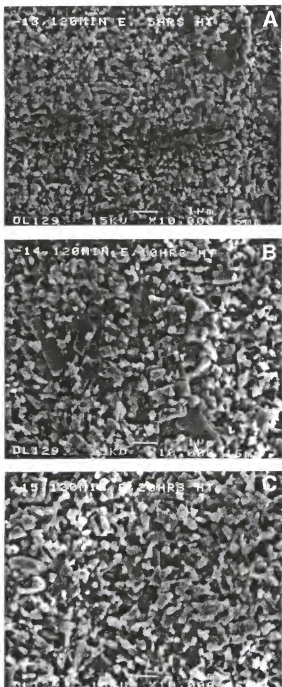


Figure 4.59 Surface morphology changes of cemented carbides etched for 120 mins with heat treatment time (a) 5 hrs, (b) 10 hrs, and (c) 20 hrs.

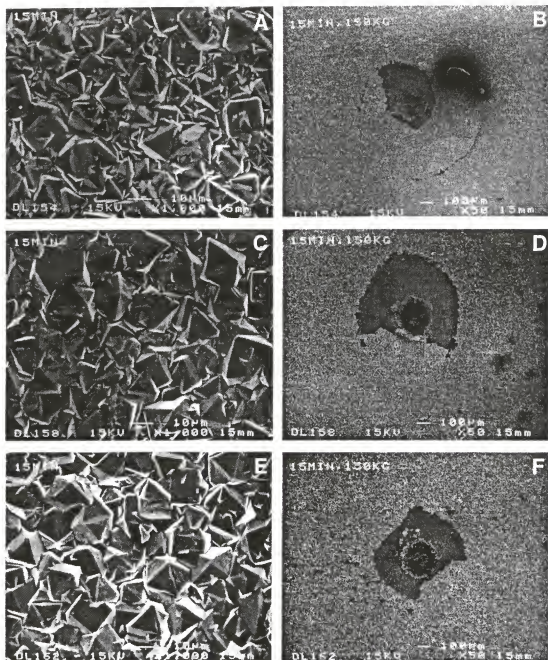


Figure 4.60 Surface morphology of diamond films on cemented carbides which were etched for 15 mins, then heat-treated for (a) 10 hrs, (c) 20 hrs, and (e) 30 hrs as well as indented diamond films ((b), (d), and (f)) of (a), (c), and (e), respectively, using Rockwell C indenter at 150 kg.

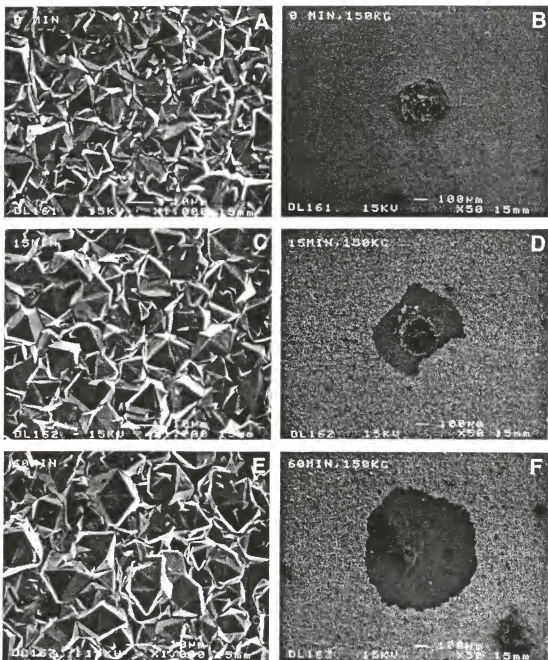


Figure 4.61 Surface morphology of diamond films on cemented carbides which were etched for (a) 0 min., (c) 15 mins, and (e) 60 mins, then heat-treated for 30 hrs as well as indented diamond films ((b), (d), and (f)) of (a), (c), and (e), respectively, using Rockwell C indenter at 150 kg.

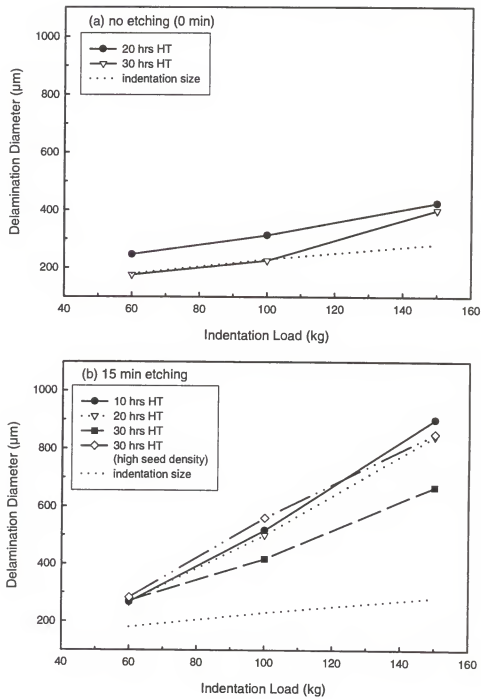


Figure 4.62 Rockwell indentation adhesion test for cemented carbides which were (a) unetched and etched with nitric acid for (b) 15 mins and (c) 60 mins, then heat-treated for various time.

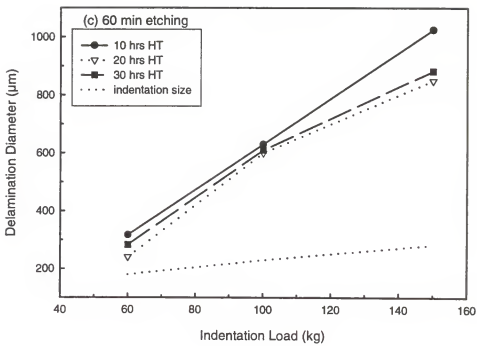


Figure 4.62 --continued

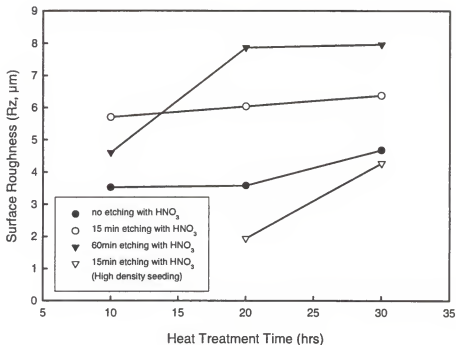


Figure 4.63 Surface roughness changes of diamond films as a function of heat treatment of cemented carbides.

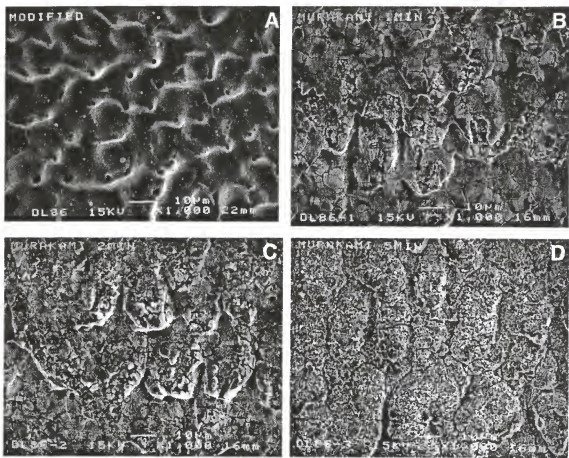


Figure 4.64 Surface morphology changes of laser-modified cemented carbides (2 J/cm^2 , 120 pulses) as a function of etching time (a) 0 min, (b) 1 min (c) 2 mins, and (d) 5 mins using Murakami agent by stirring.

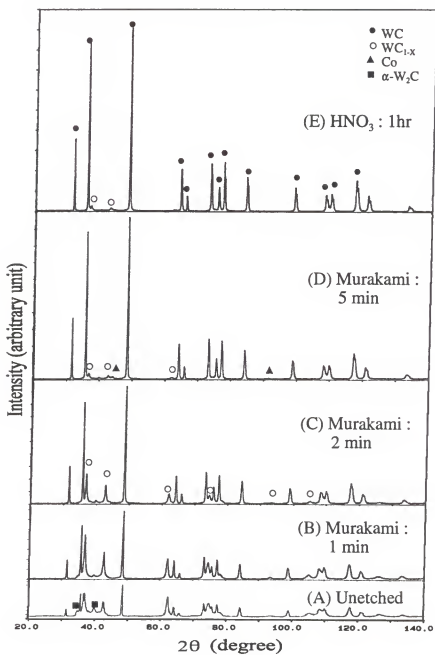


Figure 4.65 X-ray diffraction of laser modified cemented carbide with different etching time using Murakami agent and nitric acid.

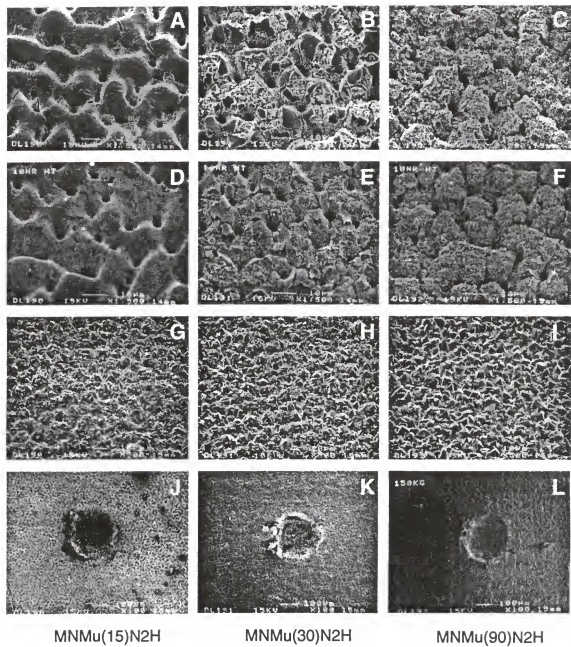


Figure 4.66 Surface morphology of laser-modified cemented carbides which were etched with nitric acid for 60 sec and Murakami agent for (a) 15 sec, (b) 30 sec, and (c) 90 sec, then heat-treated for 10 hrs ((d)-(f)) as well as diamond films ((g)-(i)) and indented diamond films ((j)-(l)) using Rockwell C indenter at 150 kg.

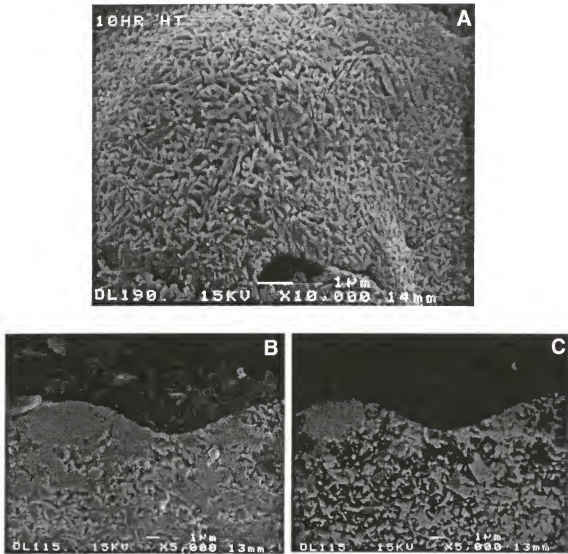


Figure 4.67 Magnified details of heat-treated surface (Fig. 4.66(d)): (a) plane view, (b) cross-sectional view (SEI), and (c) cross-sectional view (BEI).

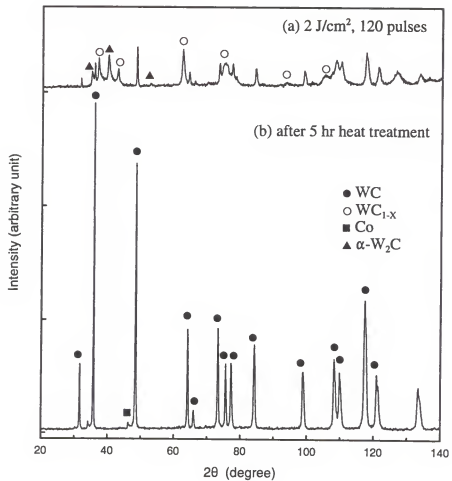


Figure 4.68 X-ray diffractions of laser-modified cemented carbides before and after heat treatment.

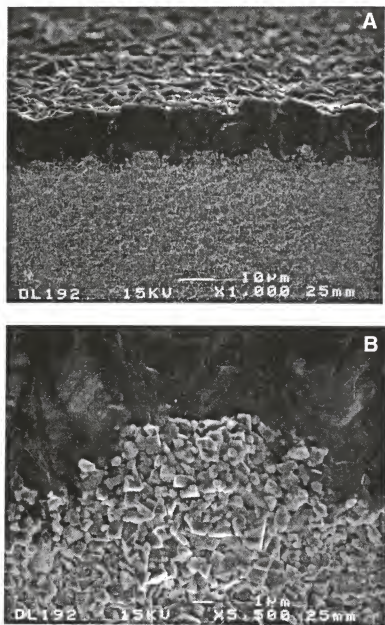


Figure 4.69 Cross-sectional view of diamond coated cemented carbides: (a) low magnification and (b) high magnification.

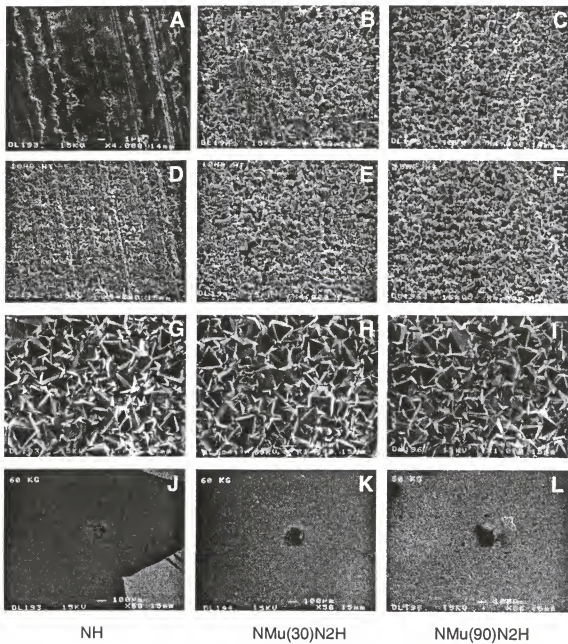


Figure 4.70 Surface morphology of cemented carbides which were etched with nitric acid for 60 sec and Murakami agent for (a) 0 sec, (b) 30 sec, and (c) 90 sec, then heat-treated for 10 hrs ((d)-(f)) as well as diamond films ((g)-(i)) and indented diamond films ((j)-(l)) using Rockwell C indenter at 60 kg.

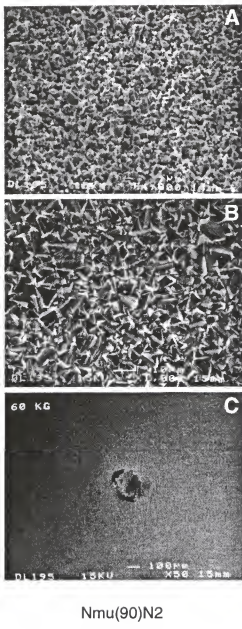


Figure 4.71 Surface morphology of cemented carbides which were etched with nitric acid for 60 sec (a) and Murakami agent for 90 sec without heat treatment as well as diamond films (b) and indented diamond films (c) using Rockwell C indenter at 60 kg.

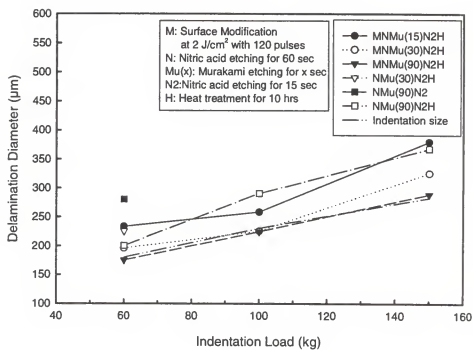


Figure 4.72 Variation of delamination diameter in diamond-coated cemented carbides as a function of indentation load.

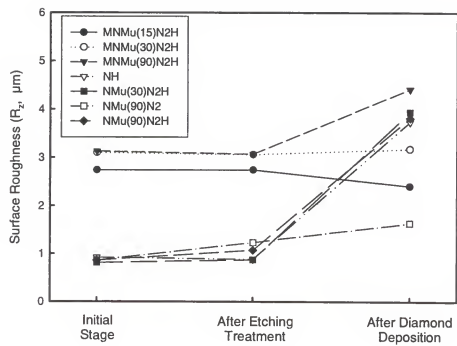


Figure 4.73 Surface roughness changes in cemented carbides after each treatment

CHAPTER 5 CONCLUSIONS

Weak adhesion of diamond films on cemented carbide tool substrates (WC-Co) has been a significant barrier for extensive use in tool applications. This is due to its large thermal expansion mismatch and detrimental effect of the cobalt binder.

A novel method for improving the adhesion of diamond films on cemented carbide tool was developed. This method is based on the formation of a compositionally graded interface by developing a micro-rough surface structure using a pulsed laser process. This laser surface modification induces mechanical interlocking, release of interfacial stress, increase of surface bonding, and complicated crack propagation paths.

In this study, the optimization of process parameters in the hot filament assisted chemical vapor deposition (HFCVD) system for growing good-quality diamond films, the mechanism about the formation of laser induced micro-rough structures (LIMS), and the effects of LIMS on the residual stress of

diamond films and adhesion characteristics has been investigated.

The conditions for growing good-quality diamond films in HFCVD systems were a chamber pressure of 20-30 Torr, gas flow rate of 100-200 sccm, gas composition of less than 1% methane in hydrogen, filament temperature of 1800-2280°C, and substrate temperature of 900-980°C. The effects of each parameter on diamond properties were explained. At high substrate temperature and chamber pressure, and at low filament temperature and methane concentration, {100} crystal faces were favored. {111} crystal faces were favored under reverse conditions.

The deposition of diamond films on LIMS surface of cemented carbides was quite effective for the improvement of adhesion of diamond films. LIMS was formed by interactions of laser radiation with cemented carbides. The laser radiation inhomogeneously but periodically heated up, melted, and evaporated cemented carbide materials on the substrate surfaces. Because of difference in laser energy density between peak and valley regions, the ablated materials were mostly redeposited on peak regions, resulting in periodic rough structures. The laser locally formed melted/redeposited areas (the peaks of LIMS) and melted/evaporated areas (the valleys of LIMS). According to the computer simulation results, cobalt was easily evaporated and tungsten was just

melted. The results obtained with AES measurement suggested that cobalt was segregated to the surface of LIMS due to difference in melting temperature when the cemented carbide liquid solidified. Other forms of tungsten carbide having low contents of carbon such as WC_{1-x} ($x=0-0.3$) and W_2C formed in the melt-zone of LIMS with a grain size of 50-100 nm due to the evaporation of carbon from tungsten carbide melt during laser irradiation. Shallow films of (tungsten-cobalt) oxide also formed on the surface of peak regions in LIMS.

From the observation of stress distribution inside diamond films using micro-Raman spectroscopy, the interfacial stress of diamond-cemented carbide decreased with increasing roughness of LIMS. The adhesion of diamond films was improved with increasing roughness of cemented carbide from the indentation adhesion test.

Etching treatment with nitric acid was helpful but not much effective for adhesion of diamond films because overetching weakened the cemented carbide substrate by loosening the bonding of tungsten carbide particles. Use of Murakami's agent for cleaning and microroughening tungsten carbides was good for adhesion of diamond films. Heat treatment of cemented carbides in activated hydrogen atmosphere in HFCVD system before diamond coating also improved the adhesion of diamond films.

APPENDIX
PROPERTIES AND APPLICATIONS OF CVD DIAMOND

Table A1 and A2 show the properties and applications of chemically vapor deposited (CVD) diamond films. Diamond has outstanding mechanical, thermal, chemical, electronic and optical properties. Owing to excellent combination of extreme properties, there are a lot of applications.

Table A1. Comparison of physical properties of CVD diamond with other materials.

Property	CVD diamond	Alternative
Thermal Conductivity (W/cm ⁻² °C)	10-18	Copper 4.0
Hardness (kg/mm ²)	9000	CBN 4500
Optical Transmissivity	225 nm to far IR	Sapphire
Band Gap (eV)	5.4	GaAs 1.43
Coefficient of Friction	0.05-0.7	Teflon 0.05
Thermal Expansion (ppm)	2.0	Si 2.6
Electrical Resistivity (ohm-cm)	10^{15} ($< 10^{-3}$ doped)	Al_2O_3 10^{15}

Table A2. Properties and applications of diamond coatings.

Properties	Applications
<ul style="list-style-type: none"> • Hardest known material High compressive strength Low friction coefficient • High elastic modulus Low thermal expansion • Broad optical transparency from UV to IR • Chemical inertness • Biocompatibility • High thermal conductivity Good electrical insulator • High hole mobility Wide band gap High breakdown voltage • Negative electron affinity 	<ul style="list-style-type: none"> • Coating for cutting tools Abrasive coatings • Loudspeaker diaphragms • Windows, lens coatings, x-ray lithography masks • Protective coatings for chemical and nuclear reactors • Diamond coated joint materials, teeth, biosensors • Heat diffuser for high temperature/high power semiconductor devices • Semiconductor for high power, radiation, and frequency electronic devices • Cold cathode for field emission display

LIST OF REFERENCES

Age93 J. W. Ager III and M. Drory, *Phys. Rev. B*, **48**, 2601 (1993).

Aka89 K. Akashi, T. Yoshida, S. Komatsu, and Y. Mitsuda, *J. Korean Inst. Metals*, **24**, 712 (1989).

Ang68 J. C. Angus, H. A. Will, and W. S. Stanko, *J. Appl. Phys.*, **39**, 2915 (1968).

Ang91 J. C. Angus, Y. Wang, and M. Sunkara, *Annu. Rev. Mater. Sci.*, **21**, 221 (1991).

Ase88 T. Aselage and K. Keefer, *J. Mater. Res.*, **3**(6), 1279 (1988).

Bac89 P. K. Bachmann and R. Messier, *Chem. Eng. News*, May 24 (1989).

Bac92 P. K. Bachmann and D. V. Wiechert, *Diamond Relat. Mater.*, **1**, 422 (1992).

Bad88 A. R. Badzian, in *Advances in X-ray Analysis*, edited by C. S. Barrett, J. V. Grefrich, R. Kenkins, J. C. Russ, J. W. Richardson, and P. K. Predeck (Plenum, New York), **31**, 113 (1988).

Bag92 J. A. Baglio, B. C. Farnsworth, S. Hankin, G. Hamill, and D. O'Neil, *Thin Solid Films*, **212**, 180 (1992).

Bah95 D. F. Bahr, J. C. Nelson, D. Zhuang, E. Pfender, J. Heberlein, and W. W. Gerberich, *Mat. Res. Soc. Symp. Proc.*, Vol **383**, 209 (1995).

Bee84 D. Beeman, J. Silverman, R. Lynds, and M. R. Anderson, *Phys. Rev. B*, **30**, 870 (1984).

Ber94 L. Bergman, M. T. McClure, J. T. Glass, and R. J. Nemanich, *J. Appl. Phys.*, **76**, 3020 (1994).

Ber97 L. Bergman and R. J. Nemanich, in *Handbook of Optical Properties, Vol. II*, edited by R. E. Hummel and P. Wißmann (CRC Press, Boca Raton, FL), Chapter 12 (1997).

Bou91 P. Bou and L. Vandenbulcke, *J. Electrochem. Soc.*, **138**, 2991 (1991).

Bro92 K. J. A. Brookes, *World Directory and Handbook of Hardmetals and Hard Materials* (International Carbide Data, Hertfordshire) D112-D116 (1992).

Bru93 R. Brunsteiner, R. Haubner, and B. Lux, *Diamond Relat. Mater.*, **2**, 1263 (1993).

Bun61 F. P. Bundy, H. P. Bovenkerk, H. M. Strong, and R. H. Wentorf, Jr., *J. chem. Phys.*, **35**, 383 (1961).

Cel89 F. G. Celii and J. E. Butler, *Appl. Phys. Lett.*, **54**, 1031 (1989).

Cel91 F. G. Celii and J. E. Butler, in *New Diamond Science and Technology*, edited by R. Messier, J. E. Butler, and J. T. Glass (Materials Research Society, Pittsburgh), 201-206 (1991).

Cer93 F. M. Cerio, J. A. Herb, and R. Cummings, *Surf. Coat. Technol.*, **62**, 674 (1993).

Cha74 B. N. Chapman, *J. Vac. Sci. Technol.*, **11**(1), 106 (1974).

Che93 C. -F. Chen and T. -M. Hong, *Surf. Coat. Technol.*, **58**, 143 (1993).

Che93 X. Chen and J. Narayan, *J. Appl. Phys.*, **74**, 4168 (1993).

Chi81 S. S. Chiang, D. B. Marshall, and A. G. Evans, in *Surface and Interfaces in Ceramics and Ceramic-Metal Systems*, edited by J. Pask and A. G. Evans (Plenum, New York), 603 (1981).

Cul78 B. D. Cullity, *Element of X-Ray Diffraction* (Addison-Wesley, Reading, MA) Chapter 16 (1978).

Dav89 J. L. Davidson, C. Ellis, and R. Ramesham, *J. Electron. Mater.*, **18**, 711 (1989).

Der68 B. V. Deryagin, D. V. Fedoseev, V. M. Lukyanovich, B. V. Spitsyn, V. A. Ryabov, and A. V. Lavrentyev, *J. Crystal Growth*, **2**, 380 (1968).

Der89 B. V. Deryagin and D. V. Fedoseev (translation of Nauka, Moscow, 1977), *Surf. Coat. Technol.*, **38**, 133 (1989).

Deu96 F. Deurler, H. van den Berg, R. Tabersky, A. Freundlieb, M. Pies, and V. Buck, *Diamond Relat. Mater.*, **5**, 1478 (1996).

Emm73 D. C. Emmony, R. P. Howson, and L. J. Willis, *Appl. Phys. Lett.*, **23**(11), 598 (1973).

End96 I. Endler, A. Leonhardt, H. -J. Scheibe, and R. Born, *Diamond Relat. Mater.*, **5**, 299 (1996).

Eto92 H. Eto, Y. Tamou, Y. Ohsawa, and N. Kikuchi, in *Diamond and Diamondlike and Related Coatings 1991*, edited by P. K. Bachmann and A. Matthews (Elsevier, Amsterdam), 373-379 (1992).

Eve62 W. G. Eversole, US Patent 3,030,187 and 3,030,188 (1962).

Fol94 S. R. Foltyn, in *Pulsed Laser Deposition of Thin Films*, edited by D. B. Chrisey and G. K. Hubler (John Wiley & Sons, NY) Chapter 4 (1994).

Fre91 M. Frenklach and H. Wang, *Phys. Rev. B*, **43**, 1520 (1991).

Gei92 M. W. Geis and J. C. Angus, *Sci. Amer.*, October, 84 (1992).

Gol92 J. I. Goldstein, D. E. Newbury, R. Echlin, D. C. Joy, A. D. Romig, Jr., C. E. Lyman, C. Fiori, and E. Lifshin, Eds., *Scanning Electron Microscopy and X-Ray Microanalysis: A Text for Biologists, Materials Scientists, and Geologists*, 2nd edition (Plenum, New York) Chapter 3 (1992).

Gra93 K. J. Grannen, F. Xiong, and R. P. H. Chang, *Surf. Coat. Technol.*, **57**, 155 (1993).

Gre94 S. M. Green, A. Pique, K. S. Harshavardhan, and J. S. Bernstein, in *Pulsed Laser Deposition of Thin Films*, edited by D. B. Chrisey and G. K. Hubler (John Wiley & Sons, New York) Chapter 2 (1994).

Hay93 R. Hay, *Cutting Tool Eng.*, **45**, 52 (1993).

Hec92 J. Hecht, *Laser Focus World*, June, 63 (1992).

Hic60 T. W. Hickmott, *J. Chem. Phys.*, **32**, 810 (1960).

Hir89 Y. Hirose, S. Ananuma, N. Okada, and K. Komaki, in *Diamond and Diamondlike Films, Proceedings*, edited by J. Dismukes et al. (Electrochemical Society, Pennington, NJ) **89-12**, 80-85 (1989).

Ike96 T. Ikeda and S. Kameoka, *Kobelco Technol. Rev.*, no. 19, 17 (1996).

Iso93 T. Isozaki, Y. Saito, A. Masuda, K. Fukumoto, M. Chosa, T. Ito, E. J. Oles, A. Inspector, and C. E. Bauer, *Diamond Relat. Mater.*, **2**, 1156 (1993).

Ito91 T. Ito, in *Application of Diamond Films and Related Materials*, edited by Y. Tzeng, M. Yoshikawa, M. Murakawa, and A. Feldman (Elsevier, Amsterdam) 77 (1991).

Jin87 P. C. Jindal, D. T. Quinto, and G. J. Wolfe, *Thin Solid Films*, **154**, 361 (1987).

Jof88 P. O. Joffreau, R. Haubner, and B. Lux, *Int. J. Refract. & Hard Met.* **7**(4), 186 (1988).

Kam83 M. Kamo, Y. Sato, S. Matsumoto, and N. Setaka, *J. Cryst. Growth*, **62**, 642 (1983).

Kar96 J. Karner, M. Pedrazzini, I. Reineck, M. E. Sjöstrand, and E. Bergmann, *Mater. Sci. Eng.*, **A209**, 405 (1996).

Kaw87 T. Kawato and K. Kondo, *Jpn. J. Appl. Phys.*, **26**, 1429 (1987).

Kenna Kennametal Catalog 6000, Lathe Tooling.

Kik87 N. Kikuchi and H. Yoshimura, *New Diamond* (Japan New Diamond Forum), **7**, 26 (1987).

Kik91 N. Kikuchi, H. Eto, T. Okamura, and H. Yoshimura, in *Application of Diamond Films and Related Materials*, edited by Y. Tzeng, M. Yoshikawa, M. Murakawa, A. Feldman (Elsevier, Amsterdam), 61 (1991).

Kob88 K. Kobashi, K. Nishimuri, Y. Kawate, T. Horiuchi, *Phys. Rev. B*, **38**, 4067 (1988).

Kuo90 C. T. Kuo, T. Y. Yen, and T. H. Huang, *J. Mater. Res.*, **5**(11), 2515 (1990).

Kur88 K. Kurihara, K. Sesaki, M. Kawarada, N. Koshino, *Appl. Phys. Lett.*, **52**, 437 (1988).

Kur92 K. Kurihara, K. Sasaki, M. Kawarada, and Y. Goto, *Thin Solid Films*, **212**, 164 (1992).

Lan12 I. Langmuir, *J. Am. Chem. Soc.*, **34**, 860 (1912).

Lee96 D. G. Lee and R. K. Singh, in *Proceedings of the 5th World Congress on Particle Technology 1996* (San Diego, CA) (1996).

Lee98 D. G. Lee, J. M. Fitz-Gerald, and R. K. Singh, *Surf. Coat. Technol.*, **100-101** (1-3), 187 (1998).

Lux92 B. Lux, R. Haubner, and P. Renard, *Diamond Relat. Mater.*, **1**, 1035 (1992).

Mar85 E. E. Marinero, W. Palmer, V. Jipson, and W. Y. Lee, *J. Vac. Sci. Technol.*, **B3**(5), 1560 (1985).

Mat82 S. Matsumoto, Y. Sato, M. Tsatsumi, and N. Setaka, *J. Mater. Sci.*, **17**, 3106 (1982).

Mat85 S. Matsumoto, *J. Mater. Sci. Lett.*, **4**, 600 (1985).

Mat89 Y. Matsui, A. Yuuki, M. Sahara, Y. Hirose, *Jpn. J. Appl. Phys.*, **28**, 1718 (1989).

May95 P. W. May, *Endeavour*, **19**(3), 101 (1995).

McC89 R. C. McCune, R. E. Chase, and W. R. Drawl, *Surf. Coat. Technol.*, **39/40**, 223 (1989).

McC92 R. C. McCune, R. E. Chase, and E. L. Cartwright, *Surf. Coat. Technol.*, **53**, 189 (1992).

Mou89 T. D. Moustakas, *Solid State Ionics* **32/33**, 861 (1989).

Mur88 M. Murakawa, S. Takeuchi, H. Miyazawa, and Y. Hirose, *Surf. Coat. Technol.*, **36**, 303 (1988).

Nes93 M. Nesládek, J. Spinnewyn, C. Asinari, R. Lebout, and R. Lorent, *Diamond Relat. Mater.*, **3**, 98 (1993).

Nes95 M. Nesládek, K. Vandierendonck, C. Quaeyhaegens, M. Kerkhofs, and L. M. Stals, *Thin Solid Films*, **270**, 184 (1995).

Oak91 J. Oakes, X. X. Pan, R. Haubner, and B. Lux, *Surf. Coat. Technol.*, **47**, 600 (1991).

Ohr92 M. Ohring, *The Materials Science of Thin Films* (Academic Press, San Diego), Chapter 9 (1992).

Ole96 E. J. Oles, A. Inspektor, and C. E. Bauer, *Diamond Relat. Mater.*, **5**, 617 (1996).

Par93 B. S. Park, Y. -J. Baik, K. -R. Lee, K. Y. Eun, and D. H. Kim, *Diamond Relat. Mater.*, **2**, 910 (1993).

Pat86 B. B. Pate, *Surf. Sci.*, **165**, 83 (1986).

Ral95 V. G. Ralchenko, A. A. Smolin, V. G. Pereverzev, E. D. Obraztsova, K. G. Korotoushenko, V. I. Konov, Y.V. Lakhotkin, and E. N. Loubnin, *Diamond Relat. Mater.*, **4**, 754 (1995).

Rat95 D. Rats, L. Bimbault, L. Vandenbulcke, R. Herbin, and K. F. Badawi, *Mat. Res. Soc. Symp. Proc.*, Vol. **383**, 159 (1995).

Rei90 I. Reineck, S. Söderberg, K. Westergren, and H. Shahani, in *2nd Int. Conf. on the New Diamond Science and Technology* (Washington, DC), (1990).

Rei93 I. Reineck, S. Söderberg, P.-E. Ekholm, and K. Westergren, *Surf. Coat. Technol.*, **57**, 47 (1993).

Rud92 R. A. Rudder, J. B. Posthill, G. C. Hudson, D. P. Malta, R. E. Thomas, R. J. Markunas, T. P. Humphreys, R. J. Nemanich, in *Wide Band Gap Semiconductors*, edited by T. D. Moustakas, J. I. Pankove, and T. Hamakawa, *Mat. Res. Soc. Proc.* (Materials Research Society, Pittsburgh, PA) **242**, 23-30 (1992).

Sai86 Y. Saito, S. Matsuda, and S. Nogita, *J. Mater. Sci. Lett.*, **5**, 565, (1986).

Sai88 Y. Saito, K. Sato, H. Tanaka, K. Fujita, and S. Matsuda, *J. Mater. Sci.* **23**, 842 (1988).

Sai90 K. Saijo, M. Yagi, K. Shibuki, and S. Takatsu, *Surf. Coat. Technol.*, **43/44**, 30 (1990).

Sai91 Y. Saito, K. Sato, and S. Matuda, *J. Mater. Sci.*, **26**, 2937 (1991).

Sen92 P. K. Sen, *Indust. Diamond Rev.*, **5**, 228 (1992).

Set87 N. Setaka, in *Chemical Vapor Deposition 1987, Proc. Tenth International Conf. On Chemical Vapor Deposition*, edited by G. W. Cullen and J. Blocher, Jr. (The Electrochemical Society, Pennington, NJ), 1156-1163 (1987).

Set89 N. Setaka, *J. Mater. Res.*, **4**, 664 (1989).

Shi88 K. Shibuki, M. Yagi, K. Saijo, and S. Takatsu, *Surf. Coat. Tech.*, **36**, 295 (1988).

Shi94 K. Shibuki, K. Sasaki, M. Yagi, T. Suzuki, and Y. Ikuhara, *Surf. Coat. Technol.*, **68/69**, 369 (1994).

Sin88 B. Singh, Y. Arie, A. W. Lavine, and R. O. Mesker, *Appl. Phys. Lett.*, **52**, 451 (1988).

Sin92 R. K. Singh and J. Viatella, *JOM*, **44**(3), 20 (1992).

Sin96 R. K. Singh, D. R. Gilbert, J. Fitz-Gerald, S. Harkness, and D. G. Lee, *Science*, **272**, 396 (1996).

Sin97 R. K. Singh and J. M. Fitz-Gerald, *Nucl. Instr. and Meth. in Phys. Res. B* **121**, 363 (1997).

Sna91 K. A. Snail, C. M. Marks, Z. P. Lu, J. Herberlein, and E. Pfender, *Mater. Lett.*, **12**, 301 (1991).

Sod90 S. Söderberg, A. Gerendas, and M. Sjöstrand, *Vacuum*, **41**, 1317 (1990).

Sod91 S. Söderberg, K. Westergren, I. Reineck, P. E. Ekholm, and H. Shahani, in *Application of Diamond Films and Related Materials*, edited by Y. Tzeng, M. Yoshikawa, M. Murakawa, and A. Feldman (Elsevier, Amsterdam), 43 (1991).

Som90 M. Sommer and F. W. Smith, *J. Mater. Res.*, **5**, 2433 (1990).

Spa89a K. E. Spear and M. Frenklach, in *Diamond and Diamond-like Films*, edited by J. P. Dismukes, A. J. Purdes, J. C. Angus, R. F. Davis, B. M. Meyerson, K. E. Spear, and M. Yoder (The Electrochemical Society, Pennington, NJ), 122-138 (1989).

Spe89b K. E. Spear, *J. Am. Ceram. Soc.*, **72**, 171 (1989).

Spi81 B. V. Spitsyn, L. L. Bouilov, and B. V. Deryagin, *J. Crystal Growth*, **52**, 219 (1981).

Suz87 K. Suzuki, A. Sawabe, H. Yasuda, and T. Inuzuka, *Appl. Phys. Lett.*, **50**, 728 (1987).

Tah95 M. A. Taher, J. L. Shultz, S. Nasrazadani, H. A. Naseem, W. D. Brown, and A. P. Malshe, *Electrochem. Soc. Proc.*, **95-4**, 614 (1995).

Wad80 N. Wada, P. J. Grazi, and S. A. Solin, *J. Non-Cryst. Solids*, **35**, 543 (1980).

Wag82 D. D. Wagman, *J. Phys. Chem. Ref. Data*, **11**, 83 (1982).

Wil93a R. L. Williamson, B. H. Rabin, and J. T. Drake, *J. Appl. Phys.*, **74**(2), 1310 (1993).

Wil93b C. Wild, P. Koidl, W. Müller-Sebert, H. Walcher, R. Kohl, N. Herres, R. Locher, R. Samlenski, and R. Brenn, *Diamond Relat. Mater.*, **2**, 158 (1993).

Win91 H. Windischmann, G. F. Epps, Y. Cong, R. W. Collins, *J. Appl. Phys.*, **69**, 2231 (1991).

Yar89 W. A. Yarborough, M. A. Stewart, and J. A. Cooper, *Surf. Coat. Technol.*, **39**, 241 (1989).

Yod93 M. N. Yoder, in *Diamond Films and Coatings*, edited by R. F. Davis (Noyes, Park Ridge, NJ) Chapter 1 (1993).

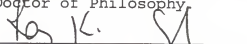
You82 J. F. Young, J. E. Sipe, J. S. Preston, and H. M. van Driel, *Appl. Phys. Lett.*, **41**(3), 261 (1982).

Zhu89 W. Zhu, C. A. Randall, A. R. Badzian, and R. Messier, *J. Vac. Sci. Technol.*, **A7**, 2315 (1989).

BIOGRAPHICAL SKETCH

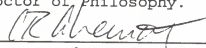
Dong-Gu Lee was born on November 11, 1962, in Seoul, Korea. He grew up in Seoul and received his Bachelor of Engineering in Metallurgical Engineering from the Korea University in Seoul in February of 1985. He entered into the graduate school program at Korea University in March of 1985 and completed his Master of Engineering in February of 1987. He joined the Republic of Korea Army in August of 1987 and was discharged in February of 1988. He then worked on magnetic materials in the Division of Metal, Korea Institute of Science and Technology (KIST) in Seoul until July, 1992. He moved to the University of Florida, Gainesville, Florida, in the fall of 1992 to begin his studies for the degree of Doctor of Philosophy in the field of materials science and engineering with a specialty in electronic materials.

I certify that I have read this study and that in my opinion it conforms to acceptable standards of scholarly presentation and is fully adequate, in scope and quality, as a dissertation for the degree of Doctor of Philosophy.



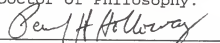
Rajiv K. Singh, Chair
Professor of Materials
Science and Engineering

I certify that I have read this study and that in my opinion it conforms to acceptable standards of scholarly presentation and is fully adequate, in scope and quality, as a dissertation for the degree of Doctor of philosophy.



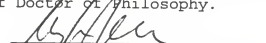
Cammy R. Abernathy
Professor of Materials
Science and Engineering

I certify that I have read this study and that in my opinion it conforms to acceptable standards of scholarly presentation and is fully adequate, in scope and quality, as a dissertation for the degree of Doctor of Philosophy.



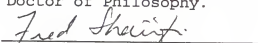
Paul H. Holloway
Professor of Materials
Science and Engineering

I certify that I have read this study and that in my opinion it conforms to acceptable standards of scholarly presentation and is fully adequate, in scope, and quality, as a dissertation for the degree of Doctor of Philosophy.



Stephen J. Pearton
Professor of Materials
Science and Engineering

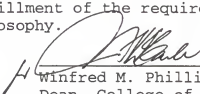
I certify that I have read this study and that in my opinion it conforms to acceptable standards of scholarly presentation and is fully adequate, in scope and quality, as a dissertation for the degree of Doctor of Philosophy.



Fred Sharifi
Assistant Professor of
Physics

This dissertation was submitted to the Graduate Faculty
of the College of Engineering and to the Graduate School and
was accepted as partial fulfillment of the requirements for
the degree of Doctor of Philosophy.

August, 1998


Winfred M. Phillips
Dean, College of
Engineering

Karen A. Holbrook
Dean, Graduate School